



T.C. DOĐUŐ UNIVERSITY
INSTITUTE OF SCIENCE AND TECHNOLOGY
ELECTRONICS AND COMMUNICATIONS ENGINEERING

**CHARACTERIZATION OF EM WAVE PROPAGATION IN
METAMATERIAL ENVIRONMENTS**

PhD DISSERTATION

AYŐEGÜL PEKMEZCİ

2012198001

SUPERVISOR:

PROF. DR. ERCAN TOPUZ

İstanbul, December 2018



DOĞUŞ ÜNİVERSİTESİ
FEN BİLİMLERİ ENSTİTÜSÜ

Tarih : 25/12/2018

Doktora Tez Savunma Sınav Tutanağı

Anabilim Dalı : Electronics and Communication Engineering
Öğrencinin Adı Soyadı : Ayşegül Pekmezci
Öğrenci No : 2012198001
Tez Danışmanının Adı Soyadı : Prof.Dr.Ercan Topuz
Tezin Başlığı : Characterization of EM Wave Propagation in Metamaterial
Environments

Doğuş Üniversitesi Lisansüstü Eğitim-Öğretim ve Sınav Yönetmeliği'nin 44.Maddesi uyarınca yapılan değerlendirmeler sonunda;

tezin kabul edilmesine

tezde düzeltme verilmesine

tezin reddedilmesine

oy birliği / oy çokluğu ile karar verilmiştir. Gereği için arz olunur.

Danışman Üye

Prof.Dr.Ercan Topuz

Üye

Prof.Dr.Funda Akleman Yapar

Üye

Doç.Dr.Çağatay Uluşık

Üye

Prof. Dr. H. Selçuk Varol

Üye

Doç.Dr.Fikret Tokan

Anabilim Dalı Başkanı Onayı:

Prof. Dr. H. Selçuk Varol

DECLARATION

I declare that this thesis is my own work and has not been submitted in any form for another degree or diploma at any university or institution. Information derived from the published or unpublished work of others has been acknowledged in the text and a list of references is given.

Ayşegül Pekmezci

Signature: 

Date: 25/12/2018

ACKNOWLEDGEMENTS

I would like to express my sincerest gratitude to my supervisor, Prof. Dr. Ercan Topuz for his infinite support and patience, suggestions and guidance throughout this dissertation. The successful completion of this thesis would not have been possible without his outstanding technical guidance, constructive comments and encouragements. I am also grateful to him, for whom I worked with great pleasure during my research, and had opportunity to learn a lot from his wisdom about academy and experience of life. Hence, I owe thanks to him since I have the honor of being his PhD student.

I would also like to extend my thanks to Prof. Dr. Levent Sevgi, who provided me to continue my PhD studies at Dođuş University. I would like to express my appreciation to him for his great help and advice on computational issues during my studies. Even if he left Dođuş University, he has never lost contact and has given me the opportunity to benefit from his views and ideas.

Additionally, I would specially like to thank Ünsal Kocatepe, who has been in my life for a long time, for his unlimited patience, calmness and love throughout these years. Thank you so much for your support and encouragement which enabled me to complete this study.

Finally, I would like to thank my family who has always supported and loved me. I am so grateful to them for their encouragement and belief in achieving this work.

ABSTRACT

In this thesis, analytical and numerical solutions of the electromagnetic wave propagation in certain environments loaded with metamaterial (MTM) are presented.

Finite Difference Time Domain (FDTD) algorithm is one of the most popular numerical techniques applicable to this problem area provided that it is augmented with Auxiliary Differential Equation (ADE) or Partial Linear Recursive Convolution (PLRC) methods to account for the dispersive characteristics of the MTM. To investigate the electromagnetic wave propagation in dispersive media Maxwell's curl and wave equation based FDTD algorithms are developed.

FDTD update equations are obtained using ADE and also PLRC FDTD formulations for MTM medium described by Lorentz models. Numerical results obtained using the proposed FDTD algorithm are compared with the analytical results. FDTD algorithm based on the wave equation for double-negative (DNG) medium is also obtained using ADE approach, and its performance in terms of computational time and memory requirements is compared with the curl equation based formulations.

Another issue discussed in this thesis is the novel formulation of Mur's ABC developed for truncating the DNG media for 1D and 2D problems using PLRC-FDTD algorithm. Efficient and simple FDTD update equations for first and second order Mur's absorbing boundary conditions (ABC) are obtained from frequency domain one-way wave equation using PLRC method and coefficient parameters are given for both Lorentz and Drude models. To demonstrate the validity and stability of the proposed Mur formulations, its absorption performance and computational advantages are compared with modified Uniaxial Perfectly Matched Layer (UPML).

Finally, electromagnetic wave propagation is investigated in a rectangular waveguide partially loaded with DNG materials along a transverse or along the axial directions. Properties of eigen-solutions in waveguide environments partially loaded with Lorentz type DNG materials, modelled by lossless/lossy, identical/non-identical electric and magnetic parameters are investigated. The phase and group velocities are calculated and drawn for several problem scenarios. Modal cutoff phenomena associated with surface waves, transitions between evanescent/propagating, forward/backward waves and

their dependence on frequency, filling factor and material parameters are also investigated. Novel conditions are given for existence of surface waves and for emergence of complex eigenvalues in the absence of losses. Analytic solutions of reflection and transmission coefficients are obtained for single mode supporting waveguide sections fully/partially loaded with DNG slabs in one transverse direction using Mode Matching Method. Floquet mode formalism is extended and applied to description of propagating fields in a waveguide loaded along the axial direction with air-DNG slabs in a quasi-periodic fashion. Eigenvalue and band-edge equations are obtained and representative solutions for dispersion and band edge diagrams are presented. Scattering characteristics and their dependence on the number of unit cells and the termination strategy used in the truncated structure are also investigated. Frequency dependence of reflection and transmission factors are calculated using frequency domain approach and compared with the results obtained from FDTD method.

Key words: Metamaterials, Lorentz model, Mur type absorbing boundary condition, Finite Difference Time Domain, eigen-solutions of dispersive rectangular waveguide, group and phase velocity, surface waves, complex waves, Floquet waves.

ÖZET

Bu tezde, metamalzeme ile yüklenmiş ortamlardaki elektromanyetik dalga yayılımının analitik ve nümerik çözümleri verilmiştir.

Maxwell denklemlerini çözmenin bilinen en popüler sayısal tekniklerinden biri olan Zaman Bölgesinde Sonlu Farklar (Finite Difference Time Domain, FDTD) metodu, Yardımcı Diferansiyel Denklem (Auxiliary Differential Equation, ADE) ve Parçalı Doğrusal İteratif Konvolüsyon (Piecewise Linear Recursive Convolution, PLRC) yöntemleri kullanılarak Maxwell dönele ve dalga denklemleri dispersif ortamlarda elektromanyetik dalga yayılımını incelemek için kullanılmıştır.

Lorentz modeliyle tanımlanan Epsilon Negatif (ENG) ortamda elektromanyetik dalga yayılımı, dalga denklemi tabanlı dispersif FDTD algoritmalarından ADE ve PLRC yöntemleri kullanılarak incelenmiş, sayısal sonuçlar analitik sonuçlarla karşılaştırılmış ve dalganın ENG malzeme ile yüklü ortamdaki saçılma karakteristiği gösterilmiştir. Çift negatif malzeme (Double Negative Material, DNG) ile yüklü ortam için ise ADE yaklaşımı kullanılarak dalga denklemi tabanlı FDTD algoritması elde edilmiş ve dalga denklemi kullanılarak elde edilen FDTD algoritmasının bilgisayar bellek/hesaplama zamanı gereksinimleri açısından Maxwell dönele denklemleriyle elde edilen algoritmaya göre artıları ve eksileri ortaya konulmuştur.

Bu tezde ele alınan bir diğer konu ise bir ve iki boyutlu DNG malzeme ile yüklü bir ortamın Mur tipi emici sınır koşul ile sonlandırılması için yeni bir formülasyonun geliştirilmiş olmasıdır. Tek yönlü dalga denklemlerinden elde edilen FDTD denklemleri, DNG ortamlar için PLRC yöntemi yardımıyla birinci ve ikinci mertebeden Mur tipi sınır koşulu için tekrar düzenlenmiş ve tüm denklem katsayıları sırasıyla Lorentz ve Drude model parametreleri için ayrı ayrı verilmiştir. Geliştirilen DNG-Mur tipi ABC'nın geçerliliği ve doğruluğu literatürde verilen DNG ortama uyarlanmış Tek Eksenli Mükemmel Uyumlu Tabaka (Uniaxial PML, UPML) tipi ABC ile soğurma performansı ve bellek/hesaplama zamanı gereksinimi açısından karşılaştırılmıştır.

Son olarak, enine ve aynı zamanda eksenel yönler boyunca kayıpsız/kayıplı, özdeş/özdeş olmayan frekansa bağlı elektriksel-manyetik parametrelerle tanımlanmış DNG malzeme ile yüklü dikdörtgen dalga kılavuzundaki yayılma problemi incelenmiştir.

Lorentz tipi DNG malzeme ile enine tabakalanmış bölgelerde geçerli özdeğer denklemi kullanılarak sönen, yayılan ve kompleks dalgalara yönelik çözümler elde edilmiştir. Bu çözümlerden yola çıkılarak farklı özelliklere sahip modal alanlar arasında geçişleri karakterize eden “kesme” olayları incelenmiş, yüzey dalgaları, sönen/ilerleyen dalgalar ve ileri/geri giden dalgalar arasındaki ilişki belirlenmiş, faz ve grup hızlarındaki değişiklikler hesaplanmıştır. Elde edilen sonuçların frekansa, doluluk faktörüne ve dispersif malzeme parametrelerine olan bağımlılıkları değişik örneklerle açıklanmıştır. Yüzey dalgalarının olduğu ve kayıpsız parametreler kullanıldığında karmaşık özdeğerlerin ortaya çıktığı koşullar da ayrıca belirtilmiştir. İletim/yansıma katsayıları ise Mod Eşleştirme Yöntemi kullanılarak kayıplı ve kayıpsız DNG malzemeler için hesaplanmıştır. Eksenel yönde periyodik olarak hava-DNG tabakaları ile yüklü dalga kılavuzundaki elektromanyetik dalga yayılım karakteristiğini incelemek için uygun biçimde genişletilmiş Floquet dalgaları dikkate alınmıştır. Böylece özdeğer ve bant-kenar denklemleri elde edilmiş, dispersiyon ve bant kenarı için nümerik çözümler sunulmuştur. Saçılma karakteristiğinin birim hücre sayısına, sonlandırılmış yapıdaki birim hücre sayısına ve sonlandırma stratejisine bağlılığı örneklerle açıklanmış, hesaplanan yansıma/iletim katsayısı FDTD metodu sonuçları ile karşılaştırılmıştır.

Anahtar Kelimeler: Metamalzemeler, Lorentz model, Mur tipi sınır koşulu, Zaman Bölgesinde Sonlu Farklar, dispersif dalga kılavuzu özçözümleri, faz ve grup hızı, yüzey dalgaları, kompleks dalgalar, Floquet dalgaları.

TABLE OF CONTENTS

ACKNOWLEDGEMENTS	iii
ABSTRACT	iv
ÖZET	vi
TABLE OF CONTENTS	viii
LIST OF FIGURES	x
LIST OF TABLES	xiii
LIST OF ABBREVIATIONS	xiv
LIST OF SYMBOLS	xv
1. INTRODUCTION	1
1.1 Background on Metamaterials	1
1.2 Motivations and Original Contributions	3
1.3 Brief Overview of the Thesis	5
2. FUNDAMENTALS OF METAMATERIALS	7
2.1 Definition	7
2.2 Refractive Index, Wave Impedance and Wave Number of Metamaterials	8
2.3 Unique Properties of DNG Metamaterials	10
2.3.1 Backward waves.....	11
2.3.2 Reversed Snell's Law	11
2.3.3 Reversed Doppler Effect	12
2.3.4 Reversed Vavilov-Cerenkov Radiation.....	13
2.3.5 Frequency dispersion	13
2.4 Dispersive material models.....	14
2.5 Phase velocity and group velocity	18
3. WAVE PROPAGATION IN DNG ENVIRONMENTS USING FINITE DIFFERENCE TIME DOMAIN (FDTD) ALGORITHM	20
3.1 Introduction	20
3.2 Dispersive Finite Difference Time Domain (FDTD) Algorithms	23
3.2.1 Piecewise Linear Recursive Convolution (PLRC).....	25
3.2.2 Auxiliary Differential Equations (ADE).....	29
3.3 Dispersive ADE-FDTD Algorithm for Wave Equation	31
3.4 Termination of DNG Media with Mur's ABC	34
3.4.1 First-order DNG-Mur's ABCs.....	37
3.4.2 Second-order DNG-Mur's ABCs:	41
3.5 Numerical Results.....	47

3.5.1 On propagation characteristics of DNG media	47
3.5.2 On effectiveness of developed DNG-Mur ABC	50
3.5.3 On wave equation based FDTD algorithm	54
4. ANALYTICAL SOLUTIONS OF WAVE PROPAGATION IN A RECTANGULAR WAVEGUIDE LOADED WITH DNG SLABS	58
4.1 Introduction.....	58
4.2 Eigen Solutions in DNG Loaded Regions	59
4.3 Determination of Modal Cut-off Frequencies	63
4.4 Properties of Dispersion Diagrams	63
4.4.1 Propagating and Evanescent Waves (Lossless and Lossy Cases).....	64
4.4.2 Complex eigenvalues in lossless case	67
4.4.3 Phase and Group Velocities	69
4.4.4 Surface Wave Type Solutions	72
4.5 Mode Matching Solution of Scattering from Partially Loaded Sections.....	75
4.6 Scattering Characteristics of Fully Loaded Sections	79
4.7 Numerical Results for Reflection-Transmission Characteristics.....	81
4.8 Multiple DNG Loaded Sections Along Axial Direction	85
5. CONCLUSIONS.....	92
REFERENCES.....	97
APPENDICES	106
Appendix A. ADE-FDTD Update Equations in Two Dimension (2D)	106
Appendix B. Modified UPML in DNG media (DNG- UPML).....	109
Appendix C. S-Matrix Representation.....	117
CIRRICULUM VITAE.....	121

LIST OF FIGURES

Figure 2.1 Material classification.	7
Figure 2.2 Definitions in the complex plane for (a) $\epsilon_r = \epsilon' - j\epsilon''$, $\mu_r = \mu' - j\mu''$ and (b) square roots of wave impedance and refractive index for DNG media.	9
Figure 2.3 Configuration of a) RH triplets and b) LH triplets in terms of E, H, S and k.	11
Figure 2.4 Snell's law for DPS and DNG media: Ray propagation through two different media.	12
Figure 2.5 a)Refractive index, b) Phase velocity and c) Group velocity versus frequency for the parameters given in Table 2.2.	19
Figure 3.1 Positions of the field components in a unit cell of the Yee's lattice	21
Figure 3.2 Flow chart of PLRC-FDTD procedure.....	29
Figure 3.3 Flow chart of ADE-FDTD procedure	31
Figure 3.4 Plot of E-field vs. position and time at three different nodes using 1D ADE-FDTD algorithm	48
Figure 3.5 The 2D FDTD scenario and the location of the metamaterial region	49
Figure 3.6 Propagation through DNG slab with $n=-1$ a) Focusing and b) Direction of propagation	49
Figure 3.7 The time history and frequency spectrum of the electric field E_z (E_{inc}) measured at the center of the computational grid	50
Figure 3.8 Snapshots of E_z field using 2 nd order DNG-Mur at time-steps: a)1250, b)2500 and c)10000	51
Figure 3.9 Comparison of DNG-Mur and DNG-UPML for 1D and 2D scenarios	52
Figure 3.10 a)Snapshot of propagation and b) E field recorded at an observation point when DNG slab boundaries are truncated with DNG - Mur.	53
Figure 3.11 a)Snapshot of propagation and b) E field recorded at an observation point when DNG slab boundaries are truncated with Standard Mur.	53
Figure 3.12 Comparison of 1D FDTD algorithm based on wave and curl equations in Lorentz type DNG medium.	55
Figure 3.13 The Gaussian pulse propagating toward the ENG medium (at $t=500\Delta t$) and reflecting from the free space-ENG medium interface (at $t=1000\Delta t$)	56

Figure 3.14 a) Real and imaginary part of permittivity, b) Reflection coefficients vs. frequency	57
Figure 4.1 Configuration of rectangular waveguide filled with a) three-layers (front view), b) two-layers and c) single layer where regions (I-III) are free space and region (II) is DNG slab (top view).....	59
Figure 4.2 Continuity and discontinuity of fields at air-slab interfaces.....	60
Figure 4.3 Real part of relative permittivity versus frequency which has refractive index about -1 for Scenario I at $f_s=9\text{GHz}$ and $f_s=13\text{GHz}$	62
Figure 4.4 Variation of cut-off frequencies versus t/a for Scenario I where a) $f_{se}=f_{sm}=f_s=9\text{GHz}$ and b) $f_{se}=f_{sm}=f_s=13\text{GHz}$ (horizontal line).	63
Figure 4.5 Dispersion diagrams of TE modes for a) fully loaded DNG slab ($t=0$) and partially loaded DNG slab when the thickness of air (t) is equals to b) $a/4$, c) $a/3$, d) $a/2$, e) $3a/4$ and f) $2a/3$	65
Figure 4.6 Dispersion diagrams of propagating modes in lossy case for (a) $f < f_s$, around $f_c=8.26\text{GHz}$ and (b) for $f > f_s$, around $f_c=10.95\text{GHz}$	66
Figure 4.7 Dispersion diagrams of propagating modes in lossy case around f_s	66
Figure 4.8 a) Propagating mode turns at a certain frequency which yields complex eigenvalues around that turning point, b) Real and imaginary parts of one of the complex β	68
Figure 4.9 Dispersion diagram calculated with parameters (see text) given in (Cory & Shtrom, 2004): Propagating (blue solid) and one of the complex waves: real part (black dash) and imaginary part (red dot).	69
Figure 4.10 Dispersion diagram and phase/group velocities in a rectangular waveguide loaded with DNG slab with a ratio of $t/a=0, 1/4$ and $3/4$	71
Figure 4.11 (a) Propagating mode turns at a certain frequency (b) group /phase velocities for complex β solutions and (c) E-field distribution along x-axis where DNG slab has $n=-1$ at $f_s=13\text{GHz}$ and $t=3a/4$	72
Figure 4.12 Surface waves along DNG-air interface along x-axis for (a) $t=a/4$ and (b) $t=3a/4$ where DNG slab has negative refractive index about -1 at $f_s=9\text{GHz}$. ..	74
Figure 4.13 Dispersion diagrams of propagating modes for non-identical parameters when $t=a/4$ and $3a/4$	74
Figure 4.14 Dispersion diagrams of propagating modes for Scenario I and II.....	75

Figure 4.15 Reflection and transmission coefficients of DNG slab for a) $t=0.75a$, b) $t=a$ and c) $t=2a$ along z-direction	82
Figure 4.16 a)Analytic solution, b) FDTD solution of scattering parameters with/without losses for fully loaded single DNG slab with a length of $t=0.75a$	82
Figure 4.17 a)Refractive index and reflection/transmission coefficient in a rectangular waveguide loaded with double DNG slab calculated with b) Analytic solution and c) FDTD solution	83
Figure 4.18 Reflection and transmission coefficients for lossless/lossy cases when a) $t=a/4$ and b) $t=3a/4$	84
Figure 4.19 a)Reflection and transmission coefficients for lossless and lossy cases between 7-8GHz and b) mode convergence for lossless case at 8GHz.....	84
Figure 4.20 Transmission line representation for TE_{10} mode of DPS/DNG loaded rectangular waveguide	85
Figure 4.21 Periodic Structure and its Symmetric Unit Cell (UC).....	86
Figure 4.22 a) Band edge diagram and b) Stop-Pass band frequency intervals for $d/p=0.3$	88
Figure 4.23 Power Reflection Transmission Characteristics of a) Unit Cell (UC), b) 5 cascaded UC's and c) 15 cascaded UC's (Parameter values used in the calculations are same as those used for Figure 4.22).....	90
Figure 4.24 Transmission coefficient for a) lossless case and b) lossy case	90
Figure 4.25 Power Reflection Transmission Characteristics of 15 cascaded UC's a) without tapering and b) with 3 tapering section on each side.	91

LIST OF TABLES

Table 2.1 Arguments of ε, μ, n and ζ in each medium.....	10
Table 2.2 Different Lorentz parameters which yield NIM about $n=-1$ at $\omega = \omega_s$	19
Table 3.1 Parameters for Drude and Lorentz Model in 1 st order DNG-Mur ABC.....	40
Table 3.2 Parameters for Drude and Lorentz Model in 2 nd order DNG-Mur ABC.....	46
Table 3.3 Memory usage and computation time in FDTD simulations.....	52
Table 3.4 Memory / time requirements of FDTD simulations based on wave and curl equations.....	55
Table 4.1 Lorentz Model Parameters.....	62
Table 4.2 Lorentz Model Parameters for DNG Media.....	83

LIST OF ABBREVIATIONS

ABC	:	Absorbing Boundary Condition
ADE	:	Auxiliary Differential Equation
CFL	:	Courant Friedrichs Lewy
CFS PML	:	Complex Frequency Shifted PML
DNG	:	Double Negative
DPS	:	Double Positive
ENG	:	Epsilon Negative
FDTD	:	Finite Difference Time Domain
LHM	:	Left Handed Medium
LSE, LSM	:	Longitudinal Section Electric and Longitudinal Section Magnetic
MNG	:	Mu Negative
MTM	:	Metamaterial
NIM	:	Negative Index Materials
PLRC	:	Piecewise Linear Recursive Convolution
PML	:	Perfectly Matched Layer
RC	:	Recursive Convolution
RHM	:	Right Handed Medium
SNG	:	Single Negative
TE, TM	:	Transverse Electric and Transverse Magnetic
UC	:	Unit Cell
UPML	:	Uniaxial PML
ZT	:	z-transform
1D, 2D, 3D	:	One-Dimensional, Two-Dimensional and Three-Dimensional

LIST OF SYMBOLS

n	refractive index
θ_i, θ_t	incident and refracted angles
η	wave impedance
ζ	normalized wave impedance
η_o	free space impedance
k	wave number
k_i	propagation factor along i-direction (i=x, y, z)
k_o	free space wave number
κ	propagation constant of the periodic structure
ω	angular frequency
c	speed of light
ε, μ	permittivity and permeability of the medium
ε_o, μ_o	permittivity and permeability of free space
ε_r, μ_r	relative permittivity and permeability
χ_e, χ_m	electric and magnetic susceptibilities
ω_{pe}, ω_{pm}	electric and magnetic plasma frequencies
ω_{oe}, ω_{om}	electric and magnetic resonance frequencies
Γ_e, Γ_m	electric and magnetic damping coefficients
$\sigma_{e,m}$	electric and magnetic conductivity
f_s	reference frequency where refractive index is -1
f_c	cutoff frequency

\vec{E}, \vec{H}	electric field and magnetic field vectors
\vec{D}, \vec{B}	electric and magnetic flux density vectors
\vec{S}	poyniting vector
\vec{P}, \vec{M}	electric and magnetic polarizations
E, H	magnitude of electric field and magnetic field vectors
D, B	magnitude of electric and magnetic flux density vectors
v_p	phase velocity
v_g	group velocity
S_{11}, S_{21}	S parameters
R	reflection coefficient
T	transmission coefficient
$Z_{TE, TM}$	impedance of TE/TM mode
Y_n	admittance of n th mode

1. INTRODUCTION

1.1 Background on Metamaterials

The materials with negative permittivity and permeability was first theoretically introduced by Veselago (Veselago, 1968), where it was pointed out that these kinds of materials would have unusual characteristics, such as negative index of refraction and backward wave propagation which are not observed readily in nature. After decades, Pendry et al., experimentally demonstrated that a composite medium of periodically placed thin metallic wire structures exhibit negative permittivity (ϵ) (Pendry et al., 1996; 1998) and periodic metallic split ring resonators (SRR) exhibit negative effective permeability (μ) over a certain frequency band (Pendry et al., 1999; 2002a; 2002b). In 2000, Smith et al. combined these two structures in a single configuration to create a material possessing negative index of refraction for a band of frequency in the GHz range (Smith & Kroll, 2000; Schultz et al., 2000). The experimental verification of first negative refractive index materials was performed at microwave frequency by Shelby et al. (Shelby, Smith, & Schultz, 2001).

Recently, many researchers have studied various shapes of split ring resonators (SRRs) (such as axially symmetric rings, triangular, S-shaped, V-shaped, omega shaped...etc.) other than the circular or rectangular rings to generate effective dispersive permeability. Hence, new double-negative (DNG) structures are realized from the arrangement of these SRRs and wires as in Smith's design or SRRs alone printed on each side of circuit board to achieve negative refractive index (Sabah, 2010; Chen, Ran, Huangfu, Zhang, & Chen, 2004; Kishor, Baitha, Sinha, & Lahiri, 2014; Li, Aydin, & Ozbay, 2010). Although the SRRs and wires geometry has become very widely used in microwave regime, this configuration has certain disadvantages at infrared and optical regimes due to required micron and submicron length-scale structures. Therefore, alternative designs are developed to achieve simultaneously negative permittivity and permeability at THz and optical frequencies (Shalaev et al., 2005; Zhou et al., 2006; Gundogdu et al., 2008; Kafesaki et al., 2007; Zhang et al., 2005; Chettiar et al., 2007; Jakšić, Dalarsson, & Maksimović, 2006).

Since these kinds of materials have unusual characteristics, such as, inverse Snell effect, inverse Doppler effect and backward Cerenkov radiation, DNG materials opened a wide potential for applications in diverse areas such as cloaking, imaging, acoustics, absorbers, antennas and guiding structures. In 2000, Pendry (Pendry, 2000) showed that the property of negative - refraction index can be used in making perfect lenses. A perfect lens may be described as an optical or electromagnetic element which forms image using both propagating and evanescent modes, resulting in an almost perfect image of the original. Moreover, Schurig et al. (Schurig et al., 2006) suggested cloaking materials which bend electromagnetic waves around objects so that the object appears invisible. The trick is to continuously change the material parameters ϵ and μ , as a function of the radius. This process can be seen as a coordinate transform that stretches and compresses space in order to introduce a place where no electromagnetic radiation can go. Thus objects inside the cloak cannot be seen from the outside.

On the other hand, since the wave in Left Handed Metamaterials (LHMs) propagates in the backward direction LHMs can be employed to design a phase shifter, which exhibits a linear phase response with frequency (Antoniades & Eleftheriades, 2003). Especially, the phase of the wave can be kept unchanged after the wave passes through one double-positive (DPS) slab and one DNG slab that have the same thickness and same absolute value of refractive index but opposite sign. This property may be applied to construct zero phase delay transmission line to feed antenna arrays. In antenna applications (Ziolkowski & Kipple, 2003; Mittra, Rajab, & Lanagan, July 2005), anisotropic metamaterial cover is used to improve the performance of the antenna by providing high directivity, good matching with an input source, and a tunable operational frequency. Thus, an electrically small antenna can be obtained with large radiated power.

Detailed overview of various geometries used in metamaterial design and their applications in microwave, optical and terahertz regions are given in (Capolino, 2009; Eleftheriades & Engheta, *Metamaterials: Fundamental*, 2011; Tretyakov et al., 2017).

1.2 Motivations and Original Contributions

This thesis is concerned with the numerical and analytical studies on DNG media such as: i) applying dispersive finite difference time domain (FDTD) approaches to DNG media (i.e. to terminate the DNG boundary and obtain the minimum computational time/memory requirements during the simulation) ii) analysis of rectangular waveguide filled with DNG slab (i.e. to investigate the dispersion diagrams and cut-off transitions properties, scattering characteristics in single and periodic loaded structures). In the following motivations and contributions of each issue is explained in details.

The boundary conditions play an important role in FDTD calculations, as it is necessary to terminate the computational domain that ideally absorbs the incident field without producing any reflections. The most widely used boundary conditions are Mur (Mur, 1981) and perfectly matched layer (PML) absorbing boundary conditions (ABCs) first introduced in (Berenger, 1994). Although PML performance yields significantly better results than Mur's ABC for a wider range of incident angles, Mur's ABC may be preferred due to its computational efficiency and the simplicity of its implementation whenever the level of reflections can be tolerated. However, in the presence of DNG media special care is required in implementing ABCs to ensure stability. In literature, one can find several studies on the use of PML in DNG media. The contribution of this thesis to this area is the formulation of first and second order Mur's ABC, developed from frequency domain one-way wave equations using piecewise linear recursive convolution (PLRC) FDTD algorithm for truncating the DNG media characterized by Lorentz or Drude model. The numerical examples for a domain filled entirely with Lorentz type DNG material are also presented to demonstrate the stability and accuracy of the proposed formulations which show that reflections effectively reduce about -50dB.

The second contribution to the dispersive FDTD formulations is the wave equation based FDTD and supporting numerical results for epsilon-negative (ENG) and DNG media described by Lorentz model. (Ozakın & Aksoy, 2013) developed a wave equation based FDTD formulation involving only Debye model and recursive convolution (RC) approach. However, auxiliary differential equation (ADE) and PLRC FDTD formulations for ENG medium described by Lorentz model, using wave equation was first established by (Pekmezci, Topuz, & Sevgi, 2016) and the numerical results of the proposed approach will be expressed and discussed. In this thesis, FDTD algorithm based on the wave

equation for DNG medium is obtained using ADE approach, and its performance is compared with the curl equation based formulations. For both simulations, computational domain is entirely filled with Lorentz type DNG medium and terminated by the proposed DNG-Mur's ABC.

The contributions made to the investigation of the characteristics of modal fields supported by a parallel plate waveguide partially or fully loaded with a homogeneous DNG slab are listed below. There are several reports in the literature investigating propagation characteristics and potential applications of metamaterial loaded planar and rectangular waveguides (Alu & Engheta, 2004; Engheta, 2002; Nefedov & Tretyakov, 2003; Cory & Shtrom, 2004; Baccarelli et al., 2005; Yongmei & Shanjia, 2009). It has already been shown that, in certain frequency and parameter regions such environments support forward, backward and surface wave type solutions and yield complex values of propagation constant in the absence of losses. These investigations are focused on problems dealing with specific applications or propagation characteristics, often using the rather restrictive assumption of nondispersive DNG media. Alu and Engheta (Alu & Engheta, 2004) presented a comprehensive analytical analysis and numerical results for the modes propagating in bilayer parallel plate waveguide loaded with pairwise combinations of lossless single negative ($\epsilon > 0, \mu < 0$ or $\epsilon < 0, \mu > 0$), DPS and DNG slabs of arbitrary thicknesses at fixed frequency (i.e., for constant values of constitutive parameters). Nefedov and Tretyakov (Nefedov & Tretyakov, 2003) investigated DPS-DNG slab combinations with several layer thicknesses and presented numerical results for dispersion characteristics of propagating modes over wide frequency bands assigning constant values to material parameters. Cory and Shtrom (Cory & Shtrom, 2004) addressed DPS-DNG slab configuration in a parallel plate waveguide of given plate separation and presented numerical results of modal dispersion for different values of geometrical loading factor (t/a in Figure 4.1b) over wide frequency bands, also using constant values for material parameters. Using Drude-Lorentz models Baccarelli et.al. (Baccarelli et al., 2005) presented a detailed analysis of surface waves on grounded metamaterial (MTM) slabs, and Yongmei and Shanjia (Yongmei & Shanjia, 2009) investigated complex modes in MTM loaded parallel plate waveguide. In this thesis a holistic approach is presented for investigating the effects of the geometrical filling factor, medium dispersion and losses. Novel contributions are made on the existence conditions, dispersive properties of evanescent, propagating and complex modes supported by the

parallel plate waveguide partially loaded along x-direction and on the properties of different types of modal cut-off transitions. The equations for obtaining reflection and transmission characteristics are desired for X-band rectangular waveguide fully/partially loaded in the cross-section with Lorentz type DNG media, and numerical results are presented. Another contribution made to the propagation characteristics of loaded waveguide is the investigation of the structures containing alternating DPS/DNG regions in the axial direction. In this context emphasis is given on “periodic-like” (truncated periodic) structures. It is shown that both Floquet eigenvalue and the band-edge equations need to be appropriately modified to account for the presence of DNG media, and numerical results are presented.

1.3 Brief Overview of the Thesis

This thesis focuses on the study of propagation of electromagnetic waves in the presence of metamaterials (MTMs) using Finite Difference Time Domain (FDTD) algorithm for addressing certain features directly in the time domain and exact analytical approach for investigating salient properties of wave fields in MTM loaded canonical waveguide environments in the frequency domain. Comparison of results obtained via analytical and numerical methods are also presented for certain scenarios, the former providing benchmark solutions for validating the latter.

Following this introducing chapter, in Chapter 2 we present a brief review of the characteristics of single and double negative media. Definitions and relations needed in the subsequent chapters such as those for the refractive index, wave impedance, wave number and dispersion models are given together with the unique properties of waves in DNG materials.

In Chapter 3, non-dispersive FDTD update equations based on Maxwell’s curl and wave equation and two of dispersive FDTD algorithms (ADE and PLRC) applicable to electromagnetic wave propagation through DNG media are reviewed. We then present formulation utilizing wave equation in DNG media based on ADE-FDTD approach and pros/cons of proposed formulation over FDTD algorithm based on curl equations. Finally, modified formulation of first and second order Mur’s absorbing boundary conditions (ABCs) for terminating DNG media obtained from frequency dependent one-way wave equations using piecewise linear recursive convolution (PLRC) method are presented.

The validity and stability of the proposed DNG-Mur formulations are demonstrated via numerical examples considering 1D and 2D problems entirely loaded with Lorentz type DNG media, and also its advantages over uniaxial perfectly matched layer (UPML) in terms of computational time and memory requirements.

In Chapter 4, exact frequency domain formulations are derived for eigenwaves supported in uniform, 1D reducible waveguide environments and partially loaded with DNG media along a transverse or along the axial directions. Numerical results for β/k_0 diagrams are presented for lossless/lossy DNG slab modelled by identical/non-identical Lorentz type permittivity and permeability. The phase and group velocities are calculated and drawn for several problem scenarios. Cut-off transitions between evanescent, propagating, complex and surface wave type solutions are investigated and novel conditions are obtained for emergence of complex and surface wave type eigensolutions. Analytic solutions of reflection and transmission coefficients are obtained for single mode supporting waveguide sections fully/partially loaded with DNG slabs in one transverse direction and also for axially periodically arrangement. Numerical results obtained from analytical formulations are compared with the FDTD simulations.

The final chapter, Chapter 5, provides a summary of the results obtained and the contributions made in this work, and concludes with suggestions of future areas of research which stand out as promising follow-up paths of this thesis.

2. FUNDAMENTALS OF METAMATERIALS

2.1 Definition

Metamaterials (MTMs) are periodic structures which are artificially constructed to exhibit extraordinary electromagnetic properties that cannot be found in nature. In a lossless medium, electromagnetic properties are determined by the macroscopic parameters, permittivity and permeability of materials (Ramakrishna, 2005). Therefore, a medium can be classified in four groups depending on their constitutive parameters as shown in Figure 2.1 (Engheta & Ziolkowski, 2006).

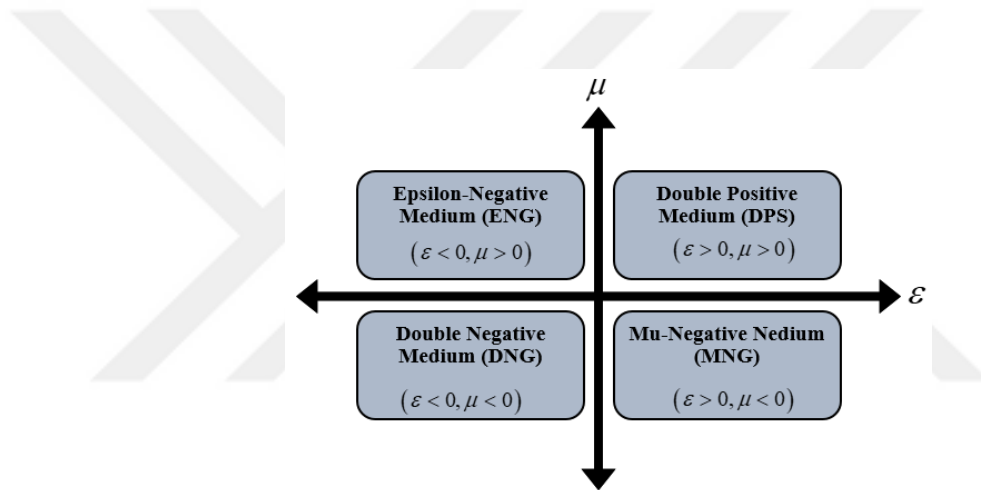


Figure 2.1 Material classification.

Medium with positive permittivity and permeability is referred to as double-positive medium (DPS) and most of the materials in nature are in this group. The propagation of electromagnetic waves is possible in such materials. Medium possessing at least one negative constitutive parameter is referred to as single-negative medium (SNG) and classified into two subcategories namely epsilon-negative (ENG) and mu-negative (MNG) media. The propagation of electromagnetic waves is not possible in such media. In certain frequency regimes, many plasmas and noble metals (such as gold and silver) exhibit negative permittivity behavior, and ferromagnetic materials exhibit negative permeability behavior. Some artificial materials can also be constructed to exhibit DPS, ENG, and MNG properties (Hao & Mittra, 2009). Propagation of electromagnetic waves is also possible in the last group composed of simultaneously

negative permittivity and permeability is named as double-negative medium (DNG), and such a material have not been discovered yet in nature. Hence, this class of materials has only been constructed artificially.

2.2 Refractive Index, Wave Impedance and Wave Number of Metamaterials

The general definition of refractive index (n), wave impedance (η) and wave number (k) are given as :

$$n = \sqrt{\epsilon_r \mu_r} \quad (2.1)$$

$$\eta = \sqrt{\mu/\epsilon} = \sqrt{\mu_o \mu_r / \epsilon_o \epsilon_r} = \eta_o \sqrt{\mu_r / \epsilon_r} \quad (2.2)$$

$$k = \omega \sqrt{\epsilon \mu} = \omega \sqrt{\epsilon_o \epsilon_r \mu_o \mu_r} = n k_o = n \omega / c \quad (2.3)$$

where $\omega = 2\pi f$ is the angular frequency, $\eta_o = \sqrt{\mu_o / \epsilon_o}$ is the free space impedance, $k_o = \omega / c$ is the free space wave number, $c = 1 / \sqrt{\epsilon_o \mu_o}$ is the speed of light, $\epsilon_r = \epsilon / \epsilon_o$ and $\mu_r = \mu / \mu_o$ are the relative permittivity and permeability, respectively.

In a dispersive medium with $e^{j\omega t}$ time dependence assumption, the constitutive parameters are expressed in complex domain and can be written in polar form as

$$\epsilon_r = |\epsilon_r| e^{j\phi_e} = \epsilon' - j\epsilon'' \quad ; \quad \mu_r = |\mu_r| e^{j\phi_m} = \mu' - j\mu'' \quad (2.4)$$

Using the preceding expressions given in Equation (2.4), refractive index and wave impedance of a dispersive medium can be defined as

$$n = \sqrt{\epsilon_r \mu_r} = |\epsilon_r|^{1/2} |\mu_r|^{1/2} (e^{j\phi_e/2} e^{j\phi_m/2}) = \sqrt{|\epsilon_r| |\mu_r|} (e^{j(\phi_e + \phi_m)/2}) = |n| e^{j\phi_n} \quad (2.5a)$$

$$\eta = \eta_o \sqrt{\frac{\mu_r}{\epsilon_r}} = \eta_o \frac{|\mu_r|^{1/2}}{|\epsilon_r|^{1/2}} \left(\frac{e^{j\phi_m/2}}{e^{j\phi_e/2}} \right) = \eta_o \sqrt{\frac{|\mu_r|}{|\epsilon_r|}} \left(e^{j(\phi_m - \phi_e)/2} \right) = \eta_o |\zeta| e^{j\phi_\zeta} \quad (2.5b)$$

where

$$|n| = \sqrt{|\epsilon_r| |\mu_r|} \quad ; \quad \phi_n = \frac{1}{2}(\phi_e + \phi_m) \quad (2.6a)$$

$$|\zeta| = \sqrt{\frac{|\mu_r|}{|\epsilon_r|}} \quad ; \quad \phi_\zeta = \frac{1}{2}(\phi_m - \phi_e) \quad (2.6b)$$

The definitions of refractive index and wave impedance involves square roots, the sign of which should be defined properly so as to satisfy causality and Poynting theorem in a linear dispersive medium. This choice is investigated in detail in (Veselago et al., 2006; Heyman & Ziolkowski, 2001; Irci, 2007; Alu & Engheta, 2005) for all types of media (DPS, SNG and DNG) and the proper branch which gives the physically correct solution is determined. Definitions for constitutive parameters, square roots of refractive index and normalized wave impedance in the complex plane, Equations (2.4-2.5), are illustrated in Figure 2.2 and arguments of ϵ, μ, n and ζ for different types of media are given in Table 2.1.

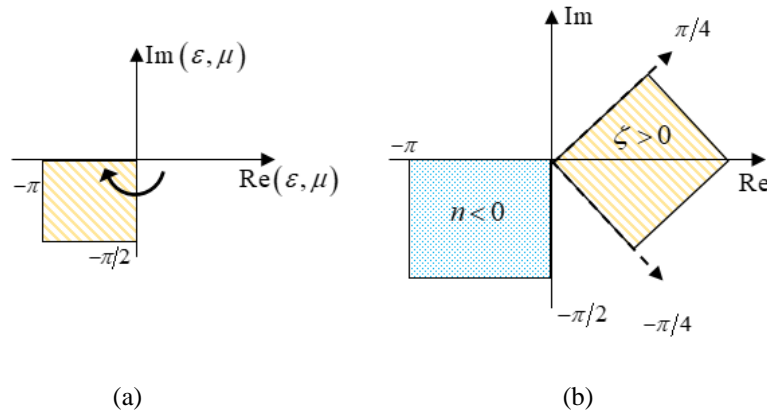


Figure 2.2 Definitions in the complex plane for (a) $\epsilon_r = \epsilon' - j\epsilon''$, $\mu_r = \mu' - j\mu''$ and (b) square roots of wave impedance and refractive index for DNG media.

Table 2.1 Arguments of ε, μ, n and ζ in each medium.

	$\varepsilon_r = \varepsilon' - j\varepsilon''; \mu_r = \mu' - j\mu''$			
	ϕ_ε	ϕ_μ	ϕ_n	ϕ_ζ
DPS	$[0, -\pi/2)$	$[0, -\pi/2)$	$[0, -\pi/2)$	$(\pi/4, -\pi/4)$
ENG	$(-\pi/2, -\pi]$	$[0, -\pi/2)$	$(-3\pi/4, -\pi/4)$	$(0, \pi/2]$
MNG	$[0, -\pi/2)$	$(-\pi/2, -\pi]$	$(-3\pi/4, -\pi/4)$	$[-\pi/2, 0)$
DNG	$(-\pi/2, -\pi]$	$(-\pi/2, -\pi]$	$(-\pi/2, -\pi]$	$(\pi/4, -\pi/4)$

From the table given above, one can conclude that all lossless conventional materials (DPS) with positive ε_r and μ_r (where $\phi_\varepsilon = \phi_\mu = 0$) yield positive refractive index and wave impedance. In the case of medium possessing at least one negative constitutive parameter (ENG or MNG), the refractive index and wave impedance have imaginary values, resulting in imaginary wave vectors and evanescent waves. However, for DNG materials in which real part of ε_r and μ_r (where $\phi_\varepsilon = \phi_\mu = -\pi$) are simultaneously negative, refractive index has opposite sign relative to DPS materials (Veselago, 1968). Consequently, these materials are denoted as Negative Index Materials (NIM) and the expression of n for a lossless DNG material is:

$$n = \sqrt{|\mu_r||\varepsilon_r|} e^{\pm j2\pi} = \sqrt{|\mu_r||\varepsilon_r|} e^{\pm j\pi} = -\sqrt{|\mu_r||\varepsilon_r|} \quad (2.7)$$

2.3 Unique Properties of DNG Metamaterials

The media with simultaneously negative permittivity and permeability must have negative refractive index as noted in the previous section. This causes some unusual characteristics such as backward wave propagation, reversed Snell's law, reversed Doppler effect, etc. In the following, brief explanation about these basic properties will be presented.

2.3.1 Backward waves

In DPS media, electric field (E), magnetic field (H) and wave vector (k) form a right handed set of vectors, and are also named as Right-handed Medium (RHM). However, in DNG media, negative refractive index causes a reversal wave vector using Equation (2.3), and E, H and k form a left-handed triplet coined by Veselago (Veselago, 1968) as Left-handed Medium (LHM).

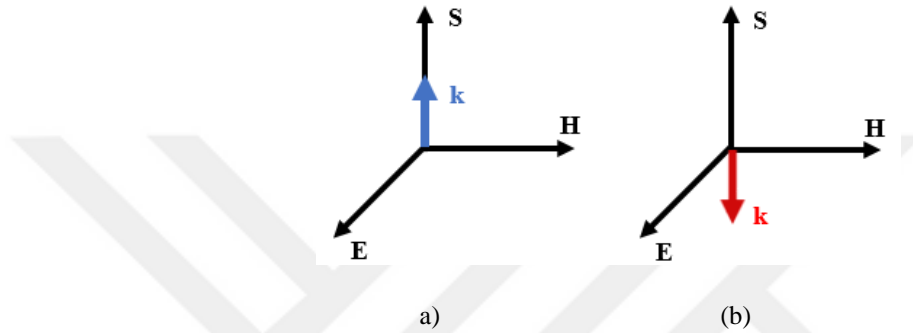


Figure 2.3 Configuration of a) RH triplets and b) LH triplets in terms of E, H, S and k.

Although E, H and k form a left handed triplet, E, H and Poynting vector (S) always maintain a right handed relationship (Veselago, 1968). Thus, the wave vector is antiparallel to the Poynting vector in a LHM. Illustration of right and left hand relations between E, H, S and k are given in Figure 2.3. Since the direction of the wave vector coincides with the direction of phase velocity and that of the Poynting's vector with the group velocity, waves propagating in LHM materials are called backward waves.

2.3.2 Reversed Snell's Law

The sign of the refraction index has an important role to fulfil the passage of rays through one medium to another. Applying the usual Snell's law, refracted angle is obtained as (Veselago, 1968)

$$n_1 \sin \theta_i = n_2 \sin \theta_t \rightarrow \theta_t = \sin^{-1} \left(\frac{n_1}{n_2} \sin \theta_i \right) \quad (2.8)$$

Here, n_1, n_2 are the refractive indices of two media and θ_i, θ_r are the incident and refracted angles, respectively. If both n_1 and n_2 are positive valued then θ_i is positive, while $n_1 > 0$ and $n_2 < 0$, then θ_i is negative. Although the direction of reflected ray is the same independent of the refractive index sign, the refracted wave in NIM is bent on the opposite side to that observed in DPS medium. In Figure 2.4, comparison of ray propagation in a NIM to that in a DPS medium is illustrated with ray paths where the path 1-4 corresponds to positive refraction and the path 1-3 is negative refraction. Therefore, the negative refraction at the interface of two media having opposite sign of refractive indices can also be thought to be a consequence of reversed Snell's law.

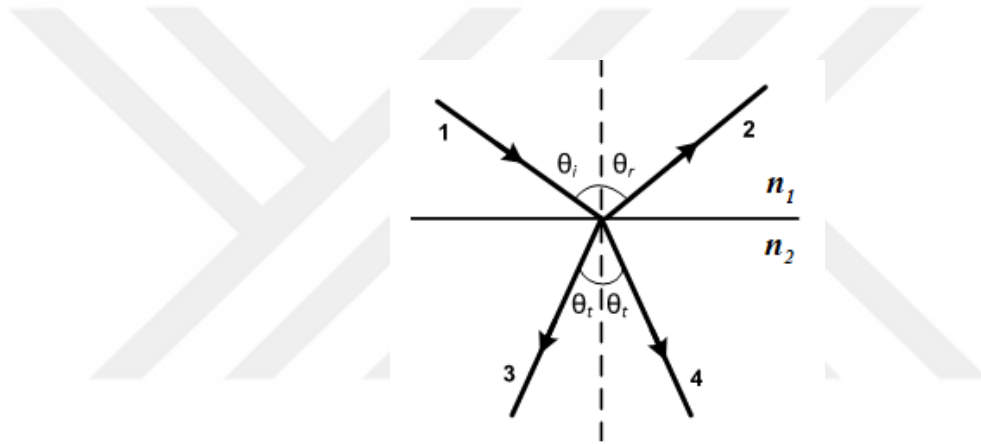


Figure 2.4 Snell's law for DPS and DNG media: Ray propagation through two different media.

1) incident ray; 2) reflected ray; 3) refracted ray if $n_2 < 0$; 4) refracted ray if $n_2 > 0$.

2.3.3 Reversed Doppler Effect

The Doppler effect is a fundamental frequency shift phenomenon that occurs whenever a wave source and an observer are moving with respect to one another. The frequency detected by the observer can be calculated simply as

$$f_1 = f_o \left(1 - n \frac{v}{c} \right) \quad (2.9)$$

where c is the speed of light in a vacuum and v is the relative velocity between source and observer with a positive sign as the observer is going away from the source. If the

refractive index (n) of the medium is positive (DPS), detected frequency (f_1) by the observer is smaller than the source frequency (f_0), while if the media has negative refractive index (DNG), then one encounters the opposite behavior. This means that, observer which is receding from the source detects higher frequency than the source frequency. The experimental observation of the inverse Doppler shift can be found in (Seddon & Bearpark, 2003; Chen et al., 2011).

2.3.4 Reversed Vavilov-Cerenkov Radiation

The Vavilov-Cerenkov radiation occurs as a charged particle moves in a medium faster than the speed of light in that medium and the radiated spherical wave fronts travel forward making an angle θ with the particle velocity v . The expression of this radiation angle is given by

$$\cos\theta = \frac{c/n}{v} \quad (2.10)$$

where c/n is the velocity of light in that medium and v is the velocity of the particle. In an ordinary medium where $n > 0$, this angle is always positive. However, if the medium has a negative refractive index $n < 0$, the radiation angle should be in the region of $[\pi/2, \pi]$ and resulting wave fronts travel backward with an obtuse angle relative to the direction of the particle. Details about reversed Cerenkov Radiation can be found in (Eleftheriades & Grbic, 2002; Lu et al., 2003; Chen & Chen, 2011; Duan, Wu, Chen, Xi, & Chen, 2009; Galyamin & Tyukhtin, 2010).

2.3.5 Frequency dispersion

For a non-dispersive medium in which the refractive index does not change with frequency, the energy density has the following form:

$$W = \frac{1}{2}(\varepsilon|E|^2 + \mu|H|^2) \quad (2.11)$$

For simultaneously negative ε and μ the total energy density calculated from Equation (2.11) would be negative, in conflict with the conservation law of energy. Therefore, Veselago (Veselago et al, 2006) stated that a DNG medium should be dispersive. When frequency dispersion exists, the energy density relation must be modified as

$$W = \frac{1}{2} \left[\frac{d(\omega\varepsilon)}{d\omega} |E|^2 + \frac{d(\omega\mu)}{d\omega} |H|^2 \right] = \frac{1}{2} \left[(\varepsilon|E|^2 + \mu|H|^2) + \left(\frac{d\varepsilon}{d\omega} |E|^2 + \frac{d\mu}{d\omega} |H|^2 \right) \right] \quad (2.12)$$

According to this expression, positive energy density is obtained for simultaneously negative ε and μ , as long as their partial derivatives with respect to the frequency are sufficiently greater than zero. Hence, one can conclude that for the possibilities of practical realization of materials with negative ε and μ , it is necessary to consider that such materials must possess frequency dispersion. In the following section, commonly used dispersive models for both ε and μ to characterize realistic DNG materials are briefly reviewed.

2.4 Dispersive material models

The correlation between electric field intensity E and electric flux density D , and similarly magnetic field intensity H and magnetic flux density B is described by the constitutive parameters. In free space the electric field and magnetic field are directly proportional to the electric and magnetic flux density by a factor of the free-space permittivity (ε_0) and permeability (μ_0), respectively. When an electromagnetic field interacts with matter it induces electric/magnetic dipole moments in the material, and creates electric/magnetic polarization which are functions of electric/magnetic susceptibilities. Hence, in a non-dispersive medium the constitutive equations can be expressed as:

$$\vec{D} = \varepsilon \vec{E} = \varepsilon_o \varepsilon_r \vec{E} = \varepsilon_o \vec{E} + \vec{P} \quad (2.13a)$$

$$\vec{B} = \mu \vec{H} = \mu_o \mu_r \vec{H} = \mu_o \vec{H} + \vec{M} \quad (2.13b)$$

where

$$\varepsilon_r = 1 + \chi_e \quad ; \quad \mu_r = 1 + \chi_m \quad (2.14)$$

$$\vec{P} = \varepsilon_o \chi_e \vec{E} \quad ; \quad \vec{M} = \mu_o \chi_m \vec{H} \quad (2.15)$$

Here, ε_r and μ_r are the relative permittivity and permeability, \vec{P} and \vec{M} are the electric and magnetic polarizations, χ_e and χ_m are the electric and magnetic susceptibilities, respectively.

However, since the permittivity $\varepsilon(\omega)$ and permeability $\mu(\omega)$ are frequency dependent parameters in dispersive media, the constitutive equations are also frequency dependent and expressed as in the following form:

$$\vec{D}(\omega) = \varepsilon(\omega) \vec{E}(\omega) = \varepsilon_o \varepsilon_r(\omega) \vec{E}(\omega) = \varepsilon_o \varepsilon_\infty \vec{E}(\omega) + \vec{P}(\omega) \quad (2.16a)$$

$$\vec{B}(\omega) = \mu(\omega) \vec{H}(\omega) = \mu_o \mu_r(\omega) \vec{H}(\omega) = \mu_o \mu_\infty \vec{H}(\omega) + \vec{M}(\omega) \quad (2.16b)$$

where

$$\varepsilon_r(\omega) = \varepsilon_\infty + \chi_e(\omega) \quad ; \quad \mu_r(\omega) = \mu_\infty + \chi_m(\omega) \quad (2.17)$$

$$\vec{P}(\omega) = \varepsilon_o \chi_e(\omega) \vec{E}(\omega) \quad ; \quad \vec{M}(\omega) = \mu_o \chi_m(\omega) \vec{H}(\omega) \quad (2.18)$$

Here, $\varepsilon_r(\omega)$ and $\mu_r(\omega)$ are the frequency dependent relative permittivity and permeability, ε_∞ and μ_∞ denote the limiting values of the relative permittivity and permeability at high frequencies, $\chi_e(\omega)$ and $\chi_m(\omega)$ are the frequency dependent electric and magnetic susceptibility functions, respectively. In the following an overview of Lorentz, Drude and Debye type dispersion models are given. Details of their physical foundation can be found in (Ramakrishna & Grzegorzczuk, 2001).

Lorentz Model:

The basic single pole Lorentz model is defined with the following relations:

$$\chi_{e,L}(\omega) = \frac{\omega_{pe}^2}{\omega_{oe}^2 - \omega^2 + j\Gamma_e \omega} \quad (2.19a)$$

$$\chi_{m,L}(\omega) = \frac{\omega_{pm}^2}{\omega_{om}^2 - \omega^2 + j\Gamma_m \omega} \quad (2.19b)$$

where ω_{pe} and ω_{pm} are the plasma frequencies, ω_{oe} and ω_{om} are the resonance frequencies, and Γ_e and Γ_m are the damping coefficients, respectively. Inserting Equation (2.19a) into Equation (2.18), frequency and time domain relation between the polarization field and electric field is obtained as,

$$P(\omega) = \varepsilon_0 \frac{\omega_{pe}^2}{\omega_{oe}^2 - \omega^2 + j\Gamma_e \omega} E(\omega) \quad (2.20a)$$

$$\frac{d^2}{dt^2} P + \Gamma_e \frac{d}{dt} P + \omega_{oe}^2 P = \varepsilon_0 \omega_{pe}^2 E \quad (2.20b)$$

The first, second and third terms on the left of Equation (2.20b) account for the acceleration of the charges, the damping mechanisms of the system with the damping coefficient Γ_e , and the restoring forces with the resonance frequency ω_{oe} . In this model, permittivity and permeability have negative real parts (hence, the material exhibits negative refraction property) if the operating frequency is between $\left[\omega_{oe,om}, \sqrt{\omega_{oe,om}^2 + \omega_{pe,pm}^2} \right]$.

Drude Model:

Lorentz model yields the Drude model given below:

$$\chi_{e,Dr}(\omega) = \frac{\omega_{pe}^2}{j\Gamma_e\omega - \omega^2} \quad (2.21a)$$

$$\chi_{m,Dr}(\omega) = \frac{\omega_{pm}^2}{j\Gamma_m\omega - \omega^2} \quad (2.21b)$$

when the restoring force is negligible, and yields negative values for frequencies below the plasma frequency $(\omega_{pe,pm})$.

Debye Model:

Finally, one obtains the Debye model when the acceleration term is very small compared to the others:

$$\chi_{e,D}(\omega) = \frac{\omega_{pe}^2}{\omega_{oe}^2 + j\Gamma_e\omega} \quad (2.22a)$$

$$\chi_{m,D}(\omega) = \frac{\omega_{pm}^2}{\omega_{om}^2 + j\Gamma_m\omega} \quad (2.22b)$$

2.5 Phase velocity and group velocity

The general description of phase velocity (v_p) and group velocity (v_g) in a medium are given as:

$$v_p = \frac{\omega}{k} \quad \text{and} \quad v_g = \frac{d\omega}{dk} \quad (2.23)$$

Using the expression of k given in Equation (2.3), phase and group velocities can also be defined as

$$v_p = \frac{\omega}{k} = \frac{c}{n} \quad \text{and} \quad \frac{1}{v_g} = \frac{dk}{d\omega} = \frac{n}{c} + \frac{\omega}{c} \frac{dn}{d\omega} = \frac{1}{v_p} + \frac{\omega}{c} \frac{dn}{d\omega} \quad (2.24)$$

Hence, in a medium wherein the refractive index is frequency independent, phase and group velocities are equal to each other ($v_p = v_g$) with same sign. However, in a frequency dispersive medium with negative refractive index, phase velocity is always negative and group velocity can be greater or smaller than the phase velocity depending to the dispersion relation ($dn/d\omega$). For identical electric and magnetic parameters using lossless Lorentz model given in Equation (2.19), refractive index is expressed as $n(\omega) = \sqrt{\epsilon_r(\omega)\mu_r(\omega)} = \epsilon_r(\omega)$. Then, the group and phase velocities yield

$$v_p = \frac{c}{\epsilon_r(\omega)} ; \quad \frac{1}{v_g} = \frac{\epsilon_r(\omega)}{c} + \frac{\omega}{c} \frac{d\epsilon_r(\omega)}{d\omega} \quad (2.25)$$

with

$$\epsilon_r(\omega) = 1 + \frac{\omega_p^2}{\omega_o^2 - \omega^2} \quad \text{and} \quad \frac{d\epsilon_r(\omega)}{d\omega} = \frac{2\omega\omega_p^2}{(\omega_o^2 - \omega^2)^2} \quad (2.26)$$

Using the parameters that exhibit refractive index about -1 at $\omega = \omega_s$, phase and group velocities are tabulated in Table 2.2.

Table 2.2 Different Lorentz parameters which yield NIM about $n=-1$ at $\omega = \omega_s$

	ω_p/ω_s	ω_o/ω_s	v_g/c	v_g	v_p
Parameter1	1	$2^{-1/2}$	0.142	$v_g = c/7$	$v_p = \frac{c}{\epsilon_r(\omega)} \Big _{\omega=\omega_s} = -c$
Parameter2	$(3/2)^{1/2}$	2^{-1}	0.230	$v_g = 3c/13$	
Parameter3	$4/3$	3^{-1}	0.285	$v_g = 2c/7$	
Parameter4	$(48/25)^{1/2}$	5^{-1}	0.315	$v_g = 6c/19$	

For the parameters given in Table 2.2, variation in refractive index versus frequency and corresponding phase/group velocities are displayed in Figure 2.5, respectively. These figures show that, for a DNG material where $n(\omega) < 0$, v_p is opposite to v_g .

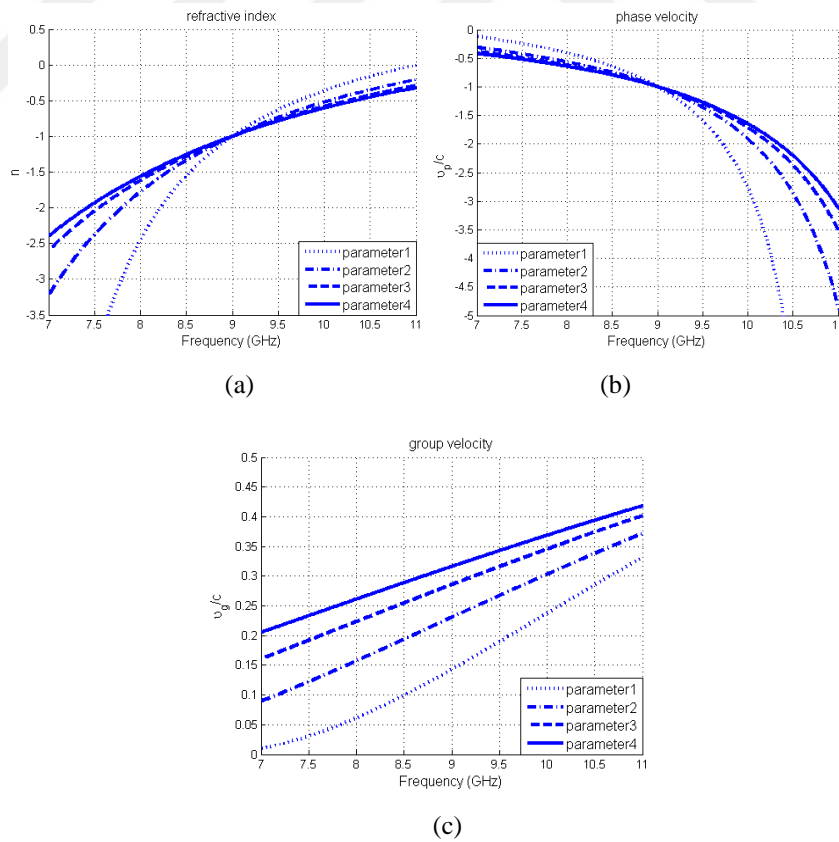


Figure 2.5 a) Refractive index, b) Phase velocity and c) Group velocity versus frequency for the parameters given in Table 2.2.

3. WAVE PROPAGATION IN DNG ENVIRONMENTS USING FINITE DIFFERENCE TIME DOMAIN (FDTD) ALGORITHM

3.1 Introduction

Finite difference time domain (FDTD) formulation is a convenient tool for solution of electromagnetic (EM) wave problems. The basic algorithm of Finite Difference Time Domain (FDTD) was first proposed by K. S. Yee in 1966 (Yee, 1966). Yee's FDTD algorithm deals with both electric and magnetic fields in time and space using the Maxwell's curl equations, which are replaced by a set of finite-difference equations. Since then, FDTD has been applied to a broad range of electromagnetic (EM) problems.

In the following, FDTD algorithm based on a central difference approximation of the spatial and time derivations of Maxwell's curl equations and wave equation for three-dimensional (3D) case are reviewed in source-free and non-dispersive media (Inan & Marshall, 2011).

$$\nabla \times \vec{E} = -\frac{\partial \vec{B}}{\partial t} - \sigma_m \vec{H} \quad (3.1a)$$

$$\nabla \cdot \vec{D} = 0 \quad (3.1b)$$

$$\nabla \times \vec{H} = \frac{\partial \vec{D}}{\partial t} + \sigma_e \vec{E} \quad (3.1c)$$

$$\nabla \cdot \vec{B} = 0 \quad (3.1d)$$

where $\sigma_{e,m}$ is the electric and magnetic conductivity. In a source-free, isotropic and lossless medium, Maxwell's curl equations in rectangular coordinates yield:

$$\nabla \times \vec{E} = -\mu \frac{\partial \vec{H}}{\partial t} \Rightarrow \begin{cases} \frac{\partial E_z}{\partial y} - \frac{\partial E_y}{\partial z} = -\mu \frac{\partial H_x}{\partial t} \\ \frac{\partial E_x}{\partial z} - \frac{\partial E_z}{\partial x} = -\mu \frac{\partial H_y}{\partial t} \\ \frac{\partial E_y}{\partial x} - \frac{\partial E_x}{\partial y} = -\mu \frac{\partial H_z}{\partial t} \end{cases} \quad (3.2)$$

$$\nabla \times \vec{H} = \varepsilon \frac{\partial \vec{E}}{\partial t} \Rightarrow \begin{cases} \frac{\partial H_z}{\partial y} - \frac{\partial H_y}{\partial z} = \varepsilon \frac{\partial E_x}{\partial t} \\ \frac{\partial H_x}{\partial z} - \frac{\partial H_z}{\partial x} = \varepsilon \frac{\partial E_y}{\partial t} \\ \frac{\partial H_y}{\partial x} - \frac{\partial H_x}{\partial y} = \varepsilon \frac{\partial E_z}{\partial t} \end{cases} \quad (3.3)$$

The system of six coupled partial differential equations of Equation (3.2) and Equation (3.3) forms the basis of the FDTD numerical algorithm for electromagnetic wave interactions with general three-dimensional (3D) objects. Placement of electric and magnetic field components in a Yee cell are described in (Inan & Marshall, 2011) and given in Figure 3.1.

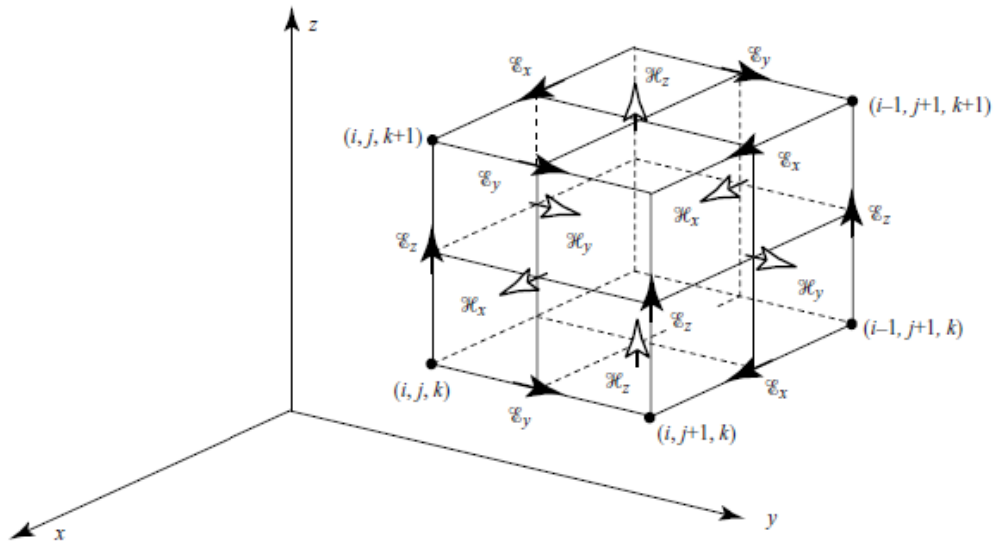


Figure 3.1 Positions of the field components in a unit cell of the Yee's lattice

With the Yee cell so defined, the spatial derivatives of various quantities and the derivatives in time are evaluated using the simple two-point centered difference approximations; a staggered spatial mesh is used for interleaved placement of the electric and magnetic fields and leapfrog integration in time is used to update the fields. The stability of FDTD algorithm is determined by Courant-Friedrich-Levy (CFL) stability condition which depends on the mesh size of spatial discretization (Δx , Δy , Δz) and the time step of the integration (Δt). In three dimensions, the Courant factor, defined as $S = c\Delta t/\Delta r$ where $\Delta r = 1/\sqrt{(1/\Delta x)^2 + (1/\Delta y)^2 + (1/\Delta z)^2}$ and c is the velocity of light, must be smaller than one to guarantee the stability of the algorithm. Therefore, a fine spatial mesh size Δr requires a fine time step Δt to maintain the desired accuracy. Hence the explicit finite difference approximations of Maxwell's equations are:

$$\begin{aligned}
H_x^{n+1/2}(i, j+1/2, k+1/2) &= H_x^{n-1/2}(i, j+1/2, k+1/2) \\
&\quad - \frac{\Delta t}{\mu\Delta y} [E_z^n(i, j+1, k+1/2) - E_z^n(i, j, k+1/2)] \\
&\quad + \frac{\Delta t}{\mu\Delta z} [E_y^n(i, j+1/2, k+1) - E_y^n(i, j+1/2, k)]
\end{aligned} \tag{3.4a}$$

$$\begin{aligned}
H_y^{n+1/2}(i+1/2, j, k+1/2) &= H_y^{n-1/2}(i+1/2, j, k+1/2) \\
&\quad + \frac{\Delta t}{\mu\Delta x} [E_z^n(i+1, j, k+1/2) - E_z^n(i, j, k+1/2)] \\
&\quad - \frac{\Delta t}{\mu\Delta z} [E_x^n(i+1/2, j, k+1) - E_x^n(i+1/2, j, k)]
\end{aligned} \tag{3.4b}$$

$$\begin{aligned}
H_z^{n+1/2}(i+1/2, j+1/2, k) &= H_z^{n-1/2}(i+1/2, j+1/2, k) \\
&\quad + \frac{\Delta t}{\mu\Delta y} [E_x^n(i+1/2, j+1, k) - E_x^n(i+1/2, j, k)] \\
&\quad - \frac{\Delta t}{\mu\Delta x} [E_y^n(i+1, j+1/2, k) - E_y^n(i, j+1/2, k)]
\end{aligned} \tag{3.4c}$$

$$\begin{aligned}
E_x^{n+1}(i+1/2, j, k) &= E_x^n(i+1/2, j, k) \\
&\quad + \frac{\Delta t}{\epsilon\Delta y} [H_z^{n+1/2}(i+1/2, j+1/2, k) - H_z^{n+1/2}(i+1/2, j-1/2, k)] \\
&\quad - \frac{\Delta t}{\epsilon\Delta z} [H_y^{n+1/2}(i+1/2, j, k+1/2) - H_y^{n+1/2}(i+1/2, j, k-1/2)]
\end{aligned} \tag{3.5a}$$

$$\begin{aligned}
E_y^{n+1}(i, j+1/2, k) &= E_y^n(i, j+1/2, k) \\
&\quad - \frac{\Delta t}{\varepsilon \Delta x} \left[H_z^{n+1/2}(i+1/2, j+1/2, k) - H_z^{n+1/2}(i-1/2, j+1/2, k) \right] \\
&\quad + \frac{\Delta t}{\varepsilon \Delta z} \left[H_x^{n+1/2}(i, j+1/2, k-1/2) - H_x^{n+1/2}(i, j+1/2, k+1/2) \right]
\end{aligned} \tag{3.5b}$$

$$\begin{aligned}
E_z^{n+1}(i, j, k+1/2) &= E_z^n(i, j, k+1/2) \\
&\quad + \frac{\Delta t}{\varepsilon \Delta x} \left[H_y^{n+1/2}(i+1/2, j, k+1/2) - H_y^{n+1/2}(i-1/2, j, k+1/2) \right] \\
&\quad - \frac{\Delta t}{\varepsilon \Delta y} \left[H_x^{n+1/2}(i, j+1/2, k+1/2) - H_x^{n+1/2}(i, j-1/2, k+1/2) \right]
\end{aligned} \tag{3.5c}$$

Taking the curl of the first Equation (3.2), and inserting the Equation (3.3), the coupled Maxwell's curl equations are combined to obtain the wave equations in the form of:

$$\nabla^2 u - \frac{1}{c^2} \frac{\partial^2 u}{\partial t^2} = \frac{\partial^2 u}{\partial x^2} + \frac{\partial^2 u}{\partial y^2} + \frac{\partial^2 u}{\partial z^2} - \frac{1}{c^2} \frac{\partial^2 u}{\partial t^2} = 0 \tag{3.6}$$

where u is any scalar field component (E_x , E_y , E_z , H_x , H_y , and H_z). Using the central finite difference approximation for the spatial and time derivatives in Equation (3.6), FDTD update equation for E-field is obtained as in the following:

$$\begin{aligned}
E^{n+1}(i, j, k) &= 2E^n(i, j, k) - E^{n-1}(i, j, k) \\
&\quad + (c\Delta t)^2 \left[\frac{E^n(i+1, j, k) - 2E^n(i, j, k) + E^n(i-1, j, k)}{\Delta x^2} \right. \\
&\quad \quad + \frac{E^n(i, j+1, k) - 2E^n(i, j, k) + E^n(i, j-1, k)}{\Delta y^2} \\
&\quad \quad \left. + \frac{E^n(i, j, k+1) - 2E^n(i, j, k) + E^n(i, j, k-1)}{\Delta z^2} \right]
\end{aligned} \tag{3.7}$$

3.2 Dispersive Finite Difference Time Domain (FDTD) Algorithms

The FDTD algorithm is simple to implement for isotropic and non-dispersive media but requires significant modification for the inclusion of dispersive media whose permittivity and/or permeability are functions of the frequency. The existing frequency

dispersive FDTD algorithms are known as Recursive Convolution (RC) method, Auxiliary Differential Equation (ADE) method and Z-transform method (Luebbers et al. 1990; Luebbers, Hunsberger, & Kunz, 1991; Luebbers & Hunsberger, 1992; Kelley & Luebbers, 1996; Kashiwa & Fukai, 1990; Sullivan, 1992; 1995). The detailed information on dispersive FDTD algorithm can be found in our review paper (Pekmezci & Sevgi, 2014) and also in (Bilotti & Sevgi, 2012).

The first frequency dependent FDTD formulation was published by Luebbers in 1990 (Luebbers et al., 1990) named as Recursive Convolution (RC). This technique utilized a recursive convolution scheme to model Debye media which relates the electric flux density (D) to the electric field through a convolution integral and discretizes the integral as a running sum. Then, Luebbers et. al. improved this technique using piecewise linear integration to obtain better accuracy in 1996 which is called as Piecewise Linear Recursive Convolution (PLRC) (Kelley & Luebbers, 1996). In 1990, Kashiwa presented a more general approach to the problem of dispersive media in FDTD by introducing the auxiliary differential equation (ADE) method (Kashiwa & Fukai, 1990). In this method, the frequency-domain constitutive relation between the electric flux density and electric field is expressed in time domain utilizing inverse Fourier transformation. This technique is very straightforward to implement but requires an additional storage variable for the flux density. In 1992, an alternative to the RC and ADE methods was proposed by Sullivan (Sullivan, 1992) based on the z-transform (ZT) where the relationship between the electric flux density (D) and the electric field intensity (E) has been formulated using z-transform.

In the following, dispersive FDTD algorithms (ADE and PLRC) are reviewed for 1D Maxwell's curl equations where there is no variation in two dimensions, namely, both y and z ($\partial/\partial y \equiv 0$ and $\partial/\partial z \equiv 0$). The process of simulations using dispersive FDTD approaches are also presented for a scenario wherein a Lorentz model DNG medium inserted in free space. The algorithm developed by ADE approach for 1D case can easily be expanded into 2D case (see Appendix A), and formulations based on Lorentz model are reduced to Drude model's formulation by setting resonance frequency (ω_0) as zero. Hence the following update equations developed for Lorentz type DNG media are also acceptable for Drude model simulations.

3.2.1 Piecewise Linear Recursive Convolution (PLRC)

Multiplication in the frequency domain corresponds to the convolution integral in the time domain which can be discretized as a running sum. Then, the time form of the constitutive equation $D(\omega) = \varepsilon(\omega)E(\omega)$ yields

$$D(t) = \varepsilon(t) * E(t) = \varepsilon_o \varepsilon_\infty E(t) + \varepsilon_o [\chi_e(t) * E(t)] \quad (3.8)$$

where $\chi_e(t)$ is the inverse Fourier transform of $\chi_e(\omega)$. Since the fields should be zero prior to $t=0$ (causality), Equation (3.8) can be discretized as

$$D^n = \varepsilon_o \varepsilon_\infty E^n + \varepsilon_o \int_0^{n\Delta t} E(n\Delta t - \tau) \chi_e(\tau) d\tau \quad (3.9)$$

where

$$E(n\Delta t - \tau) = E^{n-q} + \frac{E^{n-q-1} - E^{n-q}}{\Delta t} (\tau - q\Delta t) \quad \text{for } q\Delta t \leq \tau \leq (q+1)\Delta t \quad (3.10)$$

The RC-FDTD presented in (Luebbers et al., 1990; Luebbers, Hunsberger, & Kunz, A, 1991; Luebbers & Hunsberger, 1992) assumed that all field components are constant over each time interval Δt , while PLRC-FDTD (Kelley & Luebbers, 1996) uses a linear approximation in expressing fields over a given time interval $[q\Delta t, (q+1)\Delta t]$ which yields a better accuracy than the RC-FDTD approach. Thus, when the value of ξ_e^q parameter (in Equation 3.12b) is taken as zero, the PLRC formulation can easily reduce to constant RC formulation. In the following discrete form of D is produced by substituting Equation (3.10) into Equation (3.9).

$$D^n = \varepsilon_o \varepsilon_\infty E^n + \varepsilon_o \sum_{q=0}^{n-1} \left[E^{n-q} \chi_e^q + (E^{n-q-1} - E^{n-q}) \xi_e^q \right] \quad (3.11)$$

where

$$\chi_e^q = \int_{q\Delta t}^{(q+1)\Delta t} \chi_e(\tau) d\tau \quad (3.12a)$$

$$\xi_e^q = \frac{1}{\Delta t} \int_{q\Delta t}^{(q+1)\Delta t} (\tau - q\Delta t) \chi_e(\tau) d\tau \quad (3.12b)$$

Since the discrete form of Ampere's law given in Equation (3.1) can be written as in the following, the value of D at the next time step is needed:

$$\frac{D^{n+1} - D^n}{\Delta t} = [\nabla \times H^n] \quad (3.13)$$

$$D^{n+1} = E^{n+1} [\varepsilon_o \varepsilon_\infty + \varepsilon_o \chi_e^0 - \varepsilon_o \xi_e^0] + \varepsilon_o E^n \xi_e^0 + \varepsilon_o \sum_{q=0}^{n-1} [E^{n-q} \chi_e^{q+1} + (E^{n-q-1} - E^{n-q}) \xi_e^{q+1}] \quad (3.14)$$

Combining Equation (3.11) and Equation (3.14) one obtains:

$$\begin{aligned} D^{n+1} - D^n = & \varepsilon_o [\varepsilon_\infty + \chi_e^0 - \xi_e^0] E^{n+1} + \varepsilon_o [\xi_e^0 - \varepsilon_\infty] E^n \\ & - \varepsilon_o \sum_{q=0}^{n-1} [E^{n-q} \Delta \chi_e^q + (E^{n-q-1} - E^{n-q}) \Delta \xi_e^q] \end{aligned} \quad (3.15)$$

where

$$\Delta \chi_e^q = \chi_e^q - \chi_e^{q+1} \quad (3.16a)$$

$$\Delta \xi_e^q = \xi_e^q - \xi_e^{q+1} \quad (3.16b)$$

Substituting Equation (3.15) and Equation (3.16) into Equation (3.13) yields an update equation for the electric field in a DNG medium as follows:

$$E^{n+1} = \frac{1}{(\varepsilon_\infty + \chi_e^0 - \xi_e^0)} \left[(\varepsilon_\infty - \xi_e^0) E^n + \psi_e^n + \frac{\Delta t}{\varepsilon_o} (\nabla \times H^n) \right] \quad (3.17)$$

where ψ_e^n is known as the recursive accumulator and given by

$$\psi_e^n = \sum_{q=0}^{n-1} \left[E^{n-q} \Delta \chi_e^q + (E^{n-q-1} - E^{n-q}) \Delta \xi_e^q \right] \quad (3.18)$$

For the Lorentz model, electric susceptibility function in time domain $\chi_e(t)$ can be obtained via the inverse Fourier transform of Equation (2.19):

$$\chi_e(t) = \gamma_e e^{-\alpha_e t} \sin(\beta_e t) u(t) \quad (3.19)$$

where $\alpha_e = \Gamma_e / 2$, $\beta_e = \sqrt{\omega_{pe}^2 - \Gamma_e^2 / 4}$, and $\gamma_e = \omega_{pe}^2 / \beta_e$. However, the time domain electric susceptibility function in Equation (3.19) is not in an appropriate form in updating the corresponding RC. For this reason, complex time domain susceptibility is defined as:

$$\chi_{e,c}(t) = -j\gamma_e e^{(-\alpha_e + j\beta_e)t} u(t) \quad (3.20a)$$

with the related real quantities

$$\chi_e = \text{Re} \{ \chi_{e,c} \} \quad (3.20b)$$

Substitution of $\chi_{e,c}(t)$ into Equation (3.12) and Equation (3.18) yields the complex quantities

$$\chi_{e,c}^q = \frac{-j\gamma_e}{\alpha_e - j\beta_e} \left[1 - e^{(-\alpha_e + j\beta_e)\Delta t} \right] e^{(-\alpha_e + j\beta_e)q\Delta t} \quad (3.21a)$$

$$\xi_{e,c}^q = \frac{j\gamma_e}{\Delta t(\alpha_e - j\beta_e)^2} e^{(-\alpha_e + j\beta_e)q\Delta t} \left[e^{(-\alpha_e + j\beta_e)\Delta t} (1 + (\alpha_e - j\beta_e)\Delta t) - 1 \right] \quad (3.21b)$$

$$\Delta\chi_{e,c}^q = \chi_{e,c}^q \left[1 - e^{(-\alpha_e + j\beta_e)\Delta t} \right] \quad (3.21c)$$

$$\Delta\xi_{e,c}^q = \xi_{e,c}^q \left[1 - e^{(-\alpha_e + j\beta_e)\Delta t} \right] \quad (3.21d)$$

Finally, the complex recursive accumulator is obtained as:

$$\psi_{e,c}^n = \sum_{q=0}^{n-1} \left[E^{n-q} \Delta\chi_{e,c}^q + (E^{n-q-1} - E^{n-q}) \Delta\xi_{e,c}^q \right] \quad (3.22a)$$

$$\psi_{e,c}^{n+1} = E^{n+1} \left[\Delta\chi_{e,c}^0 - \Delta\xi_{e,c}^0 \right] + E^n \Delta\xi_{e,c}^0 + \psi_{e,c}^n e^{(-\alpha_e + j\beta_e)\Delta t} \quad (3.22b)$$

$$\psi_e^{n+1} = \text{Re} \{ \psi_{e,c}^{n+1} \} \quad (3.22c)$$

Note that, in the PLRC-FDTD algorithm, the complex recursive accumulator is updated using Equation (3.22b) and the real part in Equation (3.22c) is used in FDTD E-field update equations. The same also applies for the H-fields.

The steps for implementing PLRC-FDTD are listed below and the corresponding flow-chart is given in Figure 3.2.

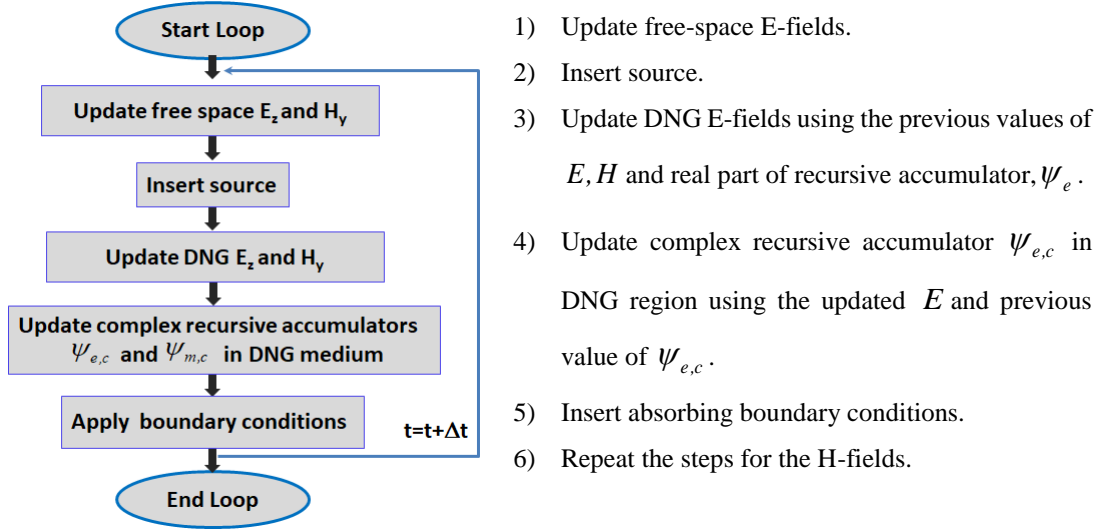


Figure 3.2 Flow chart of PLRC-FDTD procedure

3.2.2 Auxiliary Differential Equations (ADE)

ADE method converts the frequency domain equation of the Lorentz model into a time domain differential equation using $j\omega \leftrightarrow \partial/\partial t$ and $-\omega^2 \leftrightarrow \partial^2/\partial t^2$. This will yield

$$D_z(\omega) = \epsilon_o \epsilon_\infty E_z(\omega) + S_k(\omega) \quad (3.23a)$$

$$B_y(\omega) = \mu_o \mu_\infty H_y(\omega) + J_k(\omega) \quad (3.23b)$$

where

$$S_k(\omega) = \epsilon_o \frac{\omega_{pe}^2}{\omega_{oe}^2 - \omega^2 + j\Gamma_e \omega} E_z(\omega) \quad (3.24a)$$

$$J_k(\omega) = \mu_o \frac{\omega_{pm}^2}{\omega_{om}^2 - \omega^2 + j\Gamma_m \omega} H_y(\omega) \quad (3.24b)$$

The inverse Fourier transform of Equation (3.24) yields:

$$\frac{\partial^2 S_k(t)}{\partial t^2} + \Gamma_e \frac{\partial S_k(t)}{\partial t} + \omega_{oe}^2 S_k(t) = \varepsilon_o \omega_{pe}^2 E_z(t) \quad (3.25a)$$

$$\frac{\partial^2 J_k(t)}{\partial t^2} + \Gamma_m \frac{\partial J_k(t)}{\partial t} + \omega_{om}^2 J_k(t) = \mu_o \omega_{pm}^2 H_y(t) \quad (3.25b)$$

The discrete form of Equation (3.25) is given as:

$$S_k^{n+1}(i) = \left[\frac{2 - \Delta t^2 \omega_{oe}^2}{1 + 0.5 \Delta t \Gamma_e} \right] S_k^n(i) + \left[\frac{0.5 \Delta t \Gamma_e - 1}{0.5 \Delta t \Gamma_e + 1} \right] S_k^{n-1}(i) + \left[\frac{\Delta t^2 \varepsilon_o \omega_{pe}^2}{1 + 0.5 \Delta t \Gamma_e} \right] E_z^n(i) \quad (3.26a)$$

$$J_k^{n+1/2}(i+1/2) = \left[\frac{2 - \Delta t^2 \omega_{om}^2}{1 + 0.5 \Delta t \Gamma_m} \right] J_k^{n-1/2}(i+1/2) + \left[\frac{0.5 \Delta t \Gamma_m - 1}{0.5 \Delta t \Gamma_m + 1} \right] J_k^{n-3/2}(i+1/2) + \left[\frac{\Delta t^2 \mu_o \omega_{pm}^2}{1 + 0.5 \Delta t \Gamma_m} \right] H_y^{n-1/2}(i+1/2) \quad (3.26b)$$

These can then be used in iterative form and FDTD loops can be formed accordingly:

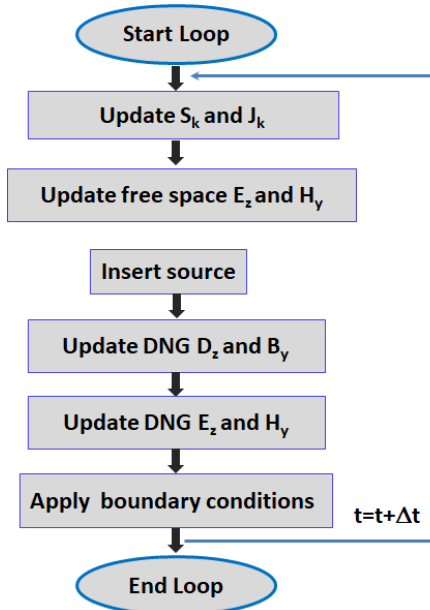
$$D_z^{n+1}(i) = D_z^n(i) + \frac{\Delta t}{\Delta x} \left[H_y^{n+1/2}(i+1/2) - H_y^{n+1/2}(i-1/2) \right] \quad (3.27a)$$

$$B_y^{n+1/2}(i+1/2) = B_y^{n-1/2}(i+1/2) + \frac{\Delta t}{\Delta x} \left[E_z^{n+1}(i+1) - E_z^{n+1}(i) \right] \quad (3.27b)$$

$$E_z^{n+1}(i) = \frac{D_z^{n+1}(i) - S_k^{n+1}(i)}{\varepsilon_o \varepsilon_\infty} \quad (3.27c)$$

$$H_y^{n+1/2}(i+1/2) = \frac{B_y^{n+1/2}(i+1/2) - J_k^{n+1}(i+1/2)}{\mu_o \mu_\infty} \quad (3.27d)$$

The steps for implementing ADE-FDTD are listed below and the corresponding flow-chart is given in Figure 3.3.



- 1) Update S_k using the previous values of E_z and S_k
- 2) Update E_z in free space and insert excitation source.
- 3) Update D_z in DNG medium using the previous values of D_z and H_y .
- 4) Update E_z in DNG medium using the present value of D_z and S_k .
- 5) Apply the absorbing boundary conditions at the terminating nodes.
- 6) Repeat the whole steps for the magnetic fields (J_k, B_y, H_y) .

Figure 3.3 Flow chart of ADE-FDTD procedure

3.3 Dispersive ADE-FDTD Algorithm for Wave Equation

Although the wave equation has the simplest form in non-dispersive media (Sadiku, 2001), it becomes significantly more complicated in dispersive media where the constitutive parameters are frequency dependent. In such cases, we may not be able to move ϵ and μ directly outside of the time derivatives. For instance, the multiplication of simultaneously frequency dependent ϵ and μ in wave equation corresponds to convolution in time domain which leads to extracting additional recursive accumulators to evaluate the discrete time convolution of ϵ and μ . Therefore, utilizing PLRC approach for wave equation in DNG media is more challenging than ADE approach where the constitutive parameters and fields (E or H) are expressed by auxiliary equations. For this reason, we develop ADE approach for DNG medium based on wave equation and present update equations for 2D case.

However, in SNG media (one of the constitutive parameters is constant), there exist only one recursive accumulator. Hence, PLRC approach can easily be employed in SNG media using wave equation. On the other way, ADE formulations for SNG media can simply be converted from DNG media's by choosing the magnetic and electric plasma frequencies as zero for ENG and MNG media, respectively. Both ADE and PLRC

formulations using wave equation in Lorentz type ENG media can be found in (Pekmezci, Topuz, & Sevgi, 2016). Hence, only numerical results validated with analytical solutions will be presented in the numerical results section.

In DNG media where both medium parameters depend on frequency and are simultaneously negative, the wave equation becomes:

$$\nabla^2 E(\omega) + k^2(\omega)E(\omega) = 0 \quad \text{with} \quad k^2(\omega) = \omega^2 \mu(\omega) \varepsilon(\omega) = \frac{\omega^2}{c^2} n^2(\omega) \quad (3.28)$$

where

$$\varepsilon(\omega) = \varepsilon_o [\varepsilon_\infty + \chi_e(\omega)] \quad ; \quad \mu(\omega) = \mu_o [\mu_\infty + \chi_m(\omega)] \quad (3.29)$$

Here, ε_∞ and μ_∞ are the relative permittivity and permeability at higher frequencies and $\chi_e(\omega)$, $\chi_m(\omega)$, are the electric and magnetic susceptibility functions of the dispersive medium which are defined for Lorentz model. Then, inserting Equation (3.29) into Equation (3.28) and modifying the equation we can obtain,

$$\nabla^2 E(\omega) + \frac{\omega^2}{c^2} D(\omega) = 0 \quad (3.30)$$

where

$$D(\omega) = \mu_\infty G(\omega) + Q(\omega) \quad (3.31a)$$

$$Q(\omega) = \chi_m(\omega) G(\omega) \quad (3.31b)$$

$$G(\omega) = \varepsilon_\infty E(\omega) + P(\omega) \quad (3.31c)$$

$$P(\omega) = \chi_e(\omega) E(\omega) \quad (3.31d)$$

In two-dimensional (2D) case under the assumptions $\partial/\partial z \equiv 0$, frequency dependent wave equation obtained in Equation (3.30) is converted into a time domain differential equation using ADE approach by inserting the following conversion $j\omega \leftrightarrow \partial/\partial t$ and $-\omega^2 \leftrightarrow \partial^2/\partial t^2$.

$$\frac{\partial^2 E}{\partial x^2} + \frac{\partial^2 E}{\partial y^2} - \frac{1}{c^2} \frac{\partial^2 D}{\partial t^2} = 0 \quad (3.32)$$

Taking the central difference approximations both for spatial and time derivatives, and provide the discrete form of wave equation in Equation (3.32).

$$D^{n+1}(i, j) = 2D^n(i, j) - D^{n-1}(i, j) + (c\Delta t)^2 \left[\frac{E^n(i+1, j) - 2E^n(i, j) + E^n(i-1, j)}{\Delta x^2} + \frac{E^n(i, j+1) - 2E^n(i, j) + E^n(i, j-1)}{\Delta y^2} \right] \quad (3.33)$$

Substitution of $\chi_e(\omega)$ and $\chi_m(\omega)$ functions into Equation (3.31) and taking inverse Fourier transforms yield the time domain equations and then the discrete form of time domain equations is obtained as:

$$D^{n+1}(i, j) = \mu_\infty G^{n+1}(i, j) + Q^{n+1}(i, j) \quad (3.34a)$$

$$Q^{n+1}(i, j) = g_1 Q^n(i, j) - g_2 Q^{n-1}(i, j) + g_3 G^n(i, j) \quad (3.34b)$$

$$G^{n+1}(i, j) = \varepsilon_\infty E^{n+1}(i, j) + P^{n+1}(i, j) \quad (3.34c)$$

$$P^{n+1}(i, j) = p_1 P^n(i, j) - p_2 P^{n-1}(i, j) + p_3 E^n(i, j) \quad (3.34d)$$

where $p_1 = \left[\frac{2 - \Delta t^2 \omega_{oe}^2}{1 + 0.5 \Delta t \Gamma_e} \right]$; $p_2 = \left[\frac{1 - 0.5 \Delta t \Gamma_e}{1 + 0.5 \Delta t \Gamma_e} \right]$; $p_3 = \left[\frac{\Delta t^2 \omega_{pe}^2}{1 + 0.5 \Delta t \Gamma_e} \right]$; $g_1 = \left[\frac{2 - \Delta t^2 \omega_{om}^2}{1 + 0.5 \Delta t \Gamma_m} \right]$; $g_2 = \left[\frac{1 - 0.5 \Delta t \Gamma_m}{1 + 0.5 \Delta t \Gamma_m} \right]$; $g_3 = \left[\frac{\Delta t^2 \omega_{pm}^2}{1 + 0.5 \Delta t \Gamma_m} \right]$.

Making some mathematical manipulations and rearranging Equation (3.33) using equations given in Equation (3.34) yield the FDTD update equation based on 2D wave equation in DNG medium:

$$\begin{aligned}
E^{n+1}(i, j) = & e_1 E^n(i, j) - E^{n-1}(i, j) + e_2 [E^n(i+1, j) - 2E^n(i, j) + E^n(i-1, j)] \\
& + e_{22} [E^n(i, j+1) - 2E^n(i, j) + E^n(i, j-1)] \\
& - [e_3 P^n(i, j) + e_4 P^{n-1}(i, j) + e_5 Q^n(i, j) + e_6 Q^{n-1}(i, j)]
\end{aligned} \quad (3.35)$$

where $e_1 = 2 - \frac{(p_3 \mu_x - g_3 \epsilon_x)}{\epsilon_x \mu_x}$; $e_2 = \frac{c^2 \Delta t^2}{\epsilon_x \mu_x \Delta x^2}$; $e_3 = \frac{(p_1 - 2) \mu_x + g_3}{\epsilon_x \mu_x}$; $e_4 = \frac{1 - p_2}{\epsilon_x}$; $e_5 = \frac{g_1 - 2}{\epsilon_x \mu_x}$; $e_6 = \frac{1 - g_2}{\epsilon_x \mu_x}$; $e_{22} = \frac{c^2 \Delta t^2}{\epsilon_x \mu_x \Delta y^2}$.

It should be noted that although wave equation based FDTD can be used in homogeneously DNG filled regions, it has severe stability problems when applied to environments involving DNG-DPS mixed media as noted in (Aoyagi, Lee, & Mittra, 1993).

3.4 Termination of DNG Media with Mur's ABC

Simulating wave propagation from scattering, antennas, or waveguides requires an unbounded domain or a domain large enough so that waves do not reflect off the domain boundaries back into the computational domain and interfere with the wave propagation being analyzed. The computational requirements for making a domain large enough to prevent these reflections would be nearly computationally impossible, or at least highly undesirable, in most cases. Therefore, to simulate the infinite space, absorbing boundary conditions (ABCs) are needed. The development of efficient and accurate ABCs is very important for the FDTD method and several types of ABC have been proposed which are grouped into two major approaches, analytical and perfect matched layer (Taflove & Hagness, 2005).

The most popular absorbing boundary condition in analytical group was derived by Enguidaj-Majda (Engquist & Majda, 1977) and the optimal FDTD implementation was given by Mur in 1981 (Mur, 1981). In contrast to this, Berenger introduced another

popular absorbing boundary condition named as perfectly matched layer (PML) in 1994 (Berenger, 1996). It is designed by setting the outer boundary of the model space to an absorbing material layer, which absorb most of the impinging waves and have low reflection. The innovation of Berenger's PML is that its quality does not depend on incidence angle, polarization or frequency and can be used as an absorbing boundary to terminate domains comprised of inhomogeneous, dispersive, anisotropic, and even nonlinear media, which was previously not possible with analytically derived ABCs. For this reason, PML provide significantly better accuracy than most other analytical ABC's (Liao, Wong, Yang, & Yuan, 1984; Higdon, 1986; Gedney & Zhao, 2010). Soon after, Chew and Weedon (Chew & Weedon, 1994) obtained a perfectly matched layer by introducing complex coordinate stretching into Maxwell's equations. This work led to the development of PML schemes that did not require the splitting of fields. Researchers presenting these types of formulations include Veihl and Mittra (Veihl & Mittra, 1996), Gedney (Gedney, 1996a), Zhao and Cangellaris (Zhao & Cangellaris, 1996) and Sullivan (Sullivan, 1997). An alternative approach for avoiding the field splitting was originally suggested by Sacks et al. (Sacks, Kingsland, Lee, & Lee, 1995), who used anisotropic material having both magnetic and electric permittivity tensors to describe the absorbing layer and applied this technique to the frequency domain based finite element methods. Based on Sacks's work, Gedney firstly introduced the Uniaxial PML (UPML) into the FDTD method and demonstrated the effectiveness of this approach for both free space (Gedney, 1996a) and dispersive medium (Gedney, 1996b).

Nonetheless implementation of either Mur or PML to DNG media for terminating the FDTD computational domain without any modification results in instability. In literature one can find several works on truncation of DNG media using PML Boundary Conditions in DNG media (Gedney, 1996b; Roden & Gedney, 2000; Fan & Liu, 2000; (Cummer, 2003; 2004; Zheng, Tam, Ge, & Xu, 2009; Li & Dai, 2006; Lu L. , 2006). Review of formulation and implementation of modified UPML is also presented in Appendix B. One of the disadvantages of those formulations is that they require both electric and magnetic fields which increases the computational time and memory requirements. For this reason, Kosmas et al. presented an ABC based on Mur's approach using dispersive media with a single pole conductivity z-transform model in 2004 (Kosmas & Rappaport, 2004). As distinct from Kosmas's work, we have developed a modified formulation of Mur's ABC for terminating the DNG media which are obtained

from frequency dependent one-way wave equations using PLRC method presented in (Pekmezci, Topuz, & Sevgi, 2018). In the following we briefly outline the formulations of first and second order DNG-Mur ABC using PLRC-FDTD algorithm based on (Pekmezci, Topuz, & Sevgi, 2018) and list the parameters used in the update equations both for Drude and Lorentz models in Table 3.1 and Table 3.2.

In a linear, isotropic, and homogenous DNG media where both medium parameters depend on frequency and are simultaneously negative, the wave equation presented in Equation (3.28) can be rewritten in Cartesian coordinates for three-dimensional case as in the following form:

$$\left(\frac{\partial^2}{\partial x^2} + \frac{\partial^2}{\partial y^2} + \frac{\partial^2}{\partial z^2} + \frac{\omega^2}{c^2} n^2(\omega) \right) E(\omega) = 0 \quad (3.36)$$

Defining the differential operators as $D_x \equiv \partial/\partial x, D_y \equiv \partial/\partial y, D_z \equiv \partial/\partial z, D_\omega \equiv j\omega/c$ and $D_\omega^2 \equiv -\omega^2/c^2$ to express the first and second derivatives of space and frequency and inserting into the Equation (3.36) yields

$$\left(D_x^2 + D_y^2 + D_z^2 - D_\omega^2 n^2(\omega) \right) E(\omega) = LE(\omega) = 0 \quad \text{with } L \equiv D_x^2 + D_y^2 + D_z^2 - D_\omega^2 n^2(\omega) \quad (3.37)$$

Here, L is the wave operator including partial differential equations and frequency terms that can be factored as in the following:

$$LE(\omega) \equiv L^+ L^- E(\omega) = 0 \quad (3.38)$$

where L^+ and L^- define the right and left going waves, respectively and can be written for x, y and z directions as in (Taflove, Oskooi, & Johnson, 2013).

$$(at \ x=0) \ L_x^- \equiv D_x - D_\omega n(\omega) \sqrt{1-S_x^2} \quad ; \quad (at \ x=h) \ L_x^+ \equiv D_x + D_\omega n(\omega) \sqrt{1-S_x^2} \quad (3.39a)$$

$$(at \ y=0) \ L_y^- \equiv D_y - D_\omega n(\omega) \sqrt{1-S_y^2} \quad ; \quad (at \ y=h) \ L_y^+ \equiv D_y + D_\omega n(\omega) \sqrt{1-S_y^2} \quad (3.39b)$$

$$(at \ z=0) \ L_z^- \equiv D_z - D_\omega n(\omega) \sqrt{1-S_z^2} \quad ; \quad (at \ z=h) \ L_z^+ \equiv D_z + D_\omega n(\omega) \sqrt{1-S_z^2} \quad (3.39c)$$

with

$$S_x^2 = \frac{(D_y^2 + D_z^2)}{D_\omega^2 n^2(\omega)} \quad ; \quad S_y^2 = \frac{(D_x^2 + D_z^2)}{D_\omega^2 n^2(\omega)} \quad ; \quad S_z^2 = \frac{(D_x^2 + D_y^2)}{D_\omega^2 n^2(\omega)} \quad (3.40)$$

Using the Taylor series expansion to approximate the square roots in Equation (3.39), one can define the order of DNG-Mur's absorbing boundary condition as 1st and 2nd order (Engquist & Majda, 1977). The simplest approximation known as 1st order Mur-type ABC is obtained by keeping only the unity term in $\sqrt{1-S^2}$, whereas the second order uses $\sqrt{1-S^2} \cong 1-S^2/2$. In the following section, modified formulations of both approximations for using in truncation of DNG media are presented.

3.4.1 First-order DNG-Mur's ABCs

Considering 1D case and wave propagation along x-direction where $\partial/\partial y \equiv 0$ and $\partial/\partial z \equiv 0$, right and left going waves in Equation (3.37) can be defined as:

$$(D_x^2 - D_\omega^2 n^2(\omega))E(\omega) = L_x^+ L_x^- E(\omega) = (D_x + D_\omega n(\omega))(D_x - D_\omega n(\omega))E(\omega) = 0 \quad (3.41)$$

For left and right going waves, Equation (3.41) must satisfy the backward/forward wave condition and substituting $D_x \equiv \frac{\partial}{\partial x}$ and $D_\omega \equiv \frac{j\omega}{c}$ into Equation (3.41) yields:

$$\left(\frac{\partial}{\partial x} + \frac{j\omega}{c}n(\omega)\right)\left(\frac{\partial}{\partial x} - \frac{j\omega}{c}n(\omega)\right)E(\omega) = 0 \quad (3.42)$$

Here, $n(\omega)$ is the frequency dependent refractive index and expressed as $n(\omega) = \sqrt{\varepsilon_r(\omega)\mu_r(\omega)} = \sqrt{[1+\chi_e(\omega)][1+\chi_m(\omega)]}$. The functional form of $n(\omega)$ complicates inverse Fourier transform of the operators in Equation (3.42). A convenient way of avoiding this complication is to approximate geometric mean in $n(\omega)$ by its arithmetic mean. This approach is found to be rather effective when source spectrum is centered close to the intersection point of the $\chi_e(\omega)$ and $\chi_m(\omega)$. However, for purposes of brevity, we present the formulations for the case of identical models for $\varepsilon_r(\omega)$ and $\mu_r(\omega)$ to write the refractive index as $n(\omega) = 1 + \chi_e(\omega)$. Then the left going waves in Equation (3.42) yields:

$$\frac{\partial E(\omega)}{\partial x} - \frac{j\omega}{c}E(\omega) - \frac{j\omega}{c}P(\omega) = 0 \quad \text{with} \quad P(\omega) = \chi_e(\omega)E(\omega) \quad (3.43)$$

The inverse Fourier transform of Equation (3.42) yields

$$\frac{\partial E(t)}{\partial x} - \frac{1}{c}\frac{\partial E(t)}{\partial t} - \frac{1}{c}\frac{\partial P(t)}{\partial t} = 0 \quad \text{with} \quad P(t) = \chi_e(t) * E(t) \quad (3.44)$$

where ‘*’ denotes the convolution. To drive FDTD algorithm for Equation (3.44), two point centered difference discretization is used at mesh point $i+1/2$ and at time index $n+1/2$:

$$E^{n+1}(i) = E^n(i+1) + \left(\frac{c\Delta t - \Delta x}{c\Delta t + \Delta x}\right) [E^{n+1}(i+1) - E^n(i)] - \left(\frac{\Delta x}{c\Delta t + \Delta x}\right) [P^{n+1}(i+1) - P^n(i+1) + P^{n+1}(i) - P^n(i)] \quad (3.45)$$

Here, i and n are the indices of discrete space and time variables, Δx and Δt are spatial and temporal discretization step sizes, respectively. The discrete form of P^n is obtained by using PLRC method following the steps presented in Section 3.2.1. Then P terms in the right side of Equation (3.45) can then be expressed as:

$$\begin{aligned} P^{n+1}(i+1) - P^n(i+1) + P^{n+1}(i) - P^n(i) &= (\chi_e^0 - \xi_e^0) E^{n+1}(i+1) + (\chi_e^0 - \xi_e^0) E^{n+1}(i) \\ &\quad + \xi_e^0 E^n(i+1) + \xi_e^0 E^n(i) \\ &\quad - \psi_e^n(i+1) - \psi_e^n(i) \end{aligned} \quad (3.46)$$

where ψ_e^n is known as the recursive accumulator and given by

$$\psi_e^n(i) = \sum_{q=0}^{n-1} \left[(\Delta \chi_e^q - \Delta \xi_e^q) E^{n-q}(i) + \Delta \xi_e^q E^{n-q-1}(i) \right] \quad \text{with} \quad \begin{aligned} \Delta \chi_e^q &= \chi_e^q - \chi_e^{q+1} \\ \Delta \xi_e^q &= \xi_e^q - \xi_e^{q+1} \end{aligned} \quad (3.47)$$

Substituting Equation (3.46) into Equation (3.45) and rearranging the discrete equation, FDTD update equations for left (at $i=1$) and right (at $i=K_x$) boundaries yield as:

$$E^{n+1}(1) = a_1 E^{n+1}(2) + a_2 E^n(2) - a_3 E^n(1) + a_4 [\psi_e^n(2) + \psi_e^n(1)] \quad (3.48a)$$

$$E^{n+1}(K_x) = a_1 E^{n+1}(K_x - 1) + a_2 E^n(K_x - 1) - a_3 E^n(K_x) + a_4 [\psi_e^n(K_x - 1) + \psi_e^n(K_x)] \quad (3.48b)$$

with

$$a_1 = \left(\frac{c_1 - c_2 c_3}{1 + c_2 c_3} \right); a_2 = \left(\frac{1 - c_2 c_4}{1 + c_2 c_3} \right); a_3 = \left(\frac{c_1 + c_2 c_4}{1 + c_2 c_3} \right); a_4 = \left(\frac{c_2}{1 + c_2 c_3} \right); c_1 = \left(\frac{c \Delta t - \Delta x}{c \Delta t + \Delta x} \right); c_2 = \left(\frac{\Delta x}{c \Delta t + \Delta x} \right); c_3 = (\chi_e^0 - \xi_e^0); c_4 = \xi_e^0 \cdot$$

The proposed formulation given in Equation (3.48) can be used easily for Drude and Lorentz model by modifying the parameters χ_e^q , ξ_e^q , $\Delta \chi_e^q$, $\Delta \xi_e^q$ and ψ_e^{n+1} as indicated in Table 3.1.

Table 3.1 Parameters for Drude and Lorentz Model in 1st order DNG-Mur ABC

Drude Model
$\chi_e(\omega) = \frac{\omega_{pe}^2}{-\omega^2 + j\Gamma_e\omega}$
$\chi_e(t) = \frac{\omega_{pe}^2}{\Gamma_e}(1 - e^{-\Gamma_e t})u(t)$
$\chi_e^q = \frac{\omega_{pe}^2}{\Gamma_e} \left[\Delta t + \frac{1}{\Gamma_e} e^{-q\Gamma_e\Delta t} (e^{-\Gamma_e\Delta t} - 1) \right]$
$\xi_e^q = \frac{\omega_{pe}^2}{\Gamma_e\Delta t} \left[\frac{\Delta t^2}{2} + \frac{e^{-q\Gamma_e\Delta t}}{\Gamma_e} \left(\Delta t e^{-\Gamma_e\Delta t} + \frac{e^{-\Gamma_e\Delta t}}{\Gamma_e} - \frac{1}{\Gamma_e} \right) \right]$
$\Delta\chi_e^q = \chi_e^q - \chi_e^{q+1} = -\frac{\omega_{pe}^2}{(\Gamma_e)^2} e^{-q\Gamma_e\Delta t} (e^{-\Gamma_e\Delta t} - 1)^2$
$\Delta\xi_e^q = \xi_e^q - \xi_e^{q+1} = -\frac{\omega_{pe}^2}{(\Gamma_e)^2 \Delta t} (e^{-\Gamma_e\Delta t} - 1) \left(\Delta t e^{-\Gamma_e\Delta t} + \frac{e^{-\Gamma_e\Delta t}}{\Gamma_e} - \frac{1}{\Gamma_e} \right) e^{-q\Gamma_e\Delta t}$
$\psi_e^{n+1} = [\Delta\chi_e^0 - \Delta\xi_e^0] E^{n+1} + \Delta\xi_e^0 E^n + e^{-\Gamma_e\Delta t} \psi_e^n$
Lorentz Model
$\chi_e(\omega) = \frac{\omega_{pe}^2}{\omega_{oe}^2 - \omega^2 + j\Gamma_e\omega}$
$\chi_{e,c}(t) = -j\gamma_e e^{(-\alpha_e + j\beta_e)t} u(t); \chi_e(t) = \text{Re}\{\chi_{e,c}(t)\} \text{ where } \alpha_e = \Gamma_e / 2; \beta_e = \sqrt{\omega_{oe}^2 - \Gamma_e^2/4}; \gamma_e = \omega_{pe}^2 / \beta_e$
$\chi_{e,c}^q = \frac{-j\gamma_e}{\alpha_e - j\beta_e} \left[1 - e^{(-\alpha_e + j\beta_e)\Delta t} \right] e^{(-\alpha_e + j\beta_e)q\Delta t}; \chi_e^q = \text{Re}\{\chi_{e,c}^q\}$
$\xi_{e,c}^q = \frac{j\gamma_e}{\Delta t(\alpha_e - j\beta_e)^2} \left[e^{(-\alpha_e + j\beta_e)\Delta t} (1 + (\alpha_e - j\beta_e)\Delta t) - 1 \right] e^{(-\alpha_e + j\beta_e)q\Delta t}; \xi_e^q = \text{Re}\{\xi_{e,c}^q\}$
$\Delta\chi_{e,c}^q = \chi_{e,c}^q - \chi_{e,c}^{q+1} = \chi_{e,c}^q \left[1 - e^{(-\alpha_e + j\beta_e)\Delta t} \right]; \Delta\chi_e^q = \text{Re}\{\Delta\chi_{e,c}^q\}$
$\Delta\xi_{e,c}^q = \xi_{e,c}^q - \xi_{e,c}^{q+1} = \xi_{e,c}^q \left[1 - e^{(-\alpha_e + j\beta_e)\Delta t} \right]; \Delta\xi_e^q = \text{Re}\{\Delta\xi_{e,c}^q\}$
$\psi_{e,c}^{n+1} = [\Delta\chi_{e,c}^0 - \Delta\xi_{e,c}^0] E^{n+1} + \Delta\xi_{e,c}^0 E^n + e^{(-\alpha_e + j\beta_e)\Delta t} \psi_{e,c}^n; \psi_e^{n+1} = \text{Re}\{\psi_{e,c}^{n+1}\}$

3.4.2 Second-order DNG-Mur's ABCs:

The first-order DNG-Mur's boundary is suitable for 1D problem, where the wave is propagating normal to the leftward and rightward boundaries. In more general problems, wave propagates toward boundaries at an arbitrary angle. In those cases, 2nd order approximations have been found to be useful to reduce the reflection according to the 1st order approximation. Here, 2D TM case ($\partial/\partial z \equiv 0$) is considered where only the E_z field components impinge on four walls (i.e., on $x=0$, $x=h$, $y=0$ and $y=h$ boundaries). First, propagation of left and right going waves along x direction are discussed and the wave equation in Equation (3.36) is factored using Equation (3.39a) as in the following:

$$\begin{aligned} \left(\frac{\partial^2}{\partial x^2} + \frac{\partial^2}{\partial y^2} + \frac{\omega^2}{c^2} n^2(\omega) \right) E(\omega) &= (D_x^2 + D_y^2 - D_\omega^2 n^2(\omega)) E(\omega) \\ &= (D_x + D_\omega n(\omega) \sqrt{1 - S_x^2}) (D_x - D_\omega n(\omega) \sqrt{1 - S_x^2}) E(\omega) = 0 \end{aligned} \quad (3.49)$$

where

$$D_y^2 \equiv \frac{\partial^2}{\partial y^2}, \quad D_x \equiv \frac{\partial}{\partial x}, \quad -D_\omega^2 \equiv \frac{\omega^2}{c^2}, \quad D_\omega \equiv \frac{j\omega}{c} \quad \text{and} \quad S_x^2 = \frac{D_y^2}{n(\omega)^2 D_\omega^2} \quad (3.50)$$

Using the two-term Taylor series expansion to define the square root term as $\sqrt{1 - S_x^2} \cong 1 - S_x^2/2$ and substituting S_x^2 and $n(\omega) = \varepsilon_r(\omega) = 1 + \chi_e(\omega)$ into Equation (3.49) one can write the one-way wave equation which satisfies the backward wave condition along x -direction as:

$$\begin{aligned} L_x^- E(\omega) &= \left(D_x - D_\omega n(\omega) \left(1 - \frac{S_x^2}{2} \right) \right) E(\omega) = \left(D_x D_\omega - D_\omega^2 n(\omega) + \frac{D_y^2}{2n(\omega)} \right) E(\omega) \\ &= j\omega \frac{\partial E(\omega)}{\partial x} + \frac{\omega^2}{c} E(\omega) + \frac{\omega^2}{c} P(\omega) + \frac{c}{2} R(\omega) = 0 \end{aligned} \quad (3.51)$$

where

$$P(\omega) = \chi_e(\omega) E(\omega) \quad (3.52a)$$

$$R(\omega) = \frac{\partial^2 E(\omega)}{\partial y^2} - Q(\omega) \quad (3.52b)$$

$$Q(\omega) = R(\omega) \chi_e(\omega) \quad (3.52c)$$

Taking the inverse Fourier of Equation (3.51) yields

$$c \frac{\partial^2 E(t)}{\partial t \partial x} - \frac{\partial^2 E(t)}{\partial t^2} - \frac{\partial^2 P(t)}{\partial t^2} + \frac{c^2}{2} R(t) = 0 \quad (3.53)$$

where

$$P(t) = \chi_e(t) * E(t) \quad (3.54a)$$

$$R(t) = \frac{\partial^2 E(t)}{\partial y^2} - Q(t) \quad (3.54b)$$

$$Q(t) = \chi_e(t) * R(t) \quad (3.54c)$$

where ‘*’ denotes the convolution. Similar to first order DNG-Mur’s approach, discrete forms of P , Q and R are obtained applying PLRC algorithm to Equation (3.54):

$$\left(P^{n+1} - 2P^n + P^{n-1} \right) \Big|_{(i,j)} = p_1 E^{n+1}(i, j) + p_2 E^n(i, j) + p_3 E^{n-1}(i, j) + \psi_e^n(i, j) \quad (3.55a)$$

$$R^{n+1}\Big|_{(i,j)} = \left(\frac{1}{1+p_1} \right) \left[\frac{E^{n+1}(i,j+1) - 2E^{n+1}(i,j) + E^{n+1}(i,j-1)}{\Delta y^2} - Q^n(i,j) - \xi_e^0 R^n(i,j) + \phi_e^n(i,j) \right] \quad (3.55b)$$

$$(Q^{n+1} - Q^n)\Big|_{(i,j)} = p_1 R^{n+1}(i,j) + \xi_e^0 R^n(i,j) - \phi_e^n(i,j) \quad (3.55c)$$

with $p_1 = (\chi_e^0 - \xi_e^0)$; $p_2 = (\chi_e^1 - \xi_e^1 - 2\chi_e^0 + 3\xi_e^0)$; $p_3 = (\xi_e^1 - 2\xi_e^0)$. Here, ψ_e^n and ϕ_e^n are known as the recursive accumulator and given by

$$\psi_e^n\Big|_{(i,j)} = \sum_{q=0}^{n-2} \left[(\Delta\chi_e^q - \Delta\xi_e^q) E^{n-q-1} + \Delta\xi_e^q E^{n-q-2} \right] \Big|_{(i,j)} \quad \text{with} \quad \begin{aligned} \Delta\chi_e^q &= \chi_e^{q+2} - 2\chi_e^{q+1} + \chi_e^q \\ \Delta\xi_e^q &= \xi_e^{q+2} - 2\xi_e^{q+1} + \xi_e^q \end{aligned} \quad (3.56a)$$

$$\phi_e^n\Big|_{(i,j)} = \sum_{q=0}^{n-1} \left[(\Delta\chi_{ee}^q - \Delta\xi_{ee}^q) R^{n-q} + \Delta\xi_{ee}^q R^{n-q-1} \right] \Big|_{(i,j)} \quad \text{with} \quad \begin{aligned} \Delta\chi_{ee}^q &= \chi_e^q - \chi_e^{q+1} \\ \Delta\xi_{ee}^q &= \xi_e^q - \xi_e^{q+1} \end{aligned} \quad (3.56b)$$

In order to obtain an FDTD update equation for E field to implement the 2nd order DNG-Mur's ABC on leftward DNG boundary along x-direction (where $i=1$), Equation (3.53) is discretized using central-difference expressions for the space and time derivatives (Mur, 1981) and then discrete form of P , Q and R from Equation (3.55) are substituted, which yields:

$$E^{n+1}(1,j) = \frac{1}{e_0} \left[e_1 E^{n+1}(2,j) + e_2 E^n(2,j) + e_3 E^n(1,j) - e_4 E^{n-1}(2,j) + e_5 E^{n-1}(1,j) \right] - \frac{e_6}{e_0} \left[\psi_e^n(2,j) + \psi_e^n(1,j) \right] + \frac{e_7}{e_0} \left[R^n(2,j) + R^n(1,j) \right] \quad (3.57)$$

with

$$e_0 = \frac{c\Delta t + \Delta x(1+p_1)}{2\Delta x\Delta t^2}; e_1 = \frac{c\Delta t - \Delta x(1+p_1)}{2\Delta x\Delta t^2}; e_2 = e_3 = \frac{2-p_2}{2\Delta t^2}; e_4 = \frac{c\Delta t + \Delta x(1+p_3)}{2\Delta x\Delta t^2}; e_5 = \frac{c\Delta t - \Delta x(1+p_3)}{2\Delta x\Delta t^2}; e_6 = \frac{1}{2\Delta t^2}; e_7 = \frac{c^2}{4}$$

Similar approaches are applied for the backward waves along y direction as in the following:

$$\left(D_y - D_\omega n(\omega) \left(1 - \frac{S_y^2}{2} \right) \right) E(\omega) = j\omega \frac{\partial E(\omega)}{\partial x} + \frac{\omega^2}{c} E(\omega) + \frac{\omega^2}{c} P_y(\omega) + \frac{c}{2} R_y(\omega) = 0 \quad (3.58)$$

where

$$P_y(\omega) = \chi_e(\omega) E(\omega) \quad (3.59a)$$

$$R_y(\omega) = \frac{\partial^2 E(\omega)}{\partial x^2} - Q_y(\omega) \quad (3.59b)$$

$$Q_y(\omega) = R_y(\omega) \chi_e(\omega) \quad (3.59c)$$

Then, applying PLRC algorithm to time equivalent of Equations (3.59) yield the discrete form of P_y^n , Q_y^n and R_y^n as

$$P_y(t) = \chi_e(t) * E(t) \Rightarrow P_y|_{(i,j)}^{n+1} = \left\{ 2P_y^n - P_y^{n-1} + p_1 E^{n+1} + p_2 E^n + p_3 E^{n-1} + \psi_e^n \right\} |_{(i,j)} \quad (3.60a)$$

$$R_y(t) = \frac{\partial^2 E(t)}{\partial x^2} - Q_y(t) \Rightarrow R_y|_{(i,j)}^{n+1} = \left(\frac{1}{1+p_1} \right) \left[\frac{E|_{(i+1,j)}^{n+1} - 2E|_{(i,j)}^{n+1} + E|_{(i-1,j)}^{n+1}}{\Delta x^2} - \left\{ Q_y^n + \xi_e^0 R_y^n - \phi_{ey}^n \right\} |_{(i,j)} \right] \quad (3.60b)$$

$$Q_y(t) = \chi_e(t) * R_y(t) \Rightarrow Q_y|_{(i,j)}^{n+1} = \left\{ Q_y^n + p_1 R_y^{n+1} + \xi_e^0 R_y^n - \phi_{ey}^n \right\} |_{(i,j)} \quad (3.60c)$$

with $p_1 = (\chi_e^0 - \xi_e^0)$; $p_2 = (\chi_e^1 - \xi_e^1 - 2\chi_e^0 + 3\xi_e^0)$; $p_3 = (\xi_e^1 - 2\xi_e^0)$.

Here, ψ_e^n and ϕ_{ey}^n are known as the recursive accumulator and presented in Equation (3.56a) and Equation (3.61).

$$\phi_{ey}^n \Big|_{(i,j)} = \sum_{q=0}^{n-1} \left[(\Delta\chi_{ee}^q - \Delta\xi_{ee}^q) R_y^{n-q} + \Delta\xi_{ee}^q R_y^{n-q-1} \right] \Big|_{(i,j)} \quad \text{with} \quad \begin{aligned} \Delta\chi_{ee}^q &= \chi_e^q - \chi_e^{q+1} \\ \Delta\xi_{ee}^q &= \xi_e^q - \xi_e^{q+1} \end{aligned} \quad (3.61)$$

Then discretizing of time equivalent of Equation (3.58) using central-difference expressions for the space and time derivatives and substituting discrete form of P_y , Q_y and R_y given in Equation (3.60), we can derive the FDTD update equation for E^{n+1} on backward boundary along y-direction (where j=1):

$$\begin{aligned} E^{n+1}(i,1) = \frac{1}{e_0} & \left[e_1 E^{n+1}(i,2) + e_2 E^n(i,2) + e_3 E^n(i,1) - e_4 E^{n-1}(i,2) + e_5 E^{n-1}(i,1) \right] \\ & - \frac{e_6}{e_0} \left[\psi_e^n(i,2) + \psi_e^n(i,1) \right] + \frac{e_7}{e_0} \left[R_y^n(i,2) + R_y^n(i,1) \right] \end{aligned} \quad (3.62)$$

with

$$e_0 = \frac{c\Delta t + \Delta x(1+p_1)}{2\Delta x\Delta t^2}; e_1 = \frac{c\Delta t - \Delta x(1+p_1)}{2\Delta x\Delta t^2}; e_2 = e_3 = \frac{2-p_2}{2\Delta t^2}; e_4 = \frac{c\Delta t + \Delta x(1+p_3)}{2\Delta x\Delta t^2}; e_5 = \frac{c\Delta t - \Delta x(1+p_3)}{2\Delta x\Delta t^2}; e_6 = \frac{1}{2\Delta t^2}; e_7 = \frac{c^2}{4}.$$

The DNG-Mur ABC on the other edges both for x and y directions can be found in a similar way presented above and parameters for both Drude and Lorentz model are listed in Table 3.2.

Table 3.2 Parameters for Drude and Lorentz Model in 2nd order DNG-Mur ABC

Drude Model	
$\chi_e^q = \frac{\omega_{pe}^2}{\Gamma_e} \left[\Delta t + \frac{1}{\Gamma_e} e^{-q\Gamma_e \Delta t} A \right] \Rightarrow \left\{ \begin{array}{l} \Delta \chi_{ee}^q = \chi_e^q - \chi_e^{q+1} = -\frac{\omega_{pe}^2}{(\Gamma_e)^2} e^{-q\Gamma_e \Delta t} A^2 \\ \Delta \chi_e^q = \chi_e^{q+2} - 2\chi_e^{q+1} - \chi_e^q = \frac{\omega_{pe}^2}{(\Gamma_e)^2} e^{-q\Gamma_e \Delta t} A^3 \end{array} \right.$	$\xi_e^q = \frac{\omega_{pe}^2}{\Gamma_e \Delta t} \left[\frac{\Delta t^2}{2} + \frac{e^{-q\Gamma_e \Delta t}}{\Gamma_e} B \right] \Rightarrow \left\{ \begin{array}{l} \Delta \xi_{ee}^q = \xi_e^q - \xi_e^{q+1} = -\frac{\omega_{pe}^2}{(\Gamma_e)^2} A B e^{-q\Gamma_e \Delta t} \\ \Delta \xi_e^q = \xi_e^{q+2} - 2\xi_e^{q+1} + \xi_e^q = \frac{\omega_{pe}^2}{(\Gamma_e)^2} A^2 B e^{-q\Gamma_e \Delta t} \end{array} \right.$
$\text{with } A = (e^{-\Gamma_e \Delta t} - 1) \quad B = \left(\Delta t e^{-\Gamma_e \Delta t} + \frac{(e^{-\Gamma_e \Delta t} - 1)}{\Gamma_e} \right)$	
$\psi_e^{n+1}(i, j) = [\Delta \chi_e^0 - \Delta \xi_e^0] E^n(i, j) + \Delta \xi_e^0 E^{n-1}(i, j) + e^{-\Gamma_e \Delta t} \psi_e^n(i, j)$	
$\phi_e^{n+1}(i, j) = [\Delta \chi_e^0 - \Delta \xi_e^0] R^{n+1}(i, j) + \Delta \xi_e^0 R^n(i, j) + e^{-\Gamma_e \Delta t} \phi_e^n(i, j)$	
$\phi_{ey}^{n+1}(i, j) = [\Delta \chi_e^0 - \Delta \xi_e^0] R_y^{n+1}(i, j) + \Delta \xi_e^0 R_y^n(i, j) + e^{-\Gamma_e \Delta t} \phi_{ey}^n(i, j)$	
Lorentz Model	
$\chi_{e,c}^q = \frac{-j\gamma_e}{\alpha_e - j\beta_e} \left[1 - e^{(-\alpha_e + j\beta_e)\Delta t} \right] e^{(-\alpha_e + j\beta_e)q\Delta t} \Rightarrow \chi_e^q = \text{Re} \{ \chi_{e,c}^q \}$	
$\Delta \chi_{ee,c}^q = \chi_{e,c}^q - \chi_{e,c}^{q+1} = \chi_{e,c}^q \left(1 - e^{(-\alpha_e + j\beta_e)\Delta t} \right) \Rightarrow \Delta \chi_{ee}^q = \text{Re} \{ \Delta \chi_{ee,c}^q \}$	
$\Delta \chi_{e,c}^q = \chi_{e,c}^{q+2} - 2\chi_{e,c}^{q+1} - \chi_{e,c}^q = \chi_{e,c}^q \left(1 - e^{(-\alpha_e + j\beta_e)\Delta t} \right)^2 \Rightarrow \Delta \chi_e^q = \text{Re} \{ \Delta \chi_{e,c}^q \}$	
$\xi_{e,c}^q = \frac{j\gamma_e}{\Delta t (\alpha_e - j\beta_e)^2} \left[e^{(-\alpha_e + j\beta_e)\Delta t} C - 1 \right] e^{(-\alpha_e + j\beta_e)q\Delta t} \Rightarrow \xi_e^q = \text{Re} \{ \xi_{e,c}^q \} \quad \text{with } C = (1 + (\alpha_e - j\beta_e)\Delta t)$	
$\Delta \xi_{ee,c}^q = \xi_{e,c}^q - \xi_{e,c}^{q+1} = \xi_{e,c}^q D \Rightarrow \Delta \xi_{ee}^q = \text{Re} \{ \Delta \xi_{ee,c}^q \}$	
$\Delta \xi_{e,c}^q = \xi_{e,c}^{q+2} - 2\xi_{e,c}^{q+1} + \xi_{e,c}^q = \xi_{e,c}^q D^2 \Rightarrow \Delta \xi_e^q = \text{Re} \{ \Delta \xi_{ee,c}^q \}$	
$\psi_{e,c}^{n+1}(i, j) = [\Delta \chi_{e,c}^0 - \Delta \xi_{e,c}^0] E^n(i, j) + \Delta \xi_{e,c}^0 E^{n-1}(i, j) + e^{(-\alpha_e + j\beta_e)\Delta t} \psi_{e,c}^n(i, j)$ $\Rightarrow \psi_e^{n+1}(i, j) = \text{Re} \{ \psi_{e,c}^{n+1}(i, j) \}$	
$\phi_{e,c}^{n+1}(i, j) = [\Delta \chi_{ee,c}^0 - \Delta \xi_{ee,c}^0] R^{n+1}(i, j) + \Delta \xi_{ee,c}^0 R^n(i, j) + e^{(-\alpha_e + j\beta_e)\Delta t} \phi_{e,c}^n(i, j)$ $\Rightarrow \phi_e^{n+1}(i, j) = \text{Re} \{ \phi_{e,c}^{n+1}(i, j) \}$	
$\phi_{ey,c}^{n+1}(i, j) = [\Delta \chi_{ee,c}^0 - \Delta \xi_{ee,c}^0] R_y^{n+1}(i, j) + \Delta \xi_{ee,c}^0 R_y^n(i, j) + e^{(-\alpha_e + j\beta_e)\Delta t} \phi_{ey,c}^n(i, j)$ $\Rightarrow \phi_{ey}^{n+1}(i, j) = \text{Re} \{ \phi_{ey,c}^{n+1}(i, j) \}$	

3.5 Numerical Results

In this section, numerical results are presented which are obtained by using 1D and 2D ADE-FDTD algorithm based on Maxwell's curl equations for Lorentz material. The accuracy and absorbing performance of the proposed DNG Mur's ABC are also displayed and compared with DNG-UPML ABCs in terms of memory usage and computational time. Numerical results are also given for ADE-FDTD algorithm based on wave equations when the computational domain is entirely loaded with Lorentz type DNG medium and terminated with the 1st and 2nd order DNG-Mur's ABC in 1D and 2D cases. The comparison of memory/computation time requirements for FDTD simulations based on wave and curl equations are presented. The ADE and PLRC-FDTD approaches for ENG media are given in (Pekmezci, Topuz, & Sevgi, 2016). Another simple way of obtaining ADE-FDTD formulations for Lorentz type-ENG media using wave and curl equations is to select the plasma frequency (ω_{pm}) of magnetic permeability as zero in the formulations developed for DNG media.

3.5.1 On propagation characteristics of DNG media

In Figure 3.4, numerical results are given, obtained by using ADE FDTD algorithm based on Maxwell's curl equations described in Section 3.2.2 for Lorentz material with the parameters $f_{oe} = f_{om} = 0.1591\text{GHz}$, $f_{pe} = f_{pm} = 1.1027\text{GHz}$ and $\Gamma = 1 \times 10^8 \text{ rad/s}$ which has negative real part of permittivity and permeability in the range of $[1 \times 10^9, 7 \times 10^9] \text{ rad/s}$. One-dimensional (1D) problem space is taken to be 400 cells along x-direction and a DNG slab extends from cell 160 to cell 240 where the outside of this range is free space. A sinusoidal source with a center frequency about 0.75GHz is launched in the free space region at a node 80 cells from the left boundary and both ends of the problem space is terminated with first order Mur-type absorbing blocks. Cell size is chosen as $\Delta x = \lambda / 40$ and the corresponding time step is calculated using $\Delta t = 0.95\Delta x / c$ where λ is free space wavelength and c is speed of light, respectively. In Figure 3.4, snapshot of the spatial electric field distribution at the 630th time step and the behavior of wave propagation in DNG region are presented. As seen in Figure 3.4a, wave propagates in the reverse direction in DNG region, but retains its normal propagation when it exits the DNG region. It can also be seen by comparing early and late time responses in the DNG region as given

in Figure 3.4b and Figure 3.4c. Time histories of the waves are recorded at three different nodes inside the DNG region which are labeled according to their distance to the source. The first node is 20 cells before the center node; the second node is the center node; and the last one is 20 cells after the second node. Normally, waves will reach the first node first, then the second node and finally the third node as observed in Figure 3.4b. This shows early time responses and the causality in the direction of the wave propagation is preserved in DNG region as reported in (Heyman & Ziolkowski, 2001). However, as shown in Figure 3.4c, the late time responses are different than the early time response due to the result of negative refractive index of DNG region.

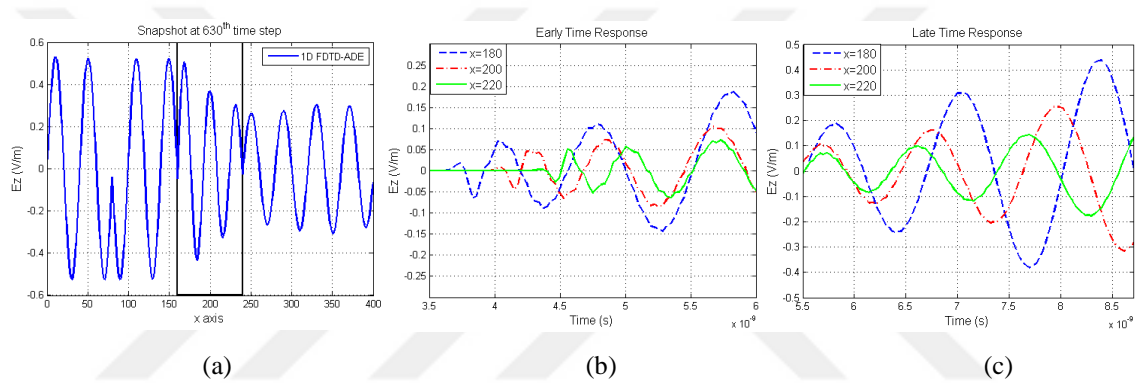


Figure 3.4 Plot of E-field vs. position and time at three different nodes using 1D ADE-FDTD algorithm
 a) E -field at a given time instant, b) Early time response and c) Late time response

In 2D scenario, simulations of ADE-FDTD approach are used to observe focusing and direction of propagation of a Gaussian beam when the refractive index of DNG slab is -1. DNG slab is modelled by identical Lorentz parameters for $\epsilon_r(\omega)$ and $\mu_r(\omega)$ where $f_{pe} = f_{pm} = 8.3081\text{MHz}$, $f_{oe} = f_{om} = 1.1992\text{MHz}$ and $\Gamma_e = \Gamma_m = 0$ as used in (Pekmezci & Sevgi, 2014). The computational domain has 400x400 grid points (on xy-plane) and DNG slab with 360x120 cells ($K_{x1}=20$, $K_{x2}=380$, $K_{y1}=120$, $K_{y2}=240$) is inserted in free space region as illustrated in Figure 3.5. A sinusoidal source at a center frequency of $f_o = 6\text{MHz}$ is used in the simulations and source is injected at $x_s=200$ and $y_s=60$. The cell size is the same in both directions that equals to $\Delta x = \Delta y = \lambda / 40$ and time step is calculated about $\Delta t = 2.79\text{ns}$ considering the Courant-Friedrichs-Lewy (CFL) stability condition. The FDTD grid of free space region is terminated with second order Mur's ABC (Mur, 1981).

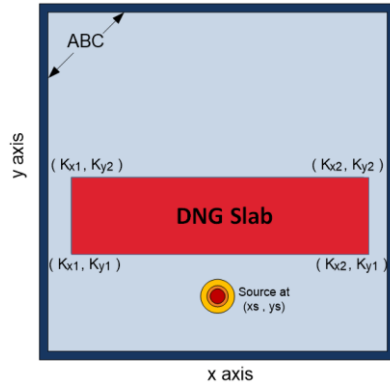


Figure 3.5 The 2D FDTD scenario and the location of the metamaterial region

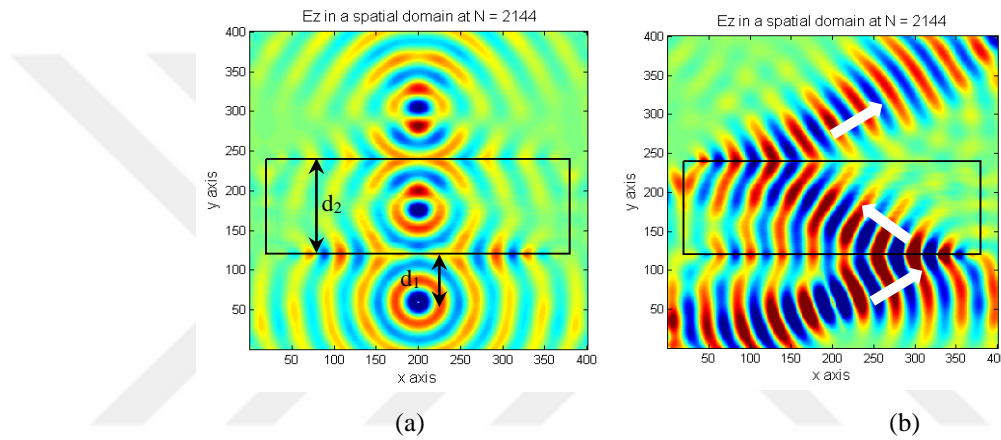


Figure 3.6 Propagation through DNG slab with $n=-1$ a) Focusing and b) Direction of propagation

In Figure 3.6a, perfect focusing is demonstrated when a localized source with sinusoidal time variation is normally incident on a lossless DNG slab. Since the slab thickness is $d_2=120\Delta y$ in the direction of propagation and source-to-slab distance is $d_1=60\Delta y < d_2$, re-focusing occur inside the DNG slab (at 60 cells away from the front face) and in free space region at 60 cells behind the slab. This is agreement with the perfect focusing condition for the case of $n=-1$ as reported in (Pendry, 2000), where the first focus occurs inside the slab at $d_{f1}=d_1$, and second focus at $d_{f2}=d_2-d_1$ beyond the slab. In Figure 3.6b, an array of sources having Gaussian beam-type spatial variation and sinusoidal time dependence (Çakır, Çakır, & Sevgi, 2008) are used to create an obliquely propagating wave at an angle of 20° with y axis to show the backward wave propagation in DNG slab. As seen in figure the wave propagates in the reverse direction in the DNG region, but retains its normal propagation when it exits the DNG region. Hence, one can clearly observe the inverse Snell effect consulting the arrows that show the direction of the beam propagation.

3.5.2 On effectiveness of developed DNG-Mur ABC

In this section, numerical results are presented both for 1D and 2D cases where the problem space is filled entirely with DNG medium modelled by identical Lorentz parameters for $\epsilon_r(\omega), \mu_r(\omega)$ and boundaries on both sides are terminated with proposed DNG-Mur ABCs. In all simulations, a tapered sinusoidal pulse (5-10-5 pulse described in (Heyman & Ziolkowski, 2001)) is used as excitation with a center frequency of $f_s = 7.5$ GHz and inserted at the center of the FDTD grid. Time – frequency domain variation of the source signal is shown in Figure 3.7.

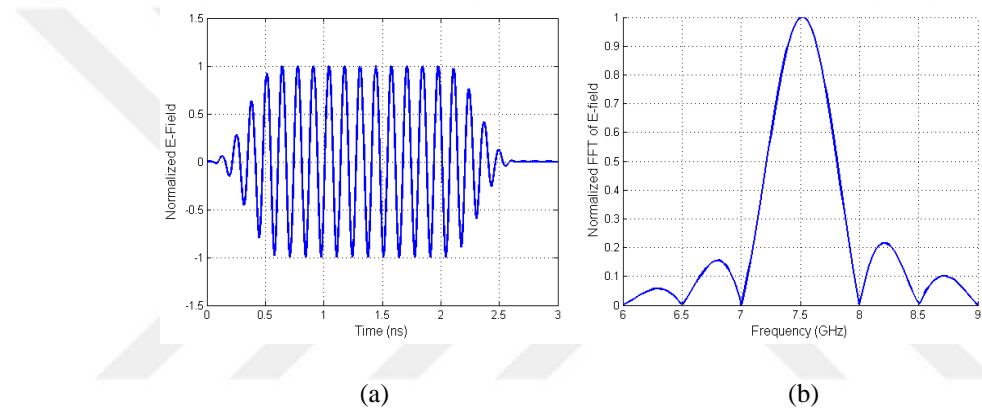


Figure 3.7 The time history and frequency spectrum of the electric field E_z (E_{inc}) measured at the center of the computational grid

The Lorentz type medium parameters are chosen as $\omega_{pe} = \omega_{pm} = \omega_s \sqrt{48/25}$, $\omega_{oe} = \omega_{om} = \omega_s/5$ and $\Gamma_e = \Gamma_m = \omega_s/200$ which yields a refractive index about -1 at the center frequency ($\omega_s = 2\pi f_s$). FDTD grid parameters are $\Delta x = \lambda/60 = 0.067$ cm for 1D case and $\Delta x = \Delta y = \lambda/20 = 0.2$ cm for 2D case with a time step of 0.5 times the Courant limit, respectively. Total FDTD domain is chosen as 1000 grid and 400x400 grid for 1D and 2D scenarios, respectively. With these parameters, the developed 1st and 2nd order DNG-Mur algorithms are stable for at least 100,000 time steps and stability of the proposed 2D DNG-Mur algorithm is demonstrated in Figure 3.8 at different time steps. Here, a line source is located at mid- point of the 2D FDTD space. As observed, late time response does not have any discernable reflections.

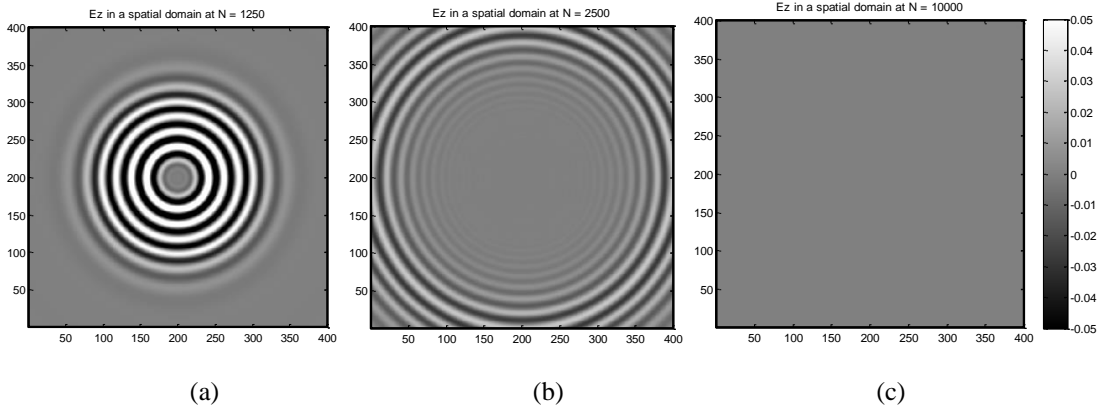


Figure 3.8 Snapshots of Ez field using 2nd order DNG-Mur at time-steps: a)1250, b)2500 and c)10000

The absorbing performance of the proposed formulations in 1D and 2D cases are illustrated via calculating the reflections from the DNG-Mur boundaries. The reflection coefficient at an observation point is determined by calculating the test and reference field strength versus time using proposed FDTD formulations given in Section 3.2.2. The calculations are done in two steps as suggested in (Zheng, Tam, Ge, & Xu, 2009). In the first step, the test field (E_{test}) is calculated at an observation point 2-cells away from the DNG-Mur boundary. In the second step, incident field (E_{inc}) is obtained by repeating the same calculations, but now considering a larger domain so that boundary reflected fields cannot reach the observation point during the time window of step one. The reflected field can then be obtained as $E_{\text{ref}}(t) = E_{\text{test}}(t) - E_{\text{inc}}(t)$. Then, the reflection coefficient at each frequency is calculated by dividing the discrete Fourier transforms (DFT) of reflected field and incident fields. In Figure 3.9a, frequency spectrum of the incident field is shown together with reflection coefficients obtained using DNG-Mur ABCs in 1D and 2D scenarios. For comparison purposes the reflection coefficients obtained using 10-cell thick DNG-UPML ABCs are also plotted. Our numerical results show that 1D and 2D DNG-Mur ABCs effectively reduce reflections to about -60dB and -50dB level over the 7.1–7.9 GHz band under the main lobe, which may be acceptable in many applications and provide stable results. We have also calculated the reflection coefficients performance of proposed DNG-Mur ABCs for the case of non-identical Lorentz models using arithmetic mean approach outlined in Section 3.3.2. The results obtained with the same parameters for $\chi_c(\omega)$, but $\omega_{pm} = \omega_s$, $\omega_{om} = \omega_s/\sqrt{2}$ and $\Gamma_m = \omega_s/200$ for $\chi_m(\omega)$ are found to differ less than ± 3 dB from those shown in Figure 3.9a, over the entire frequency range.

In Figure 3.9b, the relative error performance of the proposed 1D and 2D DNG-Mur is given together with that of the 10-cell thick DNG-UPML and the computation time and memory requirements for both approaches are listed in Table 3.3 which indicate that the DNG-Mur provides definite advantages both in memory and computation time (less memory and computational time) over DNG-UPML. The proposed algorithm based on Mur's ABC is faster than the UPML ABC, and requires less memory usage.

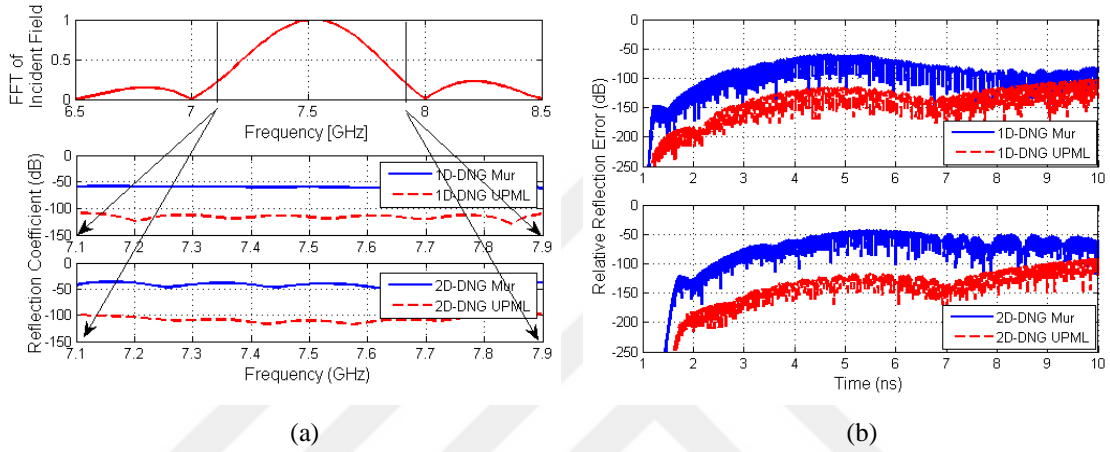


Figure 3.9 Comparison of DNG-Mur and DNG-UPML for 1D and 2D scenarios

a) Frequency spectrum of incident field and reflection coefficients, b) Relative error in dB versus time

Table 3.3 Memory usage and computation time in FDTD simulations both for DNG-Mur and DNG-UPML ABCs

FDTD grid		Time(s)	Memory(MB)
2D Case (1000x1000 cells) $t=5000\Delta t$	Mur	1693.9	244.45
	UPML	3881.5	516.98
1D Case (1000 cells) $t=10000\Delta t$	Mur	1.73	0.72
	UPML	2.65	0.87

As a second 2D test a DNG slab is considered with a thickness along y-direction about $100\Delta y$ imbedded in air, extending infinitely in x, z, and excited by a z-directed line source. We have used 50-1000-50 cycle source at $f_s = 7.5$ GHz. This yields near-perfect match conditions as steady-state conditions set up, and the refractive index of the slab approaches to -1. In order to demonstrate the effectiveness of the proposed extension of Mur formalism to DNG media we performed two simulation runs, one using DNG-Mur and the other using Standard-Mur at slab boundaries. For the first simulation, boundaries

of the 400×400 grid size computational domain are terminated with standard 2D Mur ABC for air, and with 2D DNG-Mur ABC for the DNG slab boundaries at y -grid points between 150 and 250 (See Figure 3.10a). For the second simulation, standard 2D Mur ABC is used at all boundaries (both air and DNG slab, See Figure 3.11a). The line source is placed at the point $x=200\Delta x$, $y=100\Delta y$, i.e. at a distance $50\Delta y$ from the DNG slab for both simulations, and typical outputs are depicted in Figure 3.10 and Figure 3.11, respectively.

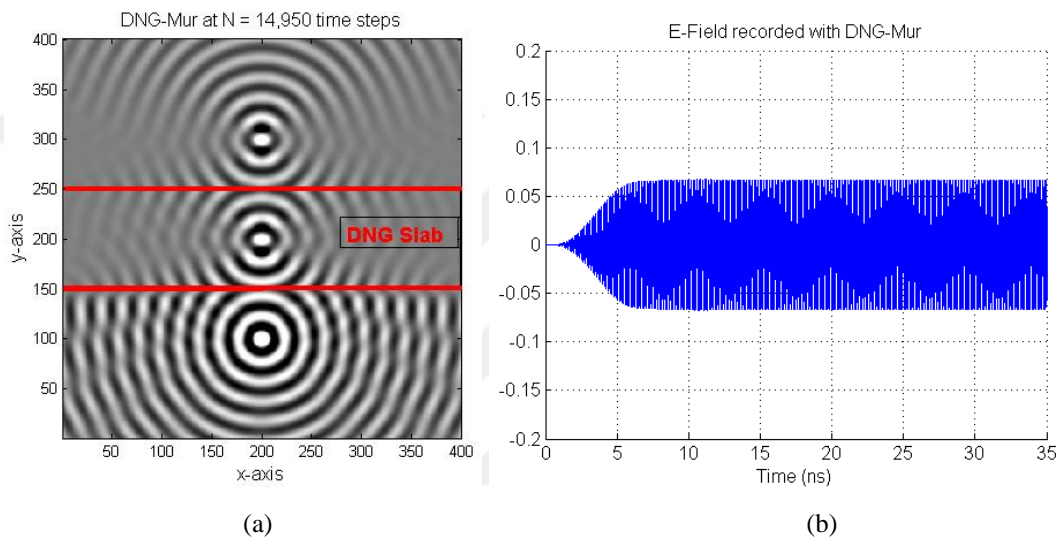


Figure 3.10 a) Snapshot of propagation and b) E field recorded at an observation point when DNG slab boundaries are truncated with DNG - Mur.

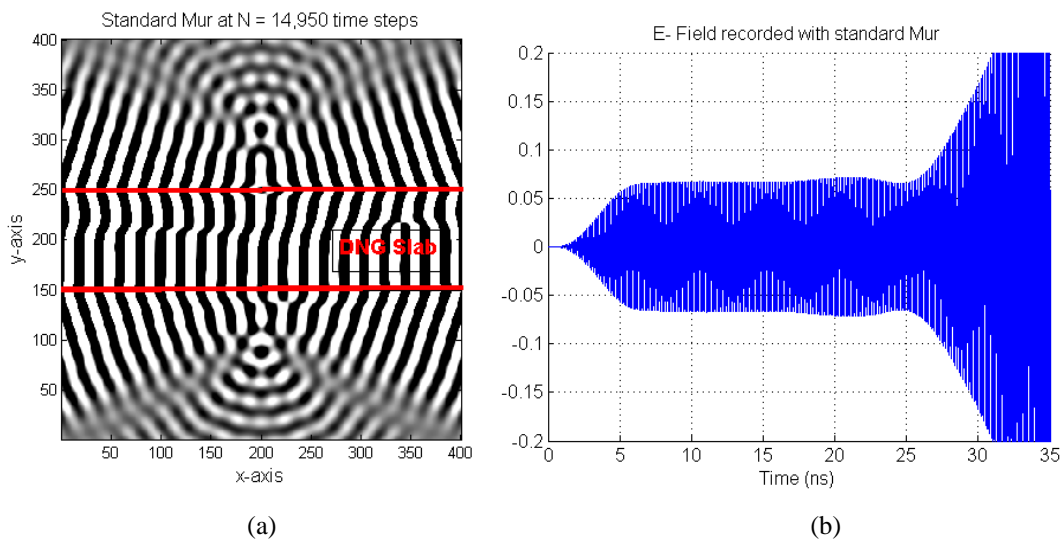


Figure 3.11 a) Snapshot of propagation and b) E field recorded at an observation point when DNG slab boundaries are truncated with Standard Mur.

The snapshot given in Figure 3.10a clearly shows the cylindrical wave fronts emanating from the source, as well as from the anticipated image locations (Heyman & Ziolkowski, 2001; Pendry, 2000) inside and behind the slab. In Figure 3.10b the time history of the E field at an observation point located between source and slab is given which demonstrates the stability of the code when terminating slab boundaries with DNG-Mur. Figure 3.11a and Figure 3.11b correspond to similar outputs obtained when, at slab boundaries, DNG-Mur is replaced with standard Mur. Figure 3.11 show that reflections from improperly terminated boundaries of the DNG slab results in instability after about 10,000 time steps, and completely corrupts field distribution inside the computational domain by about 15,000 time steps, as shown in Figure 3.11a.

3.5.3 On wave equation based FDTD algorithm

In order to perform the accuracy and performance of the 1D and 2D ADE-FDTD algorithm based on wave equation we compare the results obtained via wave equation based FDTD with Maxwell's curl equation based. In all simulations 1D and 2D domains are entirely filled with DNG medium modelled by Lorentz type material and boundaries are truncated with the 1st order and 2nd order DNG-Mur ABCs, respectively. A sinusoidal source (5-10-5 pulse) is used as excitation with a center frequency of $f_s = 7.5\text{GHz}$ and DNG medium parameters are defined as $\omega_{pe} = \omega_{pm} = \omega_p = \omega_s \sqrt{48} / 5$, $\omega_{oe} = \omega_{om} = \omega_o = \omega_s / 5$ and $\Gamma_e = \Gamma_m = \omega_s / 200$ which yield a negative refractive index about -1 at f_s . Total 1D computational domain is $1000\Delta x$ cells and electric field waveforms are recorded at an observation point that is 10 cells away the left DNG-Mur boundary. Simulations are performed for 10,000 time steps. Length of each cell ($\Delta x = \lambda / 60$) and time step (Δt) which satisfies Courant-Friedrichs-Lewy (CFL) condition are calculated as 0.0667 cm and 1.1ps, respectively. For 2D computational domain, FDTD grid is chosen as 400×400 along x and y directions and grid parameters are chosen as $\Delta x = \Delta y = \lambda / 20$ with a time step of 0.5 times the Courant limit. For both 1D and 2D cases the numerical results obtained using wave equation and curl equation based FDTD algorithms are in perfect agreement. Hence, E field intensity obtained by curl equation (solid line) and wave equation (dashed line) is presented only for 1D case in Figure 3.12. The significant difference between FDTD simulations based on wave and curl equations is seen in

comparison of memory and time requirements. As listed in Table 3.4, wave equation based formulation needs approximately %30 less computation time and memory requirements in 2D case, whereas requirements are almost identical in 1D case.

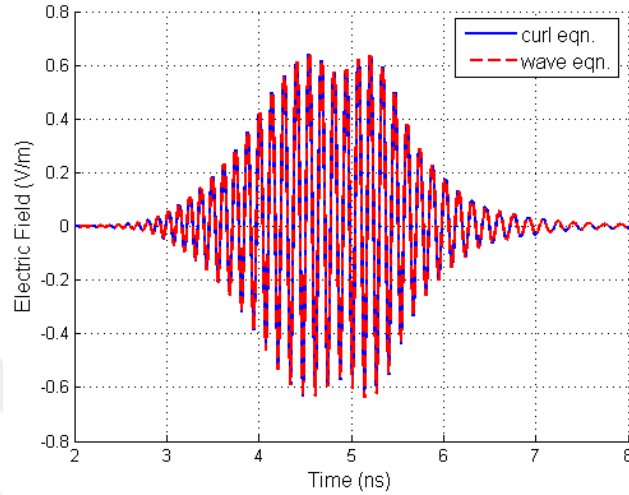


Figure 3.12 Comparison of 1D FDTD algorithm based on wave and curl equations in Lorentz type DNG medium.

Table 3.4 Memory / time requirements of FDTD simulations based on wave and curl equations

FDTD grid		Time(s)	Memory(MB)
2D Case (400x400 cells) t=5000Δt	2Dcurl_ADE	185.5	39.37
	2Dwave_ADE	128	30.82
1D Case (1000 cells) t=10000Δt	1Dcurl_ADE	6.36	0.74
	1Dwave_ADE	5.14	0.71

In order to demonstrate the validity and accuracy of wave equation based ADE and PLRC formulations for reflection of waves normally incident at free space-ENG interface one dimensional problem space is considered consisting of 600 cells out of which the first 299 cells are free space and the remaining 301 cells are ENG medium. The ENG medium is modeled by Lorentz-type material with the parameters of $f_{oe}=0.1591GHz$, $f_{pe}=1.1027GHz$ and damping factor $\Gamma_e=1\times 10^8 rad/s$. The problem parameters considered here are identical to the ones reported in (Pekmezci, Topuz, & Sevgi, 2016). Spatial length and temporal step sizes are 6.3mm and 10.47ps, respectively. Gaussian pulse inserted at 60th cell is used as excitation and the propagation of normally incident wave toward the

ENG medium and reflection from the free space-ENG interface at two time instants is depicted in Figure 3.13. As seen in figure, ENG medium almost perfectly reflects the incident wave, since it does not support propagating waves as noted in Section 2.2.

The corresponding reflection coefficient at an observation point (two cells in front of the interface) is determined by calculating the incident and reflected field strength versus time using proposed wave equation based FDTD formulations (Pekmezci, Topuz, & Sevgi, 2016) in two steps. First calculation is performed to obtain the incident field by considering the free space parameters for the entire problem space. Second calculation is performed to obtain total field at the observation point. The reflected field is obtained by subtracting the incident field result from the total field result. Then, the reflection coefficient at each frequency is calculated by dividing the DFT of reflected field and incident fields. In Figure 3.14a, relative permittivity of ENG medium is drawn in two different frequency regions. First region ($0-4\times 10^9$ rad/s) contains the transition of the real part of permittivity from positive to negative (at $\omega=1\times 10^9$ rad/s) values, and the second region ($4\times 10^9-12\times 10^9$ rad/s), displays its transition from negative to positive (at $\omega=7\times 10^9$ rad/s) values.

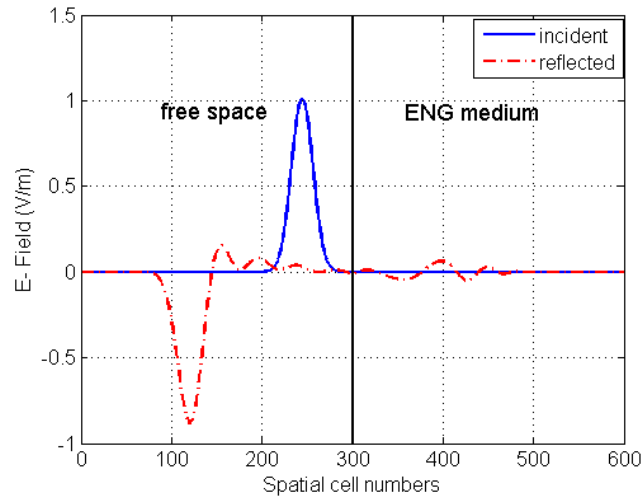


Figure 3.13 The Gaussian pulse propagating toward the ENG medium (at $t=500\Delta t$) and reflecting from the free space-ENG medium interface (at $t=1000\Delta t$)

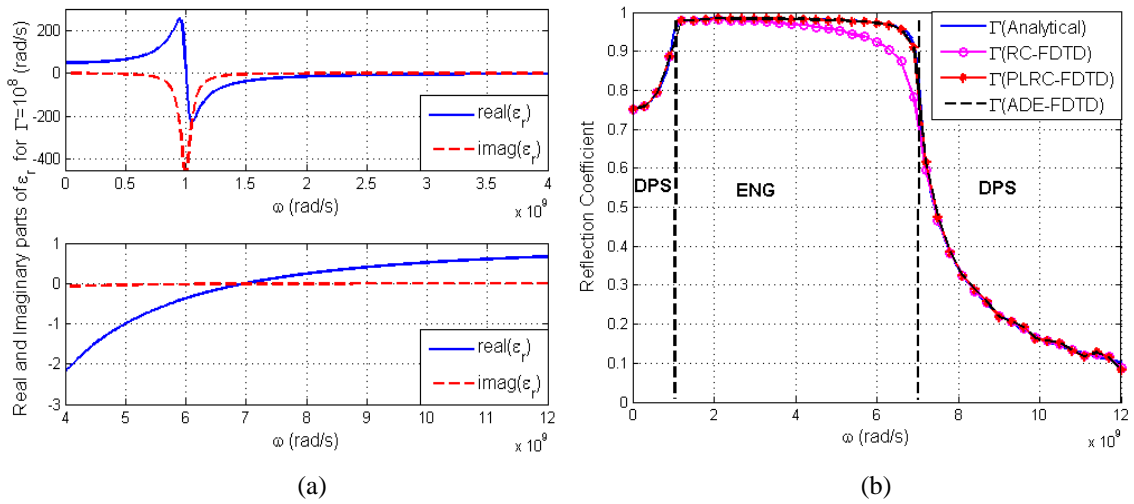


Figure 3.14 a) Real and imaginary part of permittivity, b) Reflection coefficients vs. frequency

With the aid of Figure 3.14a, one can physically interpret the variation of the reflection coefficient shown in Figure 3.14b. As expected the wave is almost perfectly reflected from the interface in the frequency region where the medium exhibits ENG characteristics and does not support transmission, whereas reflection decreases in region exhibiting DPS characteristics supporting propagation of wave. In Figure 3.14b, numerical results obtained via FDTD algorithm based on ADE, PLRC, and RC approaches are compared with the exact solution of the reflection coefficient which can be obtained using Equation (4.31a) and Equation (4.33) with $\mu_{r_2}=1$ and ϵ_{r_2} by the Lorentz model given above. As seen from this figure, ADE and PLRC formulations yield much better accuracy than the RC-FDTD formulation and an excellent agreement is observed with the analytical solution.

4. ANALYTICAL SOLUTIONS OF WAVE PROPAGATION IN A RECTANGULAR WAVEGUIDE LOADED WITH DNG SLABS

4.1 Introduction

For some waveguide configurations, such as partially filled waveguides with the material interface perpendicular to the x or y axis, TE or TM modes (with respect to the axial coordinate z) cannot satisfy the boundary conditions of the structure. However, field configurations that are combinations of TE and TM modes do of course satisfy the boundary conditions of such a partially filled waveguide. On the other hand, wave fields in these structures can also be expressed with single mode types having TE or TM characteristics with respect to one transverse coordinate which are referred to as longitudinal section electric (LSE) or longitudinal section magnetic (LSM) modes (Balanis, 2012).

There are several reports in the literature investigating propagation characteristics and potential applications of metamaterial loaded planar and rectangular waveguides (Alu & Engheta, 2004; Nefedov & Tretyakov, 2003; Cory & Shtrom, 2004; Kim, 2009; Siakavara, 2007; Baccarelli et al., 2005; Yongmei & Shanjia, 2009). It has already been shown that, in certain frequency and parameter regions such environments support forward, backward and surface wave type solutions and yield complex values of propagation constant in the absence of losses. These investigations are focused on problems dealing with specific applications or propagation characteristics, often using the rather restrictive assumption of nondispersive DNG media (Nefedov & Tretyakov, 2003; Cory & Shtrom, 2004; Kim, 2009; Siakavara, 2007). It is well known that causality dictates the satisfaction of Kramers-Kronig relations by the constitutive medium parameters (Jackson, 1998), hence, except when considering single frequencies (as in (Alu & Engheta, 2004)) or sufficiently narrow frequency bands one needs to refer to DNG medium models which account for medium dispersion and losses, such as the Lorentz and Drude models introduced in Chapter 2.

In this chapter analytic solution of rectangular waveguide partially and fully loaded with DNG slab is presented. Derivation of eigenvalue equation in a rectangular waveguide loaded with three-layer DNG slab is reviewed and then reduced to two-layer and single layer slab equations. In all numerical calculations Lorentz model is used for DNG medium, and the eigenvalue equation obtained for two-layer slab for investigating the dispersive properties of evanescent, propagating and complex modes and determining the modal cutoff transitions leading to novel contributions regarding the existence conditions.

4.2 Eigen Solutions in DNG Loaded Regions

The structure under consideration is shown in Figure 4.1. It consists of a rectangular waveguide of cross section $a \times b$, partially loaded with DNG slabs fully extending along the direction of the narrow wall, y . The length of slab along z -direction is denoted by ℓ and position along x -direction by t_i ($i=1,2$).

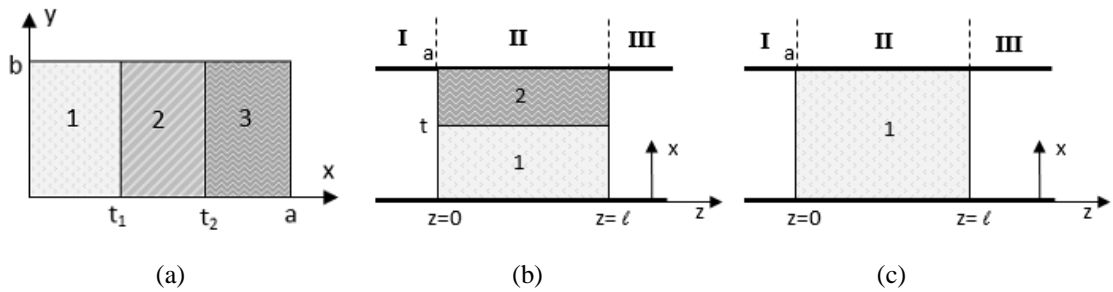


Figure 4.1 Configuration of rectangular waveguide filled with a) three-layers (front view), b) two-layers and c) single layer where regions (I-III) are free space and region (II) is DNG slab (top view).

Considering TE_x type solutions which do not depend on y , i.e., $\partial/\partial y=0$ and $E_x=0$, pertaining field components yield:

$$\nabla \times \vec{E} = -j\omega\mu\vec{H} \Rightarrow -j\omega\mu\vec{H} = -\vec{a}_x \frac{\partial E_y}{\partial z} - \vec{a}_y \frac{\partial E_z}{\partial x} + \vec{a}_z \frac{\partial E_y}{\partial x} \quad (4.1)$$

$$\nabla \times \vec{H} = j\omega\varepsilon\vec{E} \Rightarrow j\omega\varepsilon\vec{E} = -\vec{a}_x \frac{\partial H_y}{\partial z} - \vec{a}_y \left(\frac{\partial H_z}{\partial x} - \frac{\partial H_x}{\partial z} \right) + \vec{a}_z \frac{\partial H_y}{\partial x} \quad (4.2)$$

Since $E_x = 0$, $H_y = 0$ and $E_z = 0$, the non-vanishing field components appear as E_y, H_x and H_z . Hence the modes can also be classified as TE_{m0} . We further note that the continuity of field components parallel to medium interfaces implies that the x and z derivatives of E_y will be discontinuous at these interfaces as illustrated in Figure 4.2.

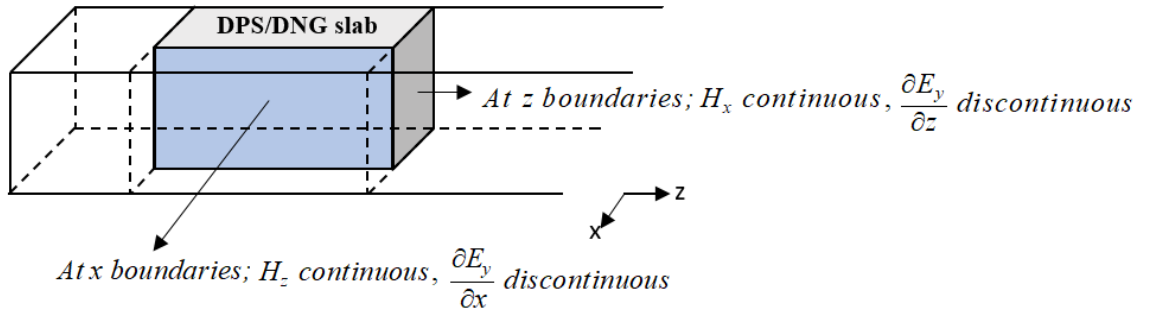


Figure 4.2 Continuity and discontinuity of fields at air-slab interfaces

For three-layer DNG slab configuration depicted in Figure 4.1a, z-dependence in slab regions are identical and suppressed in deriving the eigenvalue equation for the modal solutions in $z \in (0, \ell)$. Then the mode functions are defined as:

$$E_y = \begin{cases} A \sin(k_{x1}x) & ; 0 \leq x \leq t_1 \\ B \sin(k_{x2}x) + C \cos(k_{x2}x) & ; t_1 \leq x \leq t_2 \\ D \sin[k_{x3}(a-x)] & ; t_2 \leq x \leq a \end{cases} \quad (4.3)$$

$$H_z = \frac{j}{\omega\mu} \frac{\partial E_y}{\partial x} = \frac{j}{\omega\mu_0} \begin{cases} \frac{k_{x1}}{\mu_{r1}} A \cos(k_{x1}x) & ; 0 \leq x \leq t_1 \\ \frac{k_{x2}}{\mu_{r2}} [B \cos(k_{x2}x) - C \sin(k_{x2}x)] & ; t_1 \leq x \leq t_2 \\ -\frac{k_{x3}}{\mu_{r3}} D \cos[k_{x3}(a-x)] & ; t_2 \leq x \leq a \end{cases} \quad (4.4)$$

Imposing continuity of E_y and H_z on $x = t_1, t_2$ boundaries, the eigenvalue equation is obtained as,

$$\begin{aligned}
& \frac{k_{x1} k_{x2}}{\mu_{r1} \mu_{r2}} \cos(k_{x1} t_1) \sin k_{x3} (a-t_2) \cos k_{x2} (t_2-t_1) \\
& + \frac{k_{x2} k_{x3}}{\mu_{r2} \mu_{r3}} \sin(k_{x1} t_1) \cos k_{x3} (a-t_2) \cos k_{x2} (t_2-t_1) \\
& + \frac{k_{x1} k_{x3}}{\mu_{r1} \mu_{r3}} \cos(k_{x1} t_1) \cos k_{x3} (a-t_2) \sin k_{x2} (t_2-t_1) \\
& - \frac{k_{x2}^2}{\mu_{r2}^2} \sin(k_{x1} t_1) \sin k_{x3} (a-t_2) \sin k_{x2} (t_2-t_1) = 0
\end{aligned} \tag{4.5}$$

where $k_{xi} = k_0 \sqrt{\epsilon_{ri} \mu_{ri} - B^2}$; $i=1, 2, 3$; $k_0 = \omega \sqrt{\epsilon_0 \mu_0}$; $B = \beta_2 / k_0$. The mode index of the normalized eigenvalue B of the axial (z) component of the propagation factor is suppressed and the above eigenvalue equation can be solved for modal axial separation constant B .

For two-layer slab configuration denoting $t_1 = t_2 = t, k_{x2} = k_{x3}, \mu_{r2} = \mu_{r3}$, Equation (4.5) reduces to

$$\frac{k_{x1}}{\mu_{r1}} \cos(k_{x1} t) \sin k_{x2} (a-t) + \frac{k_{x2}}{\mu_{r2}} \sin(k_{x1} t) \cos k_{x2} (a-t) = 0 \tag{4.6}$$

It should be noted that although the form of Equation (4.6) is identical with that of the well-known eigenvalues equation for DPS-DPS stratification (Balanis, 2012). This is illusory since the negative permeability of the DNG introduces a sign change, which together with the dispersive nature of medium parameters results in drastically different characteristics for modal fields as will be evident in the following sections. For single slab configuration, i.e., for a waveguide completely filled with DNG material, using $t_1 = t_2 = a, k_{x1} = k_{x2} = k_{x3} = k_x, \mu_{r1} = \mu_{r2} = \mu_{r3}$ the eigenvalue equation in Equation (4.5) reduces to a form identical to that of the empty waveguide

$$\sin(k_x a) = 0 \tag{4.7}$$

In the following section, two-layer DNG slab problem illustrated in Figure 4.1b will be considered. Nondispersive medium (layer 1 with $\epsilon_{r1}, \mu_{r1} > 0$) will be assumed to be air, and dispersive DNG medium (layer 2 with $\epsilon_{r2}, \mu_{r2} < 0$) whose electric and magnetic parameters are modeled with a single pole Lorentz model given in Equation (2.19). We will further assume that a so called “perfect match” condition is obtained at a reference frequency f_s , i.e. $\epsilon_{r2}(f_s) = \mu_{r2}(f_s) = -1$. Although in most of the numerical calculations $\epsilon_{r2}(f)$ is taken equal to $\mu_{r2}(f)$ to display some salient features of the modes using minimum number of parameter values, effect of non-identical parameters are also presented. The normalized values of the two sets of parameters used in numerical calculations are listed in Table 4.1, where $\omega_{se,sm}$ denote reference frequencies, which in the lossless case yield $\epsilon_{r2}(\omega_{se}) = -1$ and $\mu_{r2}(\omega_{sm}) = -1$, respectively.

Table 4.1 Lorentz Model Parameters

Parameter	ω_{pe}	ω_{0e}	Γ_e	ω_{pm}	ω_{0m}	Γ_m
Scenario I	$\omega_{se} \sqrt{48} / 5$	$\omega_{se} / 5$	$0; \omega_{se} / 200$	$\omega_{sm} \sqrt{48} / 5$	$\omega_{sm} / 5$	$0; \omega_{sm} / 200$
Scenario II	$\omega_{se} \sqrt{48} / 5$	$\omega_{se} / 5$	$0; \omega_{se} / 200$	$\omega_{sm} 4 / 3$	$\omega_{sm} / 3$	$0; \omega_{sm} / 200$

The variation of the refractive index for Scenario I is given in Figure 4.3 for $f_s = 9$ GHz and 13 GHz. It has to be noted that the medium exhibits DNG behavior over the frequency band 7-12 GHz, which will generally be used in subsequent calculations.

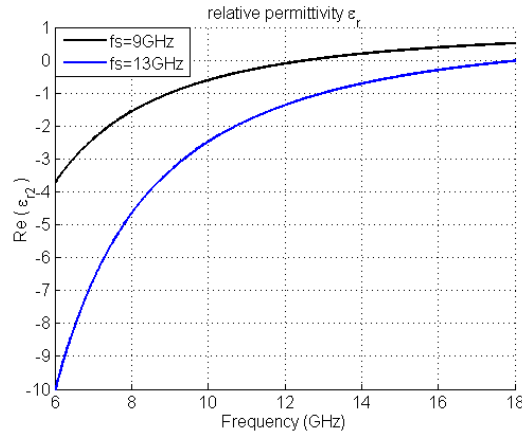


Figure 4.3 Real part of relative permittivity versus frequency which has refractive index about -1 for Scenario I at $f_s = 9$ GHz and $f_s = 13$ GHz.

4.3 Determination of Modal Cut-off Frequencies

At modal cut-off frequencies (f_c) defined by $\beta_2(f_c)=0$, we have $k_{x1} = \sqrt{k_0^2 \epsilon_{r1} \mu_{r1} - \beta_2^2} \Rightarrow k_0 \sqrt{\epsilon_{r1} \mu_{r1}}$ for $\epsilon_{r1}, \mu_{r1} > 0$ and $k_{x2} = \sqrt{k_0^2 \epsilon_{r2} \mu_{r2} - \beta_2^2} \Rightarrow k_0 \sqrt{\epsilon_{r2} \mu_{r2}}$ for $\epsilon_{r2}, \mu_{r2} < 0$. Noting that $k_{x2} / \mu_{r2} = -k_0 \sqrt{|\epsilon_{r2}| / |\mu_{r2}|}$, the eigenvalue equation given in Equation (4.6) reduces to Equation (4.8). Then, the solutions of Equation (4.8) for Scenario I of Table 4.1 is shown in Figure 4.4 for two reference frequencies (9 and 13 GHz). In the following figure, horizontal line (green) indicates the intersection of cut-off frequency curves with reference frequencies at different DNG slab thicknesses.

$$\sqrt{\frac{\epsilon_{r1}}{\mu_{r1}}} \cos(k_0 t) \sin\left(k_0 \sqrt{\epsilon_{r2} \mu_{r2}} (a-t)\right) - \sqrt{\frac{\epsilon_{r2}}{\mu_{r2}}} \sin(k_0 t) \cos\left(k_0 \sqrt{\epsilon_{r2} \mu_{r2}} (a-t)\right) = 0 \quad (4.8)$$

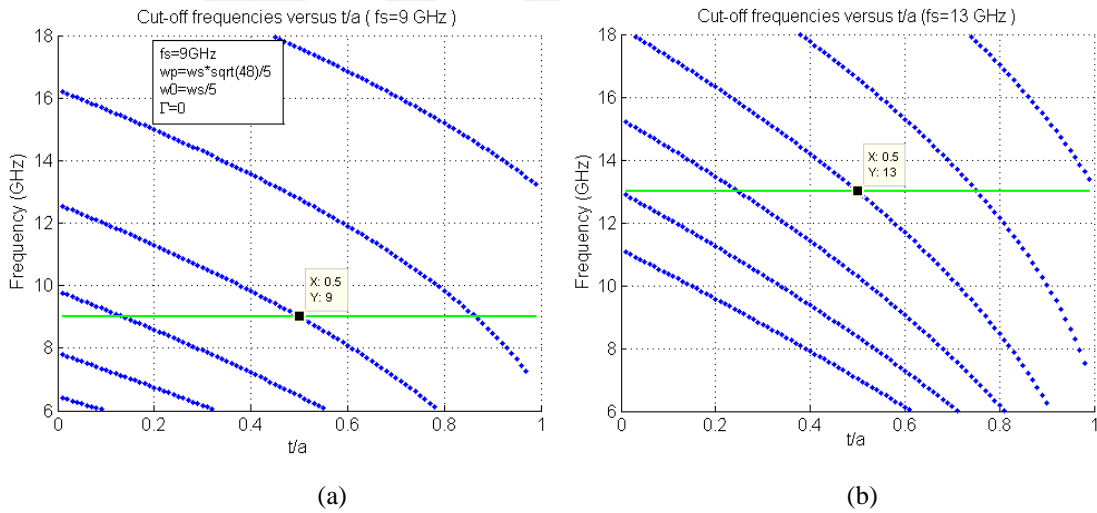


Figure 4.4 Variation of cut-off frequencies versus t/a for Scenario I where a) $f_{se}=f_{sm}=f_s=9$ GHz and b) $f_{se}=f_{sm}=f_s=13$ GHz (horizontal line).

4.4 Properties of Dispersion Diagrams

In this section properties of eigen solutions are investigated. Dispersion diagrams, phase and group velocities of propagating and evanescent modes (without/with loss) are plotted for different values of t (thickness of air region) and f_s , and the cut-off transitions are investigated in detail. Complex solutions of β are also presented which may exist for certain parameter values in lossless media.

4.4.1 Propagating and Evanescent Waves (Lossless and Lossy Cases)

Propagating and evanescent modes are calculated for Lorentz model DNG slab with identical ϵ_r and μ_r parameters where $\omega_{pe} = \omega_{pm} = \omega_p = \omega_s \sqrt{48/5}$, $\omega_{oe} = \omega_{om} = \omega_o = \omega_s/5$ and $\Gamma_e = \Gamma_m = \Gamma$. In this section, reference frequency (f_s) is chosen as 9 GHz, where a negative refractive index of about -1 is obtained. In Figure 4.5, dispersion graphs at various DNG slab thicknesses in the lossless case ($\Gamma=0$) are presented. Real and imaginary parts of β/k_0 are plotted in the same dispersion diagrams to facilitate displaying modal cut-off transitions between evanescent and propagating wave fields. Positive values are assigned to real, and negative values to imaginary values of β/k_0 , representing phase progression and decay of the modal fields in the increasing z direction. Effect of loss in propagating modes when $\Gamma=\omega_s/1000$ and $\Gamma=\omega_s/200$ are also illustrated in Figure 4.6 and Figure 4.7, at the frequency region smaller/greater than the reference frequency and around center frequency, respectively.

In a rectangular waveguide fully loaded with DNG slab, one obtains 2 cutoff frequencies in the specified frequency range lower than the cutoff frequency of DPS slab. The reason is that as the frequency decreases, the negative refraction index value of DNG slab increases which leads to higher orders of propagating modes. However, in the presence of a DPS slab the cutoff frequencies and assigned indices to propagating modes display an ascending order. One can easily see in Figure 4.5a that for a DNG slab, the cut-off frequency of 1st mode of the waveguide loaded with the DNG slab is greater than the 2nd mode. In Figure 4.5b, dispersion diagram versus frequency is plotted when the thickness of layer 1 (air) is taken as $t=a/4$. In this illustration, first two modes having modal cutoff frequencies at 8.26 GHz and 10.95GHz are in the negative refractive index region, and the 3rd cutoff ($f_{c3}=14.65$ GHz) is in the positive index region. Hence, 1st and 2nd propagating modes correspond to DNG/DPS stratification, whereas the 3rd propagating mode behaves as a mode of conventional DPS/DPS case. Similar features are obtained for $t=a/3$ and illustrated in Figure 4.5c. For this reason, the operating frequency band 7-12 GHz has been used in most calculations, wherein the refractive index has negative values independent of the DNG slab thickness. These two samples are given for the case where the DNG slab is thicker than air. In both cases propagating mode having modal cutoff frequency greater than the reference frequency exhibits surface wave mode characteristics.

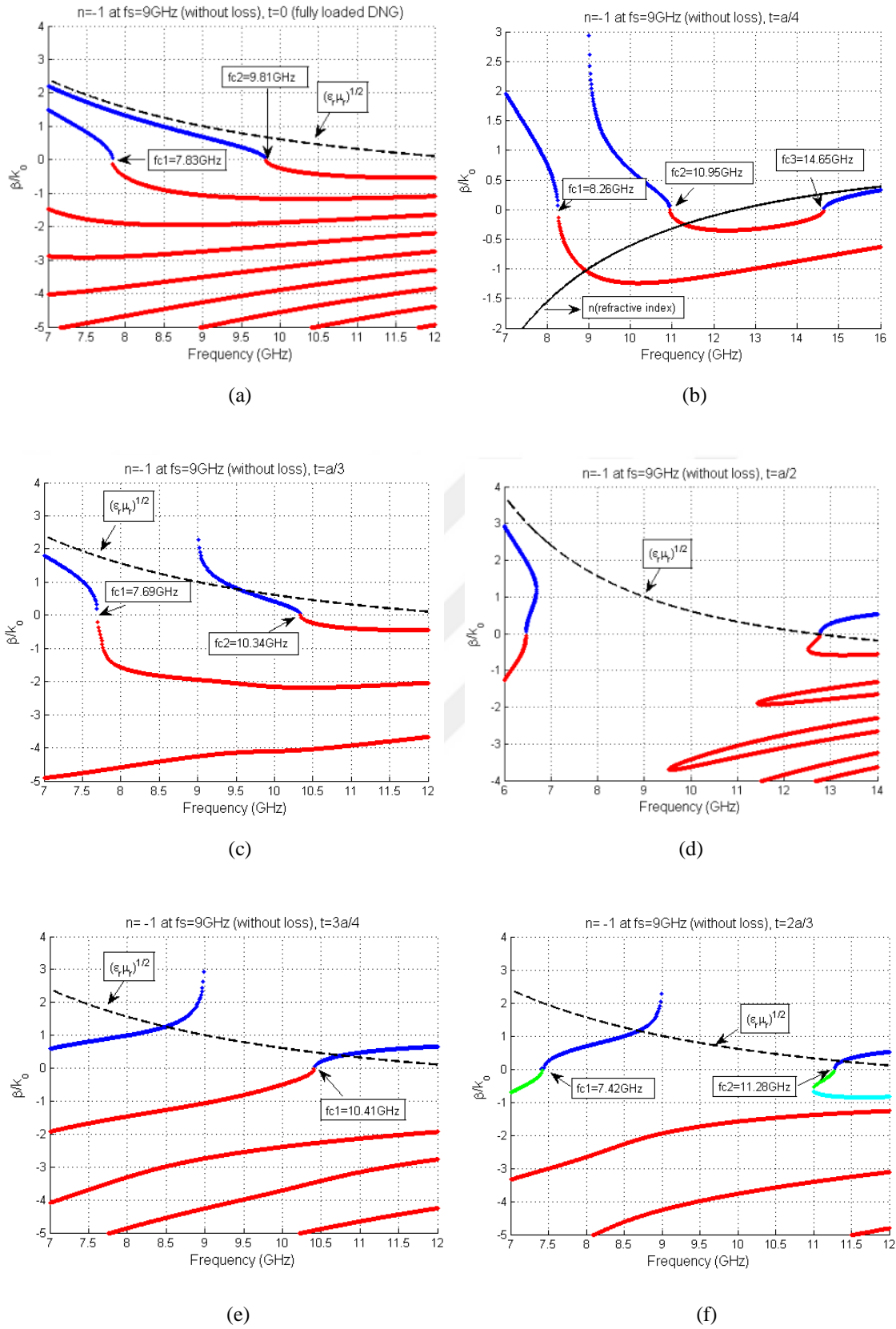


Figure 4.5 Dispersion diagrams of TE modes for a) fully loaded DNG slab ($t=0$) and partially loaded DNG slab when the thickness of air (t) is equals to b) $a/4$, c) $a/3$, d) $a/2$, e) $3a/4$ and f) $2a/3$

However, surface wave type modes will not be supported in the special case $t=a/2$ and propagating fields appear only for modes with cut-off frequencies away from f_s as indicated in Figure 4.5d. When the DNG slab thickness is chosen smaller than the air thickness, propagating modes (see in Figure 4.5e and Figure 4.5f) exhibit features as in DPS slab and surface wave type mode occurs for the first cutoff frequency smaller than the reference frequency. More details about surface wave type modes will be discussed in Section 4.4.4.

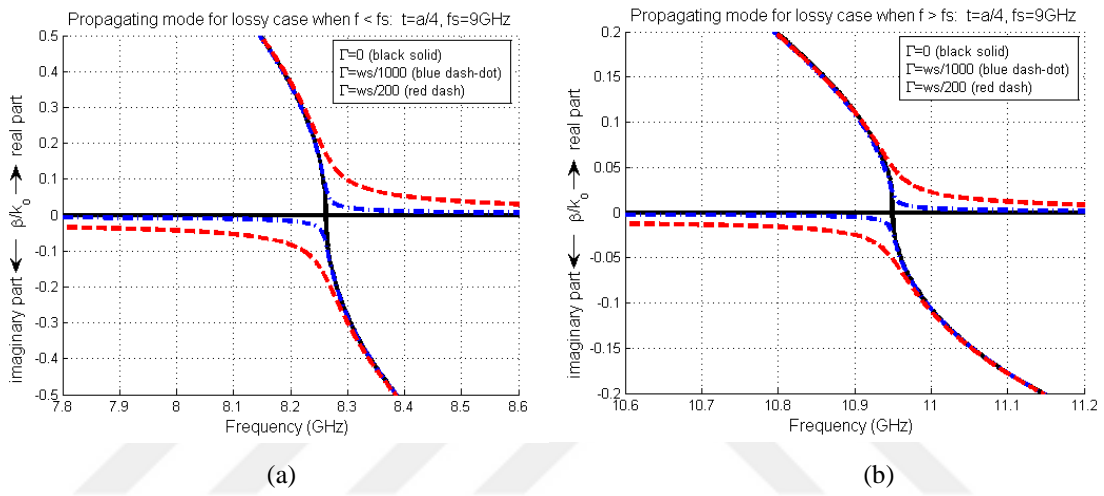


Figure 4.6 Dispersion diagrams of propagating modes in lossy case for (a) $f < f_s$, around $f_c=8.26\text{GHz}$ and (b) for $f > f_s$, around $f_c=10.95\text{GHz}$

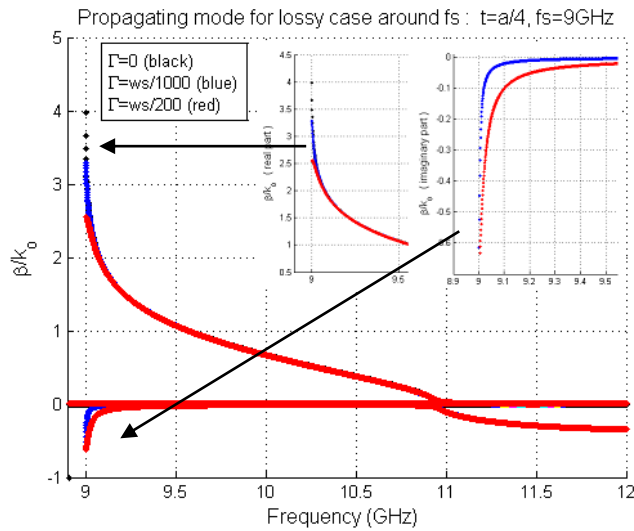


Figure 4.7 Dispersion diagrams of propagating modes in lossy case around f_s .

It as to be noted that the dispersion diagrams given for the lossless Lorenz model are only slightly modified by inclusion of small losses to the model. Indeed, the differences between dispersion diagrams are not discernable in the scale of the figures, except for the vicinities of cut-off transitions about 8.26GHz and 10.95GHz as shown in Figure 4.6a and Figure 4.6b, respectively. Figure 4.7 shows the effects of losses for the surface wave type mode which is supported around the reference frequency. Inspecting the presented numerical solutions, one is tempted to conclude that the value of β/k_0 is purely real or imaginary for lossless case, having complex values only when the damping factor (Γ) inserted to the electric and magnetic susceptibility functions. However, in some exceptional case, even if the medium is lossless eigenvalue equation has complex valued solutions for β/k_0 in certain parameter regions. Causes and consequences of this situation will be explained in details in the following section.

4.4.2 Complex eigenvalues in lossless case

The existence of complex eigenvalues in certain lossless waveguiding environments has been reported as early as 1965 (Clarricoats & Slinn, 1965) and has been an area of active research ever since, and there are numerous investigations in the literature, dealing with their properties and existence conditions (Rozzi et al., 1998). Numerical results for complex eigenvalues in metamaterial loaded waveguide is also presented (Cory & Shtrom, 2004), but under the assumption of frequency independent negative index materials. However, to the best of authors knowledge our approach is the first one which casts physical insight into the mechanism leading to emergence of complex eigenvalues in metamaterial loaded waveguides including dispersion effects, and provides a very convenient means for determining their originating points, thereby substantially facilitating their computation and elimination of spurious numerical artifacts. It is well known that, a single complex mode cannot exist, but two complex waves having complex conjugate propagation constants form a pair which as a whole behaves as an ordinary mode below cut-off carrying purely reactive power. Hence, complex modes may need to be taken into account in the characterization of discontinuities as they contribute in pairs with complex conjugate propagation constants to local power storage (Rozzi & Farina, 1999).

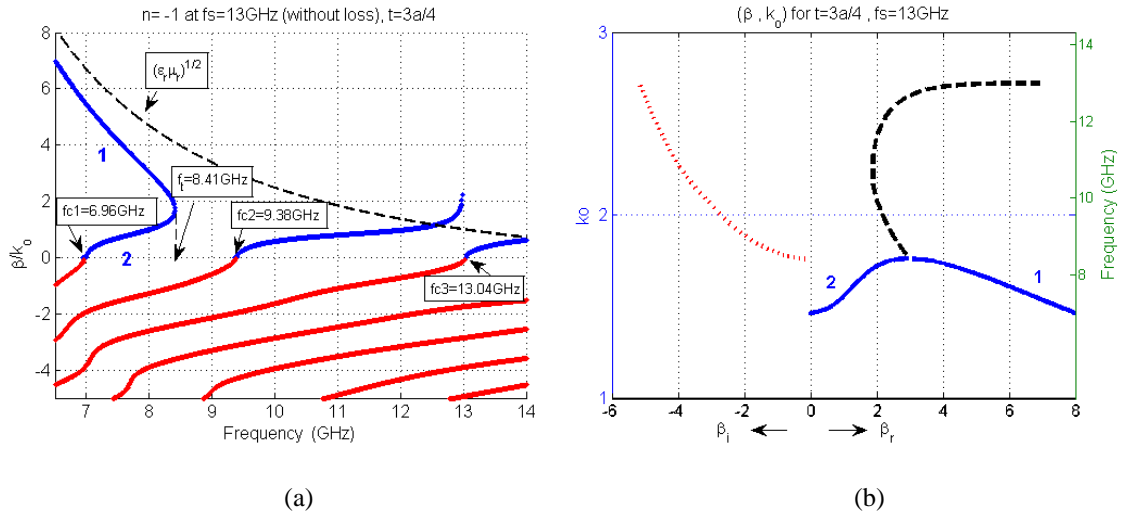


Figure 4.8 a) Propagating mode turns at a certain frequency which yields complex eigenvalues around that turning point, b) Real and imaginary parts of one of the complex β .

In Figure 4.8a, propagating and evanescent modes are presented for DNG slab with the parameters of Scenario I (see Table 4.1) as in previous section but for the case when the reference frequency which yields negative refractive index -1 is chosen at $f_s=13\text{GHz}$. It is clearly observed that if there are more than one propagating mode below the reference frequency, the mode with modal cutoff frequency near to reference frequency forms a surface wave type mode in a lossless medium whereas the one with the smallest cutoff frequency exhibits a distinctly different behavior. In Figure 4.8a, there exist two propagating wave solutions one of them being of the forward wave and the other backward wave type at all frequencies between the cutoff frequency (6.96 GHz) and the turning point frequency (8.41 GHz), beyond which both solutions disappear. That's why, particular attention should be paid to the behavior of the propagation coefficient at this point since the complex valued conjugate pairs of solutions for β emerge around that turning point. One of the complex conjugate pair is depicted in Figure 4.8b wherein the horizontal axis corresponds to real and imaginary part of beta, left vertical axis corresponds to k_0 , and right vertical axis corresponds to frequency.

Clearly, the frequency domain analysis in this chapter is applicable for any given data set for DNG constitutive parameters. To demonstrate this and provide a test case for assessing the accuracy of our codes, we have calculated the dispersion diagram given in (Cory & Shtrom, 2004), Figure 3 with the same parameters, i.e., $a=2.286\text{cm}$, $d=(a-t)=a/4$, $\epsilon_{r1}=\mu_{r1}=1$, $\epsilon_{r2}=-9$, $\mu_{r2}=-1$. Thus, for calculation of the values plotted in Figure 4.9 the DNG

slab is modelled as non-dispersive, lossless medium. Comparing our results depicted in Figure 4.9 with Figure 3 of (Cory & Shtrom, 2004), one observes that the dispersion curves of both propagating and complex modes are in perfect agreement over the frequency range considered, $k_0 d \in 0.3-3$, $f \in 2.5-25$ GHz.

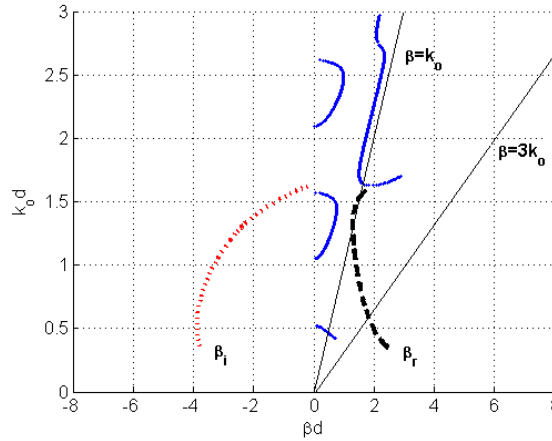


Figure 4.9 Dispersion diagram calculated with parameters (see text) given in (Cory & Shtrom, 2004): Propagating (blue solid) and one of the complex waves: real part (black dash) and imaginary part (red dot).

4.4.3 Phase and Group Velocities

The general description of phase velocity (v_p) and group velocity (v_g) in an unbounded non-dispersive medium is mentioned in Section 2.5. In a finite dispersive medium, dispersion diagrams provide a convenient means for visually assessing the dependence of phase velocity on frequency, the relative value of phase velocity at any frequency is just the inverse of the value read from the dispersion curve, $v_p / c = 1 / (\beta / k_0)$.

We begin by writing the eigenvalue equation in Equation (4.6) as,

$$F(\beta, \omega) = \frac{k_1}{\mu_{r1}} \cot(k_1 t) + \frac{k_2}{\mu_{r2}} \cot(k_2 d) = 0 \quad (4.9)$$

where $d = a - t$, $k_0 = \omega / c$ and $k_i = \sqrt{k_0^2 \epsilon_{ri} \mu_{ri} - \beta^2}$; $i = 1, 2$. The group velocity can be calculated in a straightforward manner (Eleftheriades, Iyer, & Kremer, 2002) as outlined below:

$$dF=0=\frac{\partial F}{\partial \beta}d\beta+\frac{\partial F}{\partial \omega}d\omega \Rightarrow v_g=\frac{d\omega}{d\beta}=-\frac{\partial F/\partial \beta}{\partial F/\partial \omega} \quad (4.10)$$

In the following we will assume that medium 1 is non-dispersive (i.e., ϵ_1, μ_1 are constants; $\epsilon_{r1}=\mu_{r1}=1$) and medium 2 is DNG, characterized by single pole Lorentz model with identical electric and magnetic parameters: $(\epsilon_2, \mu_2)=(\epsilon_0, \mu_0) \left\{ 1 + \frac{\omega_p^2}{\omega_0^2 - \omega^2 + j\Gamma\omega} \right\}$ with constant ω_p, ω_0 and Γ , and the latter will be assumed to be zero at this point (i.e., lossless DNG). We then have the following solutions for Equation (4.10) to obtain the group velocity at desired frequency.

$$\frac{\partial k_{1,2}}{\partial \beta} = -\frac{\beta}{k_{1,2}}; \quad \frac{\partial k_1}{\partial \omega} = \frac{\omega}{k_1 c^2}; \quad \frac{\partial k_2}{\partial \omega} = \frac{\omega \epsilon_{r2}^2 + \omega^2 \epsilon_{r2} \frac{\partial \epsilon_{r2}}{\partial \omega}}{k_2 c^2}; \quad \frac{\partial \epsilon_{r2}}{\partial \omega} = \frac{2\omega \omega_p^2}{(\omega_0^2 - \omega^2)^2} \quad (4.11a)$$

$$\frac{\partial F}{\partial \beta} = -\frac{\beta}{k_1} \left\{ \cot(k_1 t) - \frac{k_1 t}{\sin^2(k_1 t)} \right\} - \frac{\beta}{\mu_{r2} k_2} \left\{ \cot(k_2 d) - \frac{k_2 d}{\sin^2(k_2 d)} \right\} \quad (4.11b)$$

$$\begin{aligned} \frac{\partial F}{\partial \omega} = \frac{\omega}{k_1 c^2} \left\{ \cot(k_1 t) - \frac{k_1 t}{\sin^2(k_1 t)} \right\} - \frac{\omega \epsilon_{r2}^2}{\mu_{r2} k_2 c^2} \left(1 + \frac{2\omega^2}{\omega_0^2 - \omega^2} \right) \frac{k_2 d}{\sin^2(k_2 d)} \\ + \frac{\omega}{\mu_{r2} k_2 c^2} \cot(k_2 d) \left\{ \epsilon_{r2}^2 \left(1 + \frac{2\omega^2}{\omega_0^2 - \omega^2} \right) - \frac{2k_2^2 c^2}{(\omega_0^2 - \omega^2)} \right\} \end{aligned} \quad (4.11c)$$

In the following, dispersion diagrams in (β, k_0) axes are given for DNG slab with a ratio of t/a equals to 0 (fully loaded), 1/4 and 3/4. Identical permittivity and permeability parameters that yield $n=-1$ at $f_s=9$ GHz are used, and no loss is considered. The plots of dispersion diagrams given in Figures 4.10a, 4.10b and 4.10c can be used for visually assessing the dependence of group velocity on frequency where the slope of the curve at any point is equal to the value of relative group velocity at the corresponding frequency, $dk_0/d\beta = v_g/c$. When the rectangular waveguide is fully loaded with DNG slab, the group and phase velocities illustrated in Figure 4.10d, are in opposite directions for both

modes over the plotted frequency ranges of propagation. This behavior, typical in DNG media, is denoted as “contra-directional” flow as opposed to “co-directional” flow typical in DPS media, where phase and group velocities are in the same directions (Veselago et al., 2006). Similarly, from Figure 4.10e, we immediately infer that for $t=a/4$ wherein the layer 2 (DNG slab) is thicker than layer 1 (air), phase and group velocities are in opposite directions. However, if the thickness of DNG slab is smaller than the air region ($t=3a/4$), the results given in Figure 4.10f clearly show that in this case phase and group velocities are in same directions which indicates that the propagating modes exhibit a forward wave behavior similar to propagation in DPS media.

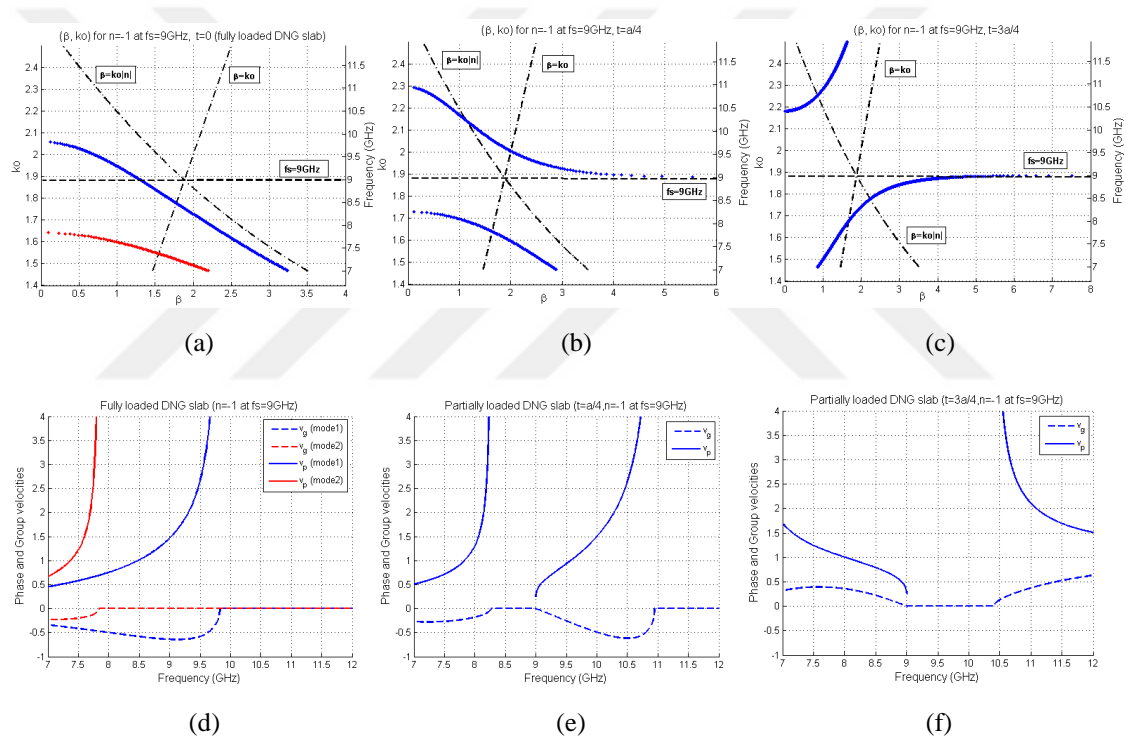


Figure 4.10 Dispersion diagram and phase/group velocities in a rectangular waveguide loaded with DNG slab with a ratio of $t/a=0, 1/4$ and $3/4$.

Co-directional - contra-directional flow transitions are presented in Figure 4.11. Same data for propagating modes given in Figure 4.11a is used and phase/group velocities are plotted in Figure 4.11b. As shown in the figure there is a modal cutoff frequency at about 6.96 GHz, where the phase velocity goes to infinity ($v_p \rightarrow \infty$) and the group velocity goes to zero ($v_g \rightarrow 0$) as expected. However, since there are two solutions at all

frequencies between 6.96 GHz and 8.41 GHz, group and phase velocities exhibits different characteristics for both branches such as co-directional (2nd branch) for one, and contra-directional (1st branch) for the other. Moreover, group velocities for both branches passes through zero at the turning point, while the phase velocity has a finite value. This can be regarded as a non-conventional cut-off frequency. Clearly, we expect that the dominant part of the transmitted power resides in the DPS (air) medium for co-directional case and in the DNG medium for contra-directional case. This is demonstrated in Figure 4.11c where the variation of the modal field E_y for the two solutions is plotted at 7.5 GHz.

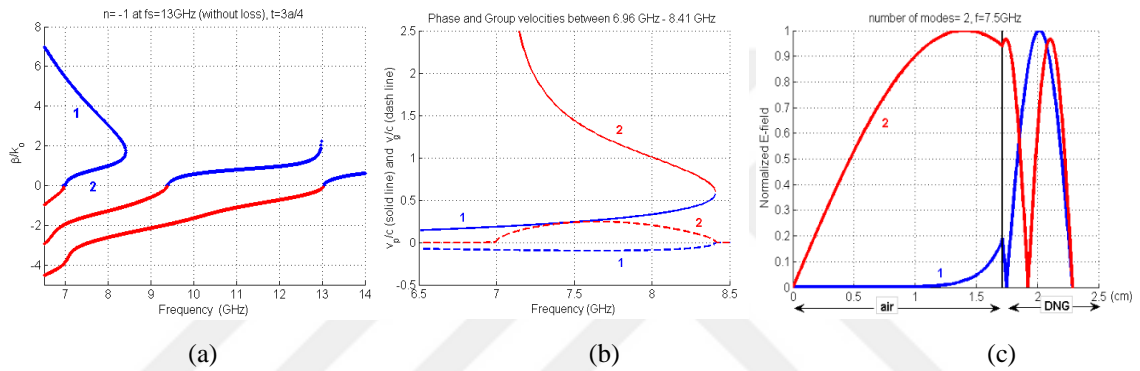


Figure 4.11 (a) Propagating mode turns at a certain frequency (b) group /phase velocities for complex β solutions and (c) E-field distribution along x-axis where DNG slab has $n=-1$ at $f_s=13\text{GHz}$ and $t=3a/4$.

4.4.4 Surface Wave Type Solutions

Wave fields which “cling” to a surface, i.e. decay exponentially as one moves away from the surface, while propagating without loss (in case material losses are omitted) are called surface waves. Clearly, such solutions can exist only in parameter regions wherein one has solutions characterized by real values of β , together with imaginary values of both k_1 and k_2 (Kalluri, 2012; Davidson, 2011). This leads to the condition,

$$b = \frac{\beta}{k_0} > \max(\epsilon_{r1}\mu_{r1}, \epsilon_{r2}\mu_{r2}) \quad (4.12)$$

Defining imaginary values of k_1 and k_2 as,

$$\bar{k}_1 = k_0 \sqrt{b^2 - \varepsilon_{r1} \mu_{r1}} \quad \bar{k}_2 = k_0 \sqrt{b^2 - \varepsilon_{r2} \mu_{r2}} \quad (4.13)$$

The eigenvalue equation reduces to

$$\bar{k}_1 t = \tanh^{-1} \left[A \tanh(\bar{k}_2 d) \right] \quad \text{where} \quad A = \frac{|\mu_{r2}|}{\mu_{r1}} \frac{\bar{k}_1}{\bar{k}_2} \quad \text{and} \quad d = a - t \quad (4.14)$$

At this point we would like to introduce the assumption that the dielectric and magnetic parameters of the DNG media satisfy $\varepsilon_{r2}(f_s) = \mu_{r2}(f_s) = -1$ at the common “reference frequency” f_s . We further assume DPS medium is air, i.e., $\varepsilon_{r1}(f) = \mu_{r1}(f) = 1$. One can then conclude that for satisfaction of the condition in Equation (4.12) the frequency has to be in the vicinity f_s . Let us denote the cutoff frequency of the propagating mode which in a certain frequency range exhibits surface wave behavior as f_c and consider the two possible cases separately in the vicinity f_s :

$f_s > f_c$: In this frequency range we have as $f \rightarrow f_s$, $|\mu_{r2}(f)| > \mu_{r1}$; $\bar{k}_2 < \bar{k}_1$ and $A > 1$. Hence, Equation (4.14) has a solution only if $d < t$. Hence the mode will exhibit surface wave behavior in the frequency range $f_0 - f_s$ where $\bar{k}_1(f_0) = 0$.

$f_s < f_c$: In this frequency range we have as $f \rightarrow f_s$, $|\mu_{r2}(f)| < \mu_{r1}$; $\bar{k}_2 > \bar{k}_1$ and $A < 1$. Hence, Equation (4.14) has a solution only if $d > t$. Hence the mode will exhibit surface wave behavior in the frequency range $f_0 - f_s$ where $\bar{k}_2(f_0) = 0$.

The conditions for the existence of surface wave type solutions in the partially loaded waveguide can be summarized as:

1. In the frequency range considered the two media should be of the types DPS – DNG, and f has to be in the vicinity of f_s .
2. If $f_s > f_c$ then the condition $d < t$ has to be satisfied.
3. If $f_s < f_c$ then the condition $d > t$ has to be satisfied.

The presence of much larger fields along the DNG-air interface, characterizing surface waves for identical parameters clearly seen in Figure 4.12. Surface wave type modes are also presented in Figure 4.13 for lossless DNG slab with non-identical parameters when the t/a ratio is equal to $1/4$ and $3/4$, respectively.

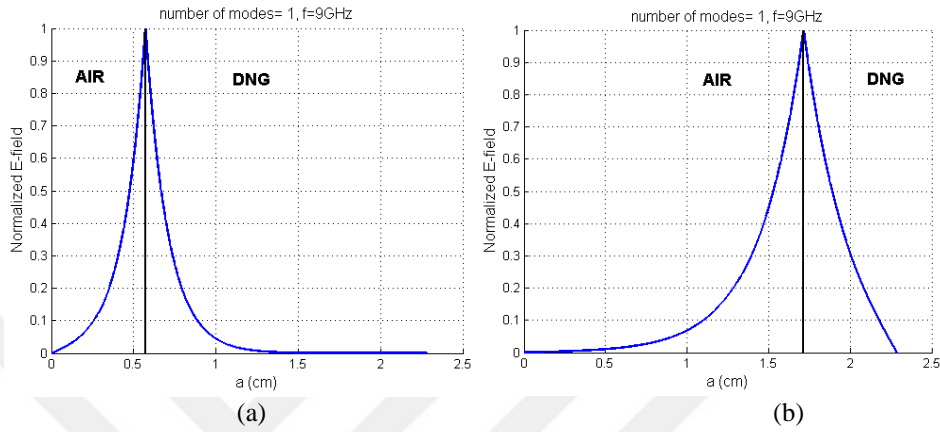


Figure 4.12 Surface waves along DNG-air interface along x-axis for (a) $t=a/4$ and (b) $t=3a/4$ where DNG slab has negative refractive index about -1 at $f_s=9\text{GHz}$.

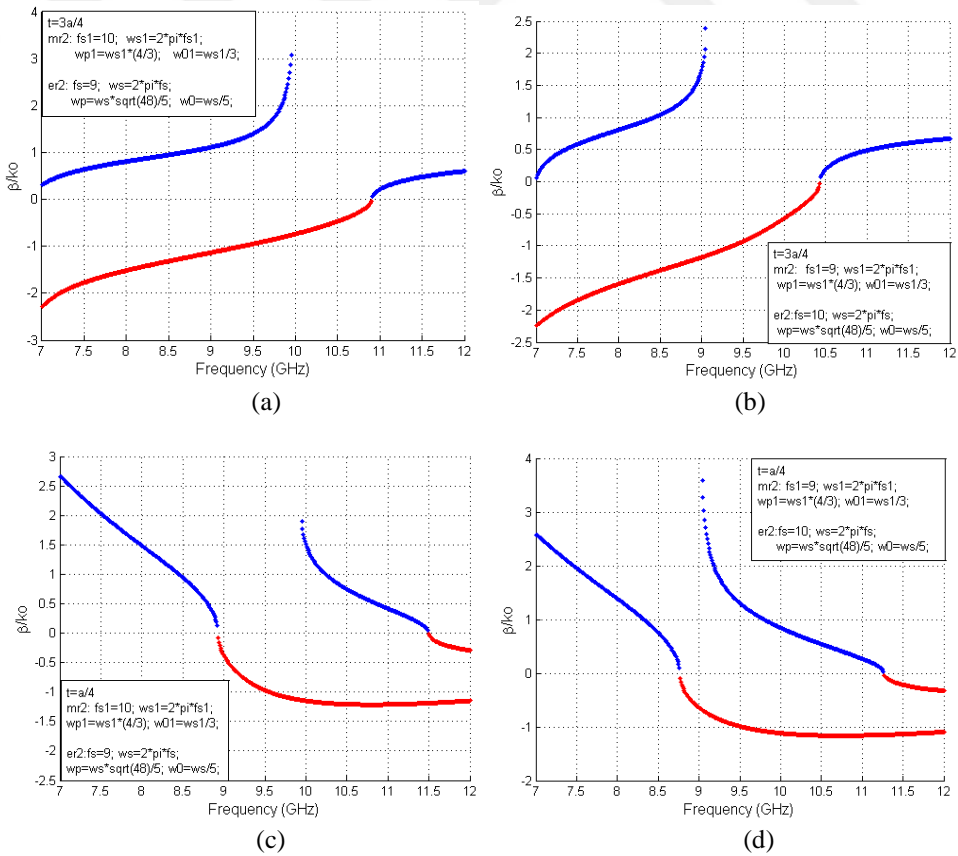


Figure 4.13 Dispersion diagrams of propagating modes for non-identical parameters when $t=a/4$ and $3a/4$.

As seen in Figure 4.13 and Figure 4.14, propagation constant of surface modes increases asymptotically at f_s when DNG medium has identical electric and magnetic parameters, whereas when the parameters are non-identical the asymptote shifts to the immediate vicinity of the frequency where the relative permeability equals to -1.

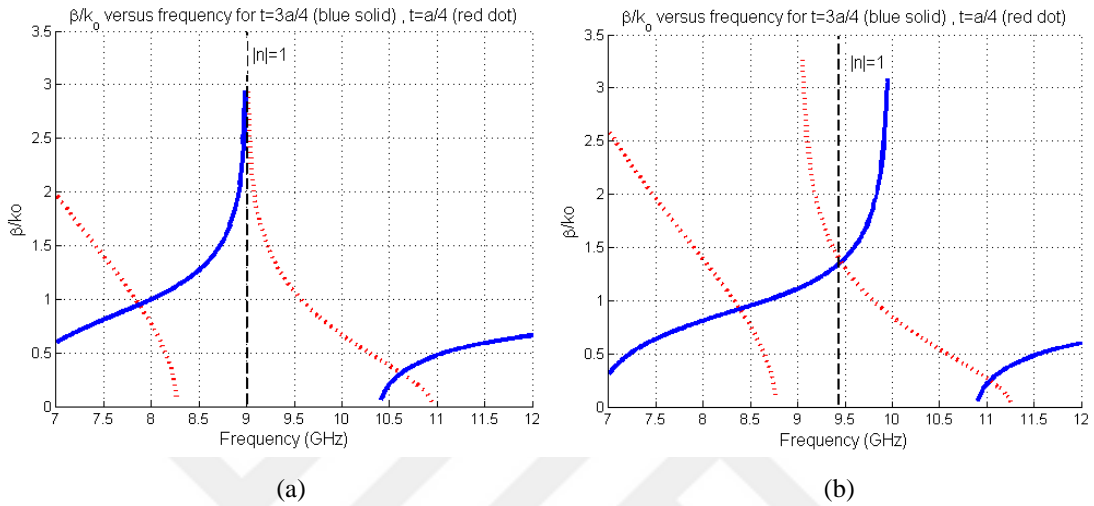


Figure 4.14 Dispersion diagrams of propagating modes for Scenario I and II

(a) lossless identical parameters given in Scenario I: $f_{se} = f_{sm} = f_s = 9 \text{ GHz}$ where $n = -1$ at $f = 9 \text{ GHz}$, (b) lossless non-identical parameters given in Scenario II: blue solid for $f_{se} = 9 \text{ GHz}$, $f_{sm} = 10 \text{ GHz}$ and red dot for $f_{se} = 10 \text{ GHz}$, $f_{sm} = 9 \text{ GHz}$ where $n = -1$ at about $f = 9.45 \text{ GHz}$. Refractive indices (n) are indicated with vertical dashed line.

4.5 Mode Matching Solution of Scattering from Partially Loaded Sections

In this section we investigate reflection and transmission characteristics of the structure shown in Figure 4.1b. Following assumptions are made:

- i- TE_{10} mode is incident from the left of the loaded section and geometry is invariant along y .
- ii- Waveguide is match terminated on the right of the loaded section.
- iii- $e^{j\omega t}$ time dependence is assumed and suppressed.

Under these simplifying assumptions, analytic solutions in the spectral domain can conveniently be obtained using a mode matching approach involving the modes of the loaded section obtained in previous section. This technique is usually applied to the analysis of waveguide structures with various discontinuities in many applications for

decades (Wexler, 1967; Wessel, Sieverding, & Arndt, 1999; Balaji & Vahldieck, 1998; Chan & Judah, 1998; Schmidt & Russer, 1995). The fields on both sides of the discontinuity are described by a superposition of waveguide modes, and then the appropriate continuity conditions are imposed at the interface to yield a system of equations (Golio & Golio, 2008; Helszajn, 2000). The modal expressions for transverse field components (E_y and H_x) in Region I, II and III (see Figure 4.1b) can be written as:

$z < 0$ (Region I): dominant mode is propagating along z -direction

$$E_y^I = \bar{f}_1 e^{-jk_1^I z} + R \bar{f}_1 e^{jk_1^I z} + \sum_{n=2}^N B_n^I \bar{f}_n e^{jk_n^I z} \quad (4.15a)$$

$$H_x^I = -\frac{k_1^I}{\omega \mu_o} \bar{f}_1 e^{-jk_1^I z} + R \frac{k_1^I}{\omega \mu_o} \bar{f}_1 e^{jk_1^I z} + \sum_{n=2}^N \frac{k_n^I}{\omega \mu_o} B_n^I \bar{f}_n e^{jk_n^I z} \quad (4.15b)$$

where

$$k_n^I = \beta_{1,n} = \sqrt{k_o^2 - \left(\frac{n\pi}{a}\right)^2}; Y_n^I = \frac{\beta_{1,n}}{\omega \mu_o}; \beta_{1,1} = \sqrt{k_o^2 - \left(\frac{\pi}{a}\right)^2} \quad (4.16)$$

$$\bar{f}_n = \sqrt{\frac{2}{a}} \sin\left(\frac{n\pi x}{a}\right) \Rightarrow \int_0^a \bar{f}_n \bar{f}_m dx = \begin{cases} \delta_{n,m} & ; n=m \\ 0 & ; n \neq m \end{cases}$$

$z \in 0, d$ (Region II): including DNG slab

$$E_{y1}^{II} = \sum_{n=1}^N B_n^{II} f_{1,n} e^{jk_n^{II} z} + \sum_{n=1}^N F_n^{II} f_{1,n} e^{-jk_n^{II} z} \quad \text{for } 0 < x < t \quad (4.17a)$$

$$H_{x1}^{II} = \sum_{n=1}^N \frac{k_n^{II}}{\omega \mu_o} B_n^{II} f_{1,n} e^{jk_n^{II} z} - \sum_{n=1}^N \frac{k_n^{II}}{\omega \mu_o} F_n^{II} f_{1,n} e^{-jk_n^{II} z} \quad \text{for } 0 < x < t \quad (4.17b)$$

$$E_{y2}^{II} = \sum_{n=1}^N B_n^{II} f_{2,n} e^{jk_n^{II} z} + \sum_{n=1}^N F_n^{II} f_{2,n} e^{-jk_n^{II} z} \quad \text{for } t < x < a \quad (4.18a)$$

$$H_{x2}^{II} = \sum_{n=1}^N \frac{k_n^{II}}{\omega \mu_o \mu_{r2}} B_n^{II} f_{2,n} e^{jk_n^{II} z} - \sum_{n=1}^N \frac{k_n^{II}}{\omega \mu_o \mu_{r2}} F_n^{II} f_{2,n} e^{-jk_n^{II} z} \quad \text{for } t < x < a \quad (4.18b)$$

where

$$k_n^{II} = \beta_{2,n} = \begin{cases} Y_{1,n}^{II} = \frac{\beta_{2,n}}{\omega \mu_o}; \beta_{2,n} = \sqrt{k_o^2 - k_{1,n}^2} & \text{where } k_{1,n} = k_o \sqrt{1 - \left(\frac{\beta_{2,n}}{k_o}\right)^2}; 0 < x < t \\ Y_{2,n}^{II} = \frac{\beta_{2,n}}{\omega \mu_o \mu_{r2}}; \beta_{2,n} = \sqrt{k_o^2 \epsilon_{r2} \mu_{r2} - k_{2,n}^2} & \text{where } k_{2,n} = k_o \sqrt{\epsilon_{r2} \mu_{r2} - \left(\frac{\beta_{2,n}}{k_o}\right)^2}; t < x < a \end{cases} \quad (4.19)$$

$$f_{1,n} = A_n \sin(k_{1,n} x); f_{2,n} = A_n C_n \sin(k_{2,n} (a-x)); C_n = \sin(k_{1,n} t) / \sin(k_{2,n} (a-t))$$

$z > d$ (Region III): only first dominant mode is transmitted, and the other modes are evanescent.

$$E_y^{III} = \sum_{n=1}^N F_n^{III} \bar{f}_n e^{-jk_n^{III} (z-d)} \quad (4.20a)$$

$$H_x^{III} = - \sum_{n=1}^N \frac{k_n^{III}}{\omega \mu_o} F_n^{III} \bar{f}_n e^{-jk_n^{III} (z-d)} \quad (4.20b)$$

where

$$k_n^{III} = \beta_{1,n} = \sqrt{k_o^2 - \left(\frac{n\pi}{a}\right)^2}; Y_n^{III} = \frac{\beta_{1,n}}{\omega \mu_o} \quad (4.21)$$

Applying boundary conditions and making some mathematical manipulations we obtain the following matrix equation:

$$\begin{aligned} U &= QP - SR \\ 0 &= QR - SP \end{aligned} \quad (4.22)$$

Here,

U is Nx1 column vector $U_\nu = 2Y_1' \langle W_\nu, \bar{f}_1 \rangle$,

P and R are Nx1 column vectors of the expansion coefficient p_ν, r_ν where $\nu=1, \dots, N$,

Q is NxN matrix with elements $Q_{k,\nu} = \sum_{n=1}^N Y_n' \langle W_\nu, \bar{f}_n \rangle \langle W_k, \bar{f}_n \rangle - j \cot(k_k'' d) \langle W_\nu, G_k \rangle$ for $Y_n' = Y_n'''$,

S is NxN diagonal matrix with elements $S_{k,\nu} = \frac{\langle W_\nu, G_k \rangle}{j \sin(k_k'' d)}$,

with

$$\langle W_k, \bar{f}_n \rangle = \int_0^t f_{1,k} \bar{f}_n dx + \int_t^a f_{2,k} \bar{f}_n dx = J_1 + J_2 \quad (4.23a)$$

$$\langle W_\nu, G_k \rangle = \int_0^t f_{1,\nu} \cdot g_{1,k} dx + \int_t^a f_{2,\nu} \cdot g_{2,k} dx = A_k^2 \frac{k_k''}{\omega \mu_o} \left\{ I_1 + \frac{1}{\mu_{r2}} C_k^2 I_2 \right\} = \begin{cases} a_k, & \text{if } \nu=k \\ 0, & \text{if } \nu \neq k \end{cases} \quad (4.23b)$$

where

$$f_{1,k} = A_k \sin(k_{1,k} x); f_{2,k} = A_k C_k \sin(k_{2,k} (a-x)); \bar{f}_n = \sqrt{\frac{2}{a}} \sin\left(\frac{n\pi}{a} x\right); \zeta_n = \frac{n\pi}{a} \quad (4.24)$$

$$W_\nu(x) = \begin{cases} f_{1,\nu} = A_\nu \sin(k_{1,\nu} x) & , x \in 0, t \\ f_{2,\nu} = A_\nu C_\nu \sin(k_{2,\nu} (a-x)) & , x \in t, a \end{cases} \quad \text{with } C_\nu = \frac{\sin(k_{1,\nu} t)}{\sin(k_{2,\nu} (a-t))} \quad (4.25)$$

$$G_k(x) = \begin{cases} g_{1,k} = Y_{1,k}'' f_{1,k} & \text{where } Y_{1,k}'' = k_k'' / \omega \mu_o, x \in 0, t \\ g_{2,k} = Y_{2,k}'' f_{2,k} & \text{where } Y_{2,k}'' = k_k'' / \omega \mu_o \mu_{r2}, x \in t, a \end{cases}$$

$$\begin{aligned}
J_1 &= \sqrt{\frac{2}{a}} \frac{A_k}{k_{1,k}^2 - \zeta_n^2} \{ \zeta_n \sin(k_{1,k}t) \cos(\zeta_n t) - k_{1,k} \sin(\zeta_n t) \cos(k_{1,k}t) \} \\
J_2 &= \sqrt{\frac{2}{a}} \frac{A_k C_k}{\zeta_n^2 - k_{2,k}^2} \{ \zeta_n \sin(k_{2,k}(a-t)) \cos(\zeta_n t) + k_{2,k} \sin(\zeta_n t) \cos(k_{2,k}(a-t)) \} \\
I_1 &= \int_0^t (\sin(k_{1,k}x))^2 dx = \frac{1}{2} \left[t - \frac{1}{2k_{1,k}} \sin(2k_{1,k}t) \right] \\
I_2 &= \int_t^a (\sin(k_{2,k}(a-x)))^2 dx = \frac{1}{2} \left[a-t - \frac{1}{2k_{2,k}} \sin(2k_{2,k}(a-t)) \right]
\end{aligned} \tag{4.26}$$

Then the solution of Equation (4.22) yields the column vectors of R and P which are used to calculate the reflection and transmission coefficients as in Equation (4.28):

$$\begin{aligned}
0 &= QR - SP \Rightarrow QR = SP \Rightarrow R = Q^{-1}SP \\
U &= QP - SR \Rightarrow U = (Q - SQ^{-1}S)P \Rightarrow P = (Q - SQ^{-1}S)^{-1}U
\end{aligned} \tag{4.27}$$

$$S_{11} = \sum_{k=1}^N p_k \langle W_k, \bar{f}_1 \rangle - 1 \quad \text{and} \quad S_{21} = \sum_{k=1}^N r_k \langle W_k, \bar{f}_1 \rangle \tag{4.28}$$

4.6 Scattering Characteristics of Fully Loaded Sections

In this case the incident TE₁₀ mode meets all boundary conditions in x, hence also the loaded waveguide will be mono-modal, and we only need to impose the additional conditions in z, on z=0 and on z=d ports. Clearly, the problem depicted as in Figure 4.1c may then be thought to reduce to a transmission line discontinuity.

The x-dependent part of the propagation factor (k_x) and the modal function f(x)=sin(πx/a) are common in all regions. Thus, we can suppress the x dependence and write the transverse field components in all region as:

$$E_y = \begin{cases} E_{inc} (e^{-j\beta_1 z} + R e^{j\beta_1 z}) & z \leq 0 \\ A e^{-j\beta_2 z} + B e^{j\beta_2 z} & 0 \leq z \leq d \\ T e^{-j\beta_1 (z-d)} & z \geq d \end{cases} \quad (4.29)$$

$$H_x = -\frac{j}{\omega\mu} \frac{\partial E_y}{\partial z} = \begin{cases} -\frac{\beta_1}{\omega\mu_1} E_{inc} (e^{-j\beta_1 z} - R e^{j\beta_1 z}) & z \leq 0 \\ -\frac{\beta_2}{\omega\mu_2} (A e^{-j\beta_2 z} - B e^{j\beta_2 z}) & 0 \leq z \leq d \\ -\frac{\beta_1}{\omega\mu_1} T e^{-j\beta_1 (z-d)} & z \geq d \end{cases} \quad (4.30)$$

where R and T are used to represent, respectively, the reflection and transmission coefficients at the interface in lossless case. The losses in DPS/DNG medium are negligible one should have $|R|^2 + |T|^2 = 1$ and using continuity of E_y and H_x on $z=0, d$ surfaces which are the free-space/slab interfaces (with the normalization $E_{inc}=1$), we obtain

$$z = 0 \Rightarrow \begin{cases} 1 + R = A + B \\ 1 - R = \frac{1}{\xi} (A - B) \end{cases} \quad \text{with } \xi = \frac{Z_{TE}^{II}}{Z_{TE}^I} = \frac{|\mu_{r2}| \sqrt{1 - (\lambda/2a)^2}}{\sqrt{\epsilon_{r2} \mu_{r2} - (\lambda/2a)^2}} \quad (4.31a)$$

$$z = d \Rightarrow \begin{cases} A\tau + B \frac{1}{\tau} = T \\ \frac{1}{\xi} \left(A\tau - B \frac{1}{\tau} \right) = T \end{cases} \quad \text{with } \tau = \exp(-j\beta_2 d) \quad (4.31b)$$

Through straightforward elimination one then obtains:

$$R = -j \frac{2\Gamma e^{-j\beta_2 d} \sin \beta_2 d}{1 - \Gamma^2 e^{-j2\beta_2 d}} ; T = \frac{(1 - \Gamma^2) e^{-j\beta_2 d}}{1 - \Gamma^2 e^{-j2\beta_2 d}} \quad (4.32)$$

where

$$\Gamma = \frac{1-\xi}{1+\xi} = \frac{Z_{TE}^I - Z_{TE}^{II}}{Z_{TE}^I + Z_{TE}^{II}}; \quad Z_{TE}^I = \frac{\omega\mu_1}{\beta_1} = \frac{\eta_o\mu_{r1}}{\sqrt{\varepsilon_{r1}\mu_{r1} - (\lambda_o/2a)^2}}; \quad Z_{TE}^{II} = \frac{\omega\mu_2}{\beta_2} = \frac{\eta_o|\mu_{r2}|}{\sqrt{\varepsilon_{r2}\mu_{r2} - (\lambda_o/2a)^2}} \quad (4.33)$$

R and T are reflection and transmission coefficients referred to planes $z=z_1=0$ and $z=z_2=d$, respectively. When reference planes are shifted by L towards left (for R) and right (for T) we have $R \rightarrow R e^{-j2\beta_1 L}$; $T \rightarrow T e^{-j\beta_1 L}$. For the special case where $\chi_e = \chi_m$, impedance matching occurs ($Z_{TE}^{II} \rightarrow Z_{TE}^I$) at $f=f_s$ and $\Gamma \rightarrow 0$. Then the total input reflection and transmission coefficients reduce to $R \rightarrow 0$; $T = e^{-j\beta_2 d}$. In problems wherein waveguide sections on both sides of the discontinuity are identical (same cross-section, same dielectric, i.e. identical TE₁₀ mode impedances) and if the discontinuity region has a symmetry plane, then the scattering matrix can be written in terms of reflection (R) and transmission (T) as, $S = \begin{bmatrix} R & T \\ T & -R \end{bmatrix}$. However, in DNG loaded waveguide problems scattering matrix is quite different from DPS loaded problems. Relation between S-parameters are defined for two-port circuits fully loaded with DPS/DNG slab are given in Appendix C (Şimşek, Işık, & Topuz, 2011).

4.7 Numerical Results for Reflection-Transmission Characteristics

In this section an X-band (7–12 GHz) rectangular waveguide with dimensions $a=2.286$ cm and $b=1.016$ cm is fully loaded along x-direction with Lorentz model DNG medium as shown in Figure 4.1c. In Figure 4.15, reflection and transmission coefficients are calculated using Equation (4.28) and presented for the rectangular waveguide fully loaded with single DNG slab which has identical electric ε_r and magnetic parameters μ_r defined by single pole Lorentz models with $\omega_{pe} = \omega_{pm} = \omega_p = \omega_s \sqrt{48}/5$, $\omega_{oe} = \omega_{om} = \omega_o = \omega_s/5$ and $\Gamma_e = \Gamma_m = \Gamma = 0$ for $f_s=9$ GHz and different lengths (ℓ) of DNG slab along z-direction ($\ell=0.75a$, $\ell=a$ and $\ell=2a$). Loss affect is illustrated in Figure 4.16 while the damping factor is $\Gamma=0$ and $\Gamma=\omega_s/200$ for DNG slab with length of $\ell=0.75a$, and it can be clearly seen that a

reduction occurs in the absolute values of the reflection and transmission coefficients. The analytic results in lossless case for the example given in Figure 4.16a are compared with FDTD solutions which can be obtained by one of the dispersive FDTD algorithms given in Chapter 3. In the calculations presented in Figure 4.16b, we preferred to use the ADE approach due to its simplicity. For FDTD simulations 3-5-3 sinusoidal pulse with a center frequency of $f_s=9\text{GHz}$ is used as excitation, FDTD grid cell along x and z directions are chosen as 0.2286 mm and time step is 0.2694 ps. The length of rectangular waveguide is chosen as $5a$ and observation points wherein the reflected and transmitted waves are recorded is as 50 cells away the back and front faces of DNG slab. Hence, as seen in figure the performance of analytic and simulation results is in very close agreement.

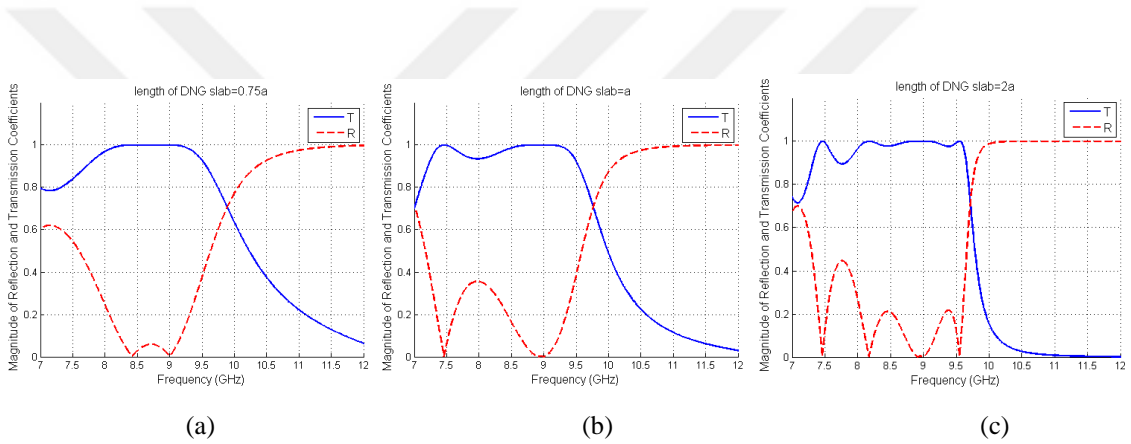


Figure 4.15 Reflection and transmission coefficients of DNG slab for a) $\ell=0.75a$, b) $\ell=a$ and c) $\ell=2a$ along z-direction

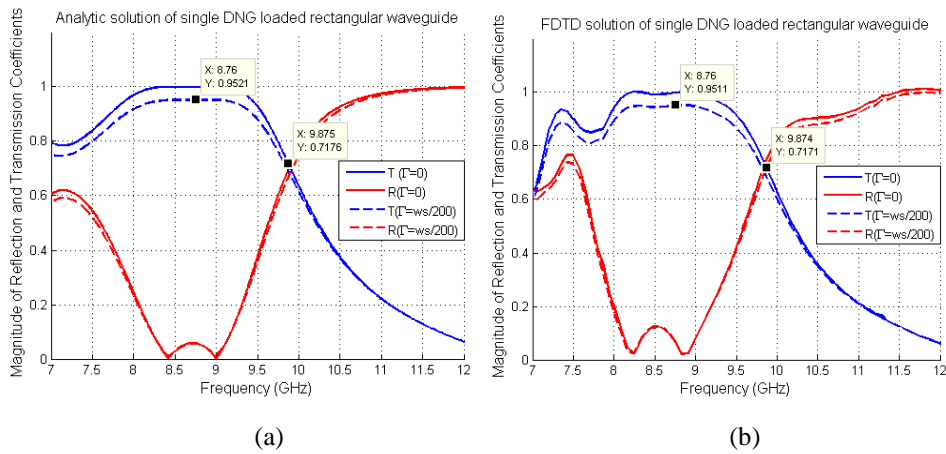


Figure 4.16 a) Analytic solution, b) FDTD solution of scattering parameters with/without losses for fully loaded single DNG slab with a length of $\ell=0.75a$

As another example given in Figure 4.17, analytic and FDTD numerical solutions of scattering characteristics of rectangular waveguide loaded with cascade connected double DNG slabs having length of $\ell_1=0.558\text{cm}$ and $\ell_2=0.5292\text{cm}$ are plotted. The problem scenario considered in this example is identical with the one reported in (Cimen, Cakir, & Sevgi, 2010). It consists of two directly cascaded DNG slabs of lengths ℓ_1 , ℓ_2 represented by different Lorentz models with parameters listed in Table 4.2. DNG regions completely fill the cross-section of the waveguide. In FDTD simulations, a (1-3-1) sinusoidal pulse is used as excitation with a center frequency of $f_s=10\text{GHz}$. As seen in the figure, this structure yields two stop bands in the frequency band 7–12GHz and FDTD simulation is almost same with analytic results. Moreover, our simulations results are also in very good agreement with those reported in (Cimen, Cakir, & Sevgi, 2010). It should be noted that the composite structure, as well as each one of the loaded sections do not exhibit DNG behavior over the entire frequency band considered, due to the different Lorentz models used in representing ϵ_r and μ_r . This is clearly seen from Figure 4.17a depicting the frequency variation of the refractive indices, which becomes purely imaginary in about 8–8.5GHz and 10.5–11GHz bands. Hence, one infers that unless ℓ_1 and ℓ_2 are not much smaller than signal wavelength, there would be negligible transmission within these frequency intervals.

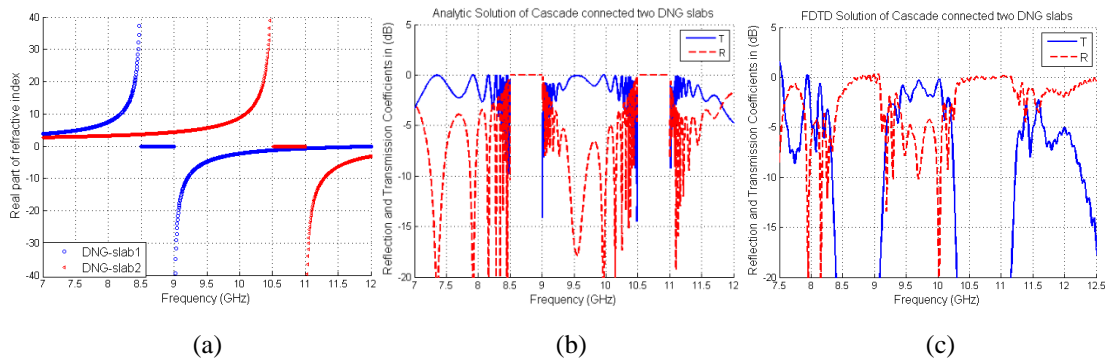


Figure 4.17 a)Refractive index and reflection/transmission coefficient in a rectangular waveguide loaded with double DNG slab calculated with b) Analytic solution and c) FDTD solution

Table 4.2 Lorentz Model Parameters for DNG Media

	DNG-slab1 ($\ell_1=0.5880\text{cm}$)	DNG-slab2 ($\ell_2=0.5292\text{cm}$)
$\omega_{pe,oe}$	$53.40 \times 10^9 \text{ rad/s}$	$65.97 \times 10^9 \text{ rad/s}$
$\omega_{pm,om}$	$56.54 \times 10^9 \text{ rad/s}$	$69.11 \times 10^9 \text{ rad/s}$
$\Gamma_{e,m}$	0	0

The last numerical example is presented for the partially loaded DNG slab which has same parameters used in the single DNG slab scenario. Reflection and transmission coefficients are obtained using the analytical equations obtained by the mode matching technique given in Equations (4.27–4.28) and plotted in Figure 4.18 for DNG slab thicknesses of $3a/4$ and $a/4$, respectively. The scattering characteristics shown in Figure 4.18 are consistent with the dispersion diagrams presented in Figure 4.5b and Figure 4.5e of Section 4.4.1. In Figure 4.19, an extended section of Figure 4.18a is given in the frequency region between 7–8GHz to distinguish the effect of loss for reflection and transmission. On the other hand, the accuracy of analytical solutions is of course dependent on the number of modes used in the expansions, which was taken as 30 in the calculations. As can be seen from Figure 4.19b reflection and transmission coefficients rapidly converge with increasing mode number used in the calculations, hence the accuracy obtained by using 30 modes is quite satisfactory.

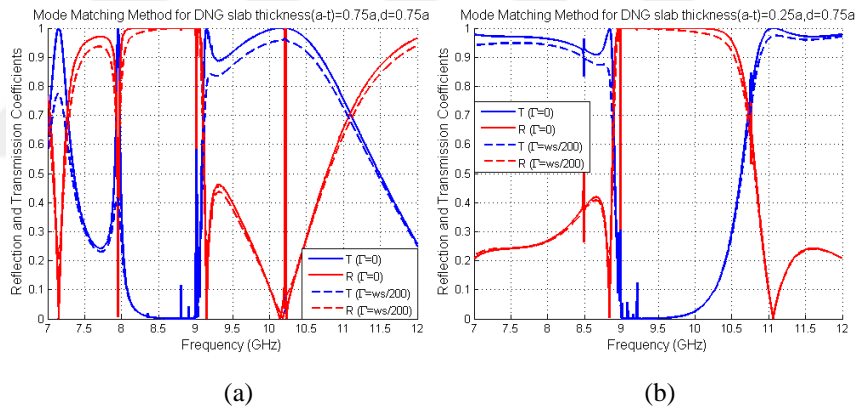


Figure 4.18 Reflection and transmission coefficients for lossless/lossy cases when a) $t=a/4$ and b) $t=3a/4$.

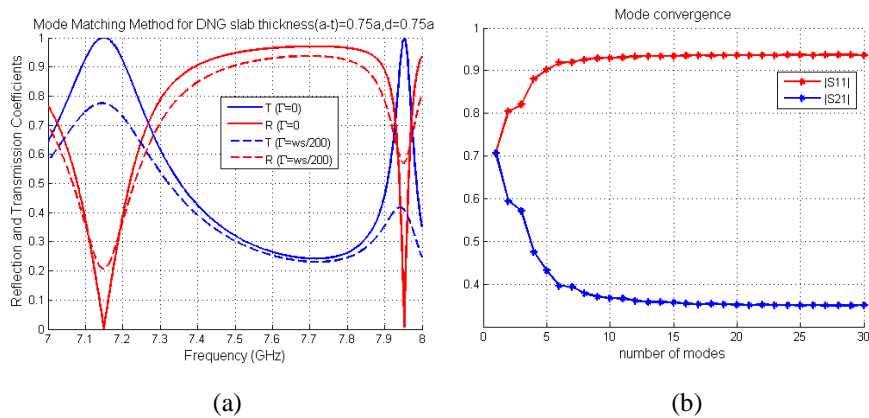


Figure 4.19 a) Reflection and transmission coefficients for lossless and lossy cases between 7-8GHz and b) mode convergence for lossless case at 8GHz.

4.8 Multiple DNG Loaded Sections Along Axial Direction

In the previous section partial DNG loading in the cross section of a rectangular waveguide and its effects on the propagation characteristics of the dominant TE₁₀ were investigated. In this section we will focus on propagation characteristics of the rectangular waveguide loaded with multiple DNG sections along axial direction. Although the presented analysis is also applicable in more general problems, for the sake of simplification here we will only consider the case wherein the DNG loaded sections extend over the cross section of the waveguide and the propagation of the dominant TE₁₀ mode. The problem can then be formulated as a cascade connection of two ports with transmission line representations, as shown in Figure 4.20, consisting of DPS-DNG loaded regions of electrical lengths θ_1 , θ_2 , impedances Z_1, Z_2 and propagation factors β_1, β_2 at fixed frequency.

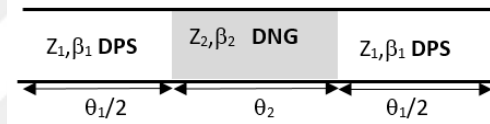


Figure 4.20 Transmission line representation for TE₁₀ mode of DPS/DNG loaded rectangular waveguide

Taking into account the relations given in Section 2.2 in obtaining transmission line representations for DPS and DNG loaded sections, the S matrix elements of the symmetric two-port in Figure 4.20 can be obtained in unified forms with the square root defined as the principle value in keeping with the convention adopted in the MATLAB code used in the calculations:

$$S_{11} = S_{22} = e^{-j\theta_1} \frac{2\Gamma}{1 + \Gamma^2 + j(1 - \Gamma^2)\cot(\theta_2)} ; S_{12} = S_{21} = e^{-j\theta_1} \frac{j(1 - \Gamma^2)/\sin\theta_2}{(1 + \Gamma^2) + j(1 - \Gamma^2)\cot\theta_2} \quad (4.34a)$$

with

$$\Gamma = \frac{t_1|\mu_{r2}| - t_2}{t_1|\mu_{r2}| + t_2} \quad \text{and} \quad \beta_i/k_0 = t_i = \sqrt{\epsilon_{ri}\mu_{ri} - \left(\frac{\lambda}{2a}\right)^2} ; \theta_i = k_0 t_i d_i \quad i = 1, 2 \quad (4.34b)$$

where λ , k_0 denote wavelength and wavenumber in air, p is the period of the periodic structure, and $d_2=d$, $d_1=p-d$ are the lengths of regions 2 and 1, respectively. Note that t_1 , t_2 , θ_1 and $\theta_2 >0$ and $|\Gamma| < 1$ for waves propagating in both media. S matrix representation for cascades of such two-ports can be obtained from equations given in Appendix C. When the cascaded two-ports are identical one will have a quasi-periodic structure, i.e., a periodic structure terminated at N periods, which are of special interest, since they lead to closed form solutions for the transfer characteristics, thereby enabling the designer to gain a fairly complete understanding on the effects of the various electrical and geometrical parameters of the structure in determining its frequency (and time) response. We will therefore investigate periodic structures as depicted in Figure 4.21 in more detail.

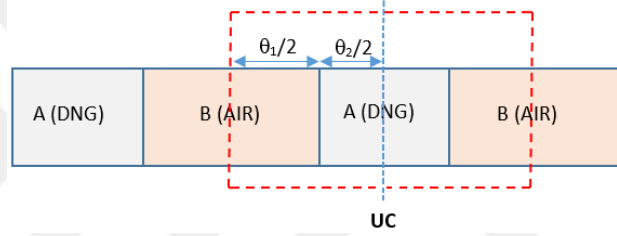


Figure 4.21 Periodic Structure and its Symmetric Unit Cell (UC)

Consider the symmetric unit cell (UC) of the periodic structure shown in Figure 4.21, represented by the scattering matrix elements given in Equation (4.34). By Floquet theorem the fields at the ports of the UC are required to be identical except for a constant factor, Λ as, $\Lambda \begin{bmatrix} a_1 \\ b_1 \end{bmatrix} = \begin{bmatrix} b_2 \\ a_2 \end{bmatrix}$. One then obtains,

$$\Lambda \begin{bmatrix} a_1 \\ b_1 \end{bmatrix} = \begin{bmatrix} (S_{12}S_{21} - S_{11}S_{22})/S_{12} & (S_{22}/S_{12}) \\ -(S_{11}/S_{12}) & (1/S_{12}) \end{bmatrix} \begin{bmatrix} a_1 \\ b_1 \end{bmatrix} ; \Lambda \begin{bmatrix} a_1 \\ b_1 \end{bmatrix} = M \begin{bmatrix} a_1 \\ b_1 \end{bmatrix} \quad (4.35)$$

We note that the two eigenvalues Λ_1, Λ_2 are related to the determinant and trace of M as,

$$\Lambda_1 \Lambda_2 = \det(M) = \frac{S_{21}}{S_{12}} = 1 \text{ (reciprocity)}; \Lambda_1 + \Lambda_2 = \text{trace}(M) = \frac{1 + S_{12}S_{21} - S_{11}S_{22}}{S_{12}} \quad (4.36)$$

Denoting $\Lambda_{1,2} = e^{\pm j\kappa p}$, where κ is the propagation constant of the periodic structure, one obtains the eigenvalue equation for Floquet waves as,

$$\cos(\kappa p) = \frac{S_{12}S_{21} + 1 - S_{11}S_{22}}{2S_{12}} = \frac{S_{12}^2 - S_{11}^2 + 1}{2S_{12}} \quad (4.37a)$$

When the structure is lossless S matrix is unitary and Equation (4.37a) reduces to

$$\cos(\kappa p) = \frac{\text{Re}\{S_{12}\}}{|S_{12}|^2} \quad (4.37b)$$

Substituting from Equation (4.34a) into Equation (4.37b) one obtains the eigenvalue equation of the waves (Floquet modes) supported by the periodic structure:

$$\cos(\kappa p) = \frac{\cos(\theta_2 - \theta_1) - \Gamma^2 \cos(\theta_2 + \theta_1)}{(1 - \Gamma^2)} \quad (4.38)$$

It should be noted Equation (4.38) differs from the well-known eigenvalue equation in DPS-DPS stratified periodic structures (Yeh, Yariv, & Hong, 1977), but can be obtained therefrom by the simple transformation $\theta_2 \rightarrow -\theta_2$, to account for co-directional and contra-directional flow in DPS, DNG regions, respectively. It should however, be noted that this sign change together with the dispersive nature of DNG medium will be shown to result in drastically different characteristics for Floquet modes. A remark which is similar to the one made in connection with the eigenvalue equation in Equation (4.6). Defining θ as $\theta = \kappa p$, pass/stop bands will be obtained for $|\cos(\theta)| < 1$, and $|\cos(\theta)| > 1$, respectively. The band edge frequencies for given period can be determined as a function of filling factor d/p using the condition $|\cos(\kappa p)| = \pm 1$ which yields four families as,

$$\Gamma \sin\left(\frac{\theta_1 + \theta_2}{2}\right) = \pm \sin\left(\frac{\theta_1 - \theta_2}{2}\right) \quad \text{and} \quad \Gamma \cos\left(\frac{\theta_1 + \theta_2}{2}\right) = \pm \cos\left(\frac{\theta_1 - \theta_2}{2}\right) \quad (4.39)$$

A band edge diagram calculated for identical Lorentz models with the normalized parameters where $a=2.286$; $c=30$; $f_s=9$; $\omega_s = 2\pi f_s$, $\omega_{pe} = \sqrt{48}/5$, $\omega_{oe}=1/5$ and $p=3.3$ is depicted in Figure 4.22a as a function of filling factor d/p . The band diagram for $d/p=0.3$ is also given in Figure 4.22b to demonstrate the stop-pass band frequency intervals. For given material parameters and period, band edge diagrams provide a very convenient means for determining, in one glance, the value of the loading factor d/p , and the resulting stopband (band gap), passband (which fill in the voids between the band gaps) characteristics of the periodic structure. For example, the value of $d/p=0.3$ shown in Figure 4.22a yields the limiting frequencies of three stop bands as shown in Figure 4.22b. One infers that there will be three passbands for f (GHz) <7.7 , $8.1 < f$ (GHz) <9.6 and $10.3 < f$ (GHz) <11.25 in the frequency region (7-12 GHz) and three stopbands in $7.7 < f$ (GHz) <8.1 , $9.6 < f$ (GHz) <10.3 and $11.25 < f$ (GHz) in the frequency region (7-12 GHz).

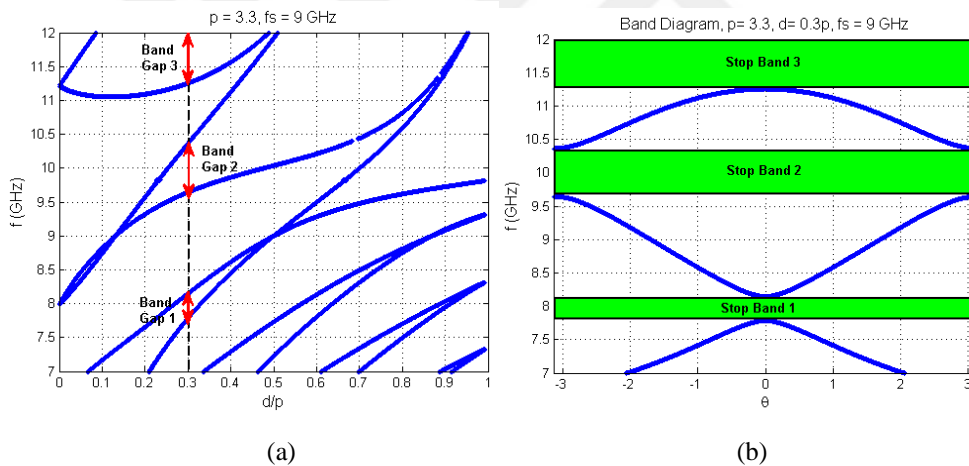


Figure 4.22 a) Band edge diagram and b) Stop-Pass band frequency intervals for $d/p=0.3$.

Supposing that d/p is equal to 1, which means the unit cell is fully loaded with DNG slab, propagating waves are supported in the waveguide at frequencies below 9.8 GHz but not above that frequency. In this case, one can say that 9.8 GHz is cutoff frequency for fully loaded structures and hence, band edge diagram plotted in Figure 4.22a is consistent with dispersion diagram given in Figure 4.5a. On the other hand, as can easily be seen from Figure 4.22a, when d/p is equal to 0, which means the waveguide is empty, no band gaps occur and as a result the wave propagates along the waveguide over the frequency band 7–12 GHz.

In the absence of losses, a strictly periodic structure would yield a binary 0/1 reflection (R) and transmission (T) characteristic, with R=1, T=0 in stop bands and R=0, T=1 in pass bands. This characteristic can only be achieved in case the structure is not terminated (infinite), which is non-physical, or in case it is terminated in its characteristic impedance, the Bloch impedance (Z_B), which is not possible due to wildly varying nature of Z_B , in the presence of stop/pass bands (Foroozesh & Shafai, 2008). Therefore, the transfer characteristics of truncated periodic structures, obtained by terminating the periodic structure after a number of periods (N), in some appropriate way, are of more interest. The S parameters of a cascade of N unit cells (UC's) can easily be calculated using the S matrix elements of the UC in Equation (4.34) and the equations given in Equation (C.11) of Appendix C. Thus, when the superscript N is used for the S parameters of the cascade of N UC's, and the structure is terminated into empty waveguide without taking some additional measures one would have $R = S_{11}^N$ and $T = S_{21}^N$. However, for this termination strategy one can use the closed form expression derived for the power reflection coefficient $|R|^2$ of N cascaded DPS-DPS UC's in (Yeh, Yariv, & Hong, 1977), but can be shown to be directly applicable also to the DPS-DNG UC's, which translated into our notation as,

$$|R|^2 = \frac{|C|^2}{|C|^2 + [\sin(\kappa p) / \sin(N\kappa p)]^2} ; |C|^2 = \frac{|S_{11}^{UC}|^2}{1 - |S_{11}^{UC}|^2} \quad (4.40)$$

where S_{11}^{UC} is given in Equation (4.34) and, in the lossless case $|T|^2$ is obtained from power conservation relation simply as $|T|^2 = 1 - |R|^2$. Power reflection (R) and transmission (T) coefficients through a single UC and a cascade of 15 UC's terminated in air region without tapered sections are illustrated in Figures 4.23a and 4.23b, which clearly show the evolution of the transfer characteristic of a strictly periodic structure given in Figure 4.22 as the number of the UC's is increased. The effects of (abrupt) termination of a periodic structure can readily be inferred from Equation (4.40) which shows that the reflectivity $|R|^2$ (and hence $|T|^2$) will fluctuate increasingly faster for higher values of N, in the pass bands, wherein κ is real, due to the rapidly varying character of the second term in the denominator. This term will however decay exponentially in the stop bands,

wherein κ is imaginary. Hence, $|R|^2$ of the truncated structure will quickly approach to that of the strictly periodic structure as N is increased. This behavior is clearly seen in Figure 4.23c obtained for $p=3.3$, $d/p=0.3$, $f_s=9\text{GHz}$ and $N=15$.

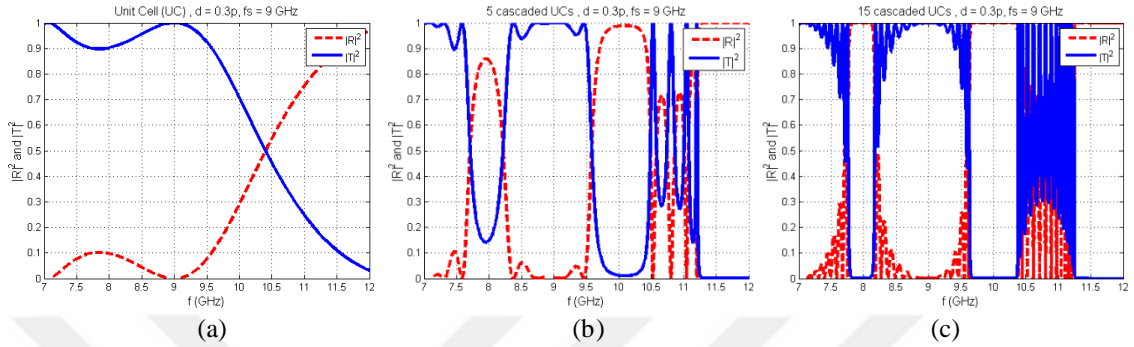


Figure 4.23 Power Reflection Transmission Characteristics of a) Unit Cell (UC), b) 5 cascaded UC's and c) 15 cascaded UC's (Parameter values used in the calculations are same as those used for Figure 4.22)

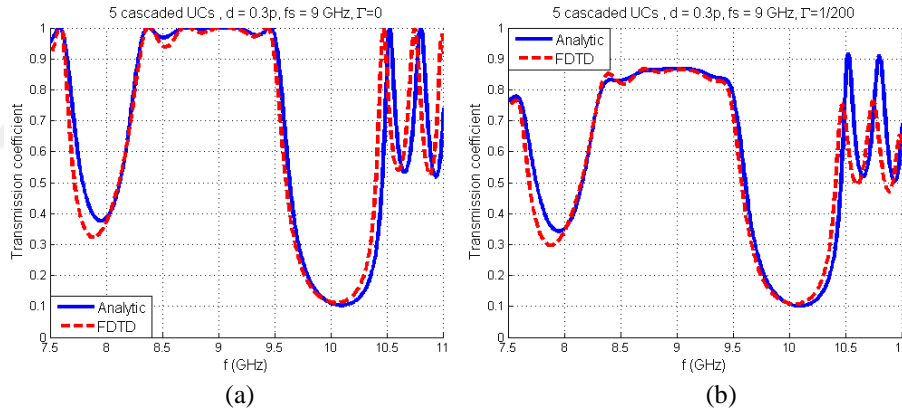


Figure 4.24 Transmission coefficient for a) lossless case and b) lossy case

In Figure 4.24, transmission coefficients of waveguide filled with 5 cascade connected DNG slabs (with identical Lorentz models and same unit cell size) are plotted for both lossless ($\Gamma=0$) and lossy ($\Gamma=1/200$) cases and the analytical solutions are compared with the results of the FDTD simulations. In FDTD simulations problem space is taken to be 100 cells along x -direction and 1200 cells along z -direction. The first unit cell extends from cell 200 to cell 345 in the z direction and the other unit cells are connected cascade. FDTD grid parameters are chosen as $\Delta x = \Delta z = a/100$ and the time step is taken as 0.95 times the Courant limit. A sinusoidal source (1-3-1 pulse) is used as excitation with a center frequency about 9GHz and launched before the first unit cell in

free space region. Problem space is terminated with second order Mur-type ABC for sufficient absorption. The transmitted field is recorded at an observation point behind the periodic structure and then the transmission coefficient at each frequency is calculated as described in Section 3.5.2. As seen from this figure, numeric results obtained with/without loss exhibit perfect agreement with the analytical results over the frequency range 7.5–11GHz.

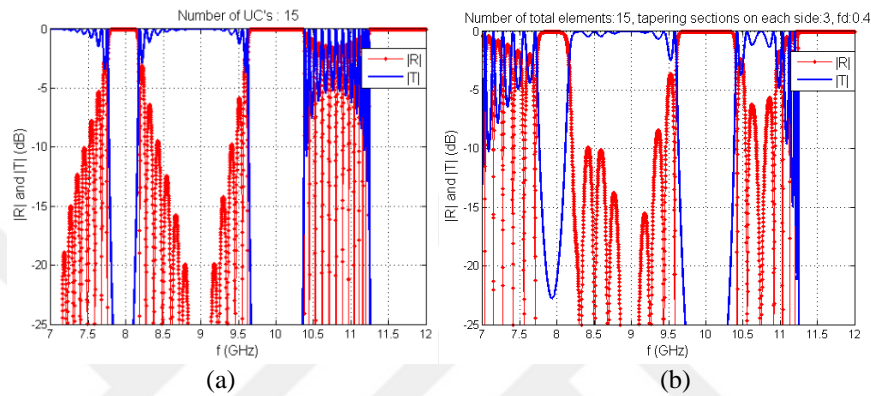


Figure 4.25 Power Reflection Transmission Characteristics of 15 cascaded UC's a) without tapering and b) with 3 tapering section on each side.

As noted above truncating a periodic structure imperfectly, without using some impedance matching approach, has pronounced adverse effects mainly in the bandpass regions which are due to interference of multiply reflected wave constituents arising from the discontinuities at the termination boundaries. The reflection-transmission characteristic of a truncated structure would better mimic that of a strictly periodic one only when terminated in some more appropriate way, rather than abruptly as was done above. The determination of the optimal termination method is problem specific, and beyond the scope of this general investigation. It would however be instructive to give an example of possible improvement that can be achieved by using a simple tapering technique. A plot obtained using this approach is given in Figure 4.25, where the truncated structure is identical to the one considered in Figure 4.23c, except that the loading factors of three elements on the sides of input and output ports have been reduced by factors of (0.4) , $(0.4)^2$ and $(0.4)^3$ in moving away from the ports. As can be seen, even this simple measure is quite effective in substantially decreasing the ripples in the transmission band observed in Figure 4.25a caused by the discontinuity introduced due to abrupt truncation.

5. CONCLUSIONS

In the last two decades the unconventional characteristics of electromagnetic waves propagating in metamaterials (MTM) has grown to be an area of intensive theoretical and applied research.

The work reported in this thesis addresses some lesser investigated numerical and analytical problems of the area. These being related to some implementational aspects of the Finite Difference Time Domain (FDTD) algorithm, and to eigen-waves in certain uniform wave guiding structures loaded with DNG media. In both fields, the results presented in the thesis provide some contributions to the existing literature.

This concluding chapter is organized under three headings. In the first one we present a summary of the work performed in the thesis. This is followed by a list of the main contributions together with related published and pending work. The final part contains suggestions for follow-up problems for future research. Necessarily, there will be some overlapping between the material covered in the first two sections, and that of the Introduction Chapter of this thesis, which, however, will be kept at a minimum.

Summary of the work done

Analytic formulation problems of electromagnetic wave propagation are only possible in certain idealized environments, yielding so-called canonical problems. Problems involving MTM media produce some extra complications due to the resonant behavior of their frequency dispersion and to inhomogeneity and anisotropy resulting from production methods of these artificial dielectrics, which generally involve periodically arranged discontinuities having sub-wavelength dimensions. The commonly adopted approaches in the literature are either to resort to available full-wave electromagnetic simulators such as HFSS and CST for number-cranking; or, more often, to introduce the simplifying assumptions of homogeneous and isotropic MTM medium having dispersive characteristics described by some functional form. The second approach is used in this thesis.

The formulations applicable to media having negative values of constitutive parameters which are relevant for the numerical and analytical investigations performed

in the thesis are summarized in Chapter 2. These include dispersion models, proper branch cuts for refractive index and wave impedance.

FDTD algorithm is chosen for numerically investigating wave characteristics in the presence of MTM media in the problem domain. The outputs obtained via FDTD approach provide physical insight for the time-evolution of reflected and transmitted wave fields through transient into steady-state regimes. The dispersive nature of MTM's requires substantial modifications of the well-known FDTD algorithms developed for nondispersive media. We have, therefore, derived the formulations of all codes used in the thesis and implemented them. Chapter 3 of the thesis is devoted to the work done in this context. This chapter contains formulations of Maxwell's curl and wave equation based FDTD update equations, Auxiliary Differential Equation (ADE) and Piecewise Linear Recursive Convolution (PLRC) methods for incorporating dispersion, comparison of and contributions to the Absorbing Boundary Conditions (ABC) used in terminating computational domains, together with representative examples of computed results.

Frequency domain approaches may provide advantages in attacking electromagnetic wave propagation problems involving frequency dispersive media or/and waveguide environments, since all dispersive parameters reduce to constants at fixed frequencies. Hence, for canonical problems one can work out exact analytical formulations which when superposed yield benchmark solutions for the frequency dependence of wave fields.

In Chapter 4 of this thesis we considered the canonical problem of propagation in a rectangular waveguide loaded fully or partially with MTM media along a transverse and also along the axial directions. For brevity, but without loss of generality, we considered the problem geometries wherein wave equations effectively involve a single spatial coordinate, and hence result in significant simplification of formulations and calculations. This chapter contains the solutions for the evanescent, propagating and complex eigenwaves in regions transversely stratified with MTM media as depicted in Figure 4.1 (partially loaded in cross-section), including complete and unified analysis of the existence conditions for, and cut-off transitions between supported wave types, and also their dependence on the problem parameters and frequency. Representative numerical results are provided for dispersion diagrams, for variation of phase and group velocities of forward, backward and surface wave type fields and also for the transmission-reflection

characteristics of such sections as a function of their axial extent. Truncated periodic type DPS-DNG stratifications along the axial direction, shown in Figure 4.21, are also investigated in Chapter 4. In this context eigenvalue and band-edge equations for Floquet waves are obtained, representative solutions are presented for dispersion and band edge diagrams. Reflection-transmission characteristics and their dependence on the number of unit cells and the termination strategy used in the truncated structure are also investigated. Frequency dependence of reflection and transmission is calculated using both the frequency domain approach and also FDTD and are shown to be in excellent agreement.

Contributions and outcomes

- The outcomes of the preparatory investigations on the modeling of the dispersive characteristics of homogeneous, isotropic MTM media and implementations of these into FDTD algorithms for demonstrating some salient features of the electromagnetic waves supported in MTM environments are reported as a tutorial review in (Pekmezci & Sevgi, 2014).
- Most, if not all, of the existing literature on FDTD solutions for problems containing MTM media use update algorithms based on Maxwell's curl equations. We have also worked out FDTD update equations based on scalar wave equation and shown in (Pekmezci, Topuz, & Sevgi, 2016) that it yields computational advantages in addressing propagation problems in uniform MTM environments.
- In performing FDTD calculations involving structures imbedded in extended homogeneous regions one needs to introduce artificial boundaries for terminating the computational domain and use Perfectly Matched Layer (PML) or Mur type Absorbing Boundary Conditions (ABC) for suppressing spurious reflections from these terminations. We have derived FDTD update equations for 2D Mur type ABC's and shown that in dealing with MTM loaded 2D problems investigated in this thesis it provides definite computational advantages and suppresses boundary reflections by more than 40dB. A performance which is perfectly acceptable for our calculations, although its inferior to that obtainable via the PML approach. The outcomes of these investigations are reported in (Pekmezci, Topuz, & Sevgi, 2018).

- Different types of modal fields may be supported by waveguides transversely loaded with MTM media. In the absence of losses there may be evanescent, forward/backward propagating, surface and complex waves. Considering the canonical problem of propagation in DPS/DNG layered planar waveguides the existence conditions of and the transitions between these wave types are investigated via exact frequency domain analysis and numerical results are obtained as functions of the geometrical parameters using identical/non-identical, lossless/lossy Lorentz models for the MTM slab. Novel conditions are obtained for the existence conditions of complex and surface wave type modal fields. The outcomes of these investigations are submitted for publications.

Suggestions for follow-up work

During the course of this work several problem areas have been identified as deserving further attention. These problem areas are listed below as suggestions for follow-up work.

- Implementation of FDTD algorithm to waveguides layered in the transverse or axial directions with single negative (Epsilon Negative: ENG or Mu Negative: MNG), double negative (DNG) and double positive (DPS) media. This work involves working out FDTD update equations for addressing dispersive media models as well as for the transition conditions at the various boundaries of the problem domain. To the best of our knowledge, an accurate and stable algorithm has not yet been reported in the literature.
- Formulation of FDTD update equations of 3D Mur type ABC's for dispersive media. This work involves an extension of the 2D Mur update equations presented in Chapter 3. It is expected that 3D Mur will provide some advantages over the alternative approach of 3D PML type ABC, in requiring less computational resources.

Determination of propagation characteristics of waves in waveguides loaded in the transverse or axial directions with combinations of ENG, MNG, DNG and DPS type layers. Although the exact frequency domain analysis presented in Chapter 4 for DNG/DPS stratifications is, in principle, also applicable to problems involving ENG,

MNG layers, the resulting wave characteristics will exhibit distinctly different features from the ones treated in the thesis. As discussed in Chapter 2 propagating waves are not supported in ENG, MNG layers. Since propagation phenomena in such mixed media structures involves tunneling of evanescent fields, a separate, detailed analysis is needed for determining its dependence on medium dispersion models and the geometrical problem parameters for both transversely and axially stratified structures.



REFERENCES

- Alu, A., & Engheta, N. (2004). Guided Modes in a Waveguide Filled With a Pair of Single-Negative (SNG), Double-Negative (DNG), and/or Double-Positive (DPS) Layers. *IEEE Trans. Microw. Theory Techn.*, 52(1), 199-210.
- Alu, A., & Engheta, N. (2005). Polarizabilities and effective parameters for collections of spherical nano-particles formed by pairs of concentric double-negative (DNG), single-negative (SNG) and/or double-positive (DPS) metamaterial layers. *J. Appl. Phys.*, 97, 1-12.
- Antoniades, M. A., & Eleftheriades, G. V. (2003). Compact linear lead/lag metamaterial phase shifters for broadband applications. *IEEE Antennas and Wireless Propagation Letters*, 2, 103-106.
- Aoyagi, P. H., Lee, J. F., & Mittra, R. (1993). A Hybrid Yee Algorithm/Scalar-Wave Equation Approach. *IEEE Trans. Microw. Theory Techn.*, 41(9), 1593-1599.
- Baccarelli, P., & et.al. (2005). Fundamental modal properties of surface waves on metamaterial grounded slabs. *IEEE Trans. Microw. Theory Techn.*, 53(4), 1431-1442.
- Balaji, U., & Vahldieck, R. (1998). Mode-matching analysis of circular-ridged waveguide discontinuities. *IEEE Trans. Microw. Theory Techn.*, 46(2), 191-195.
- Balanis, C. A. (2012). *Advanced Engineering Electromagnetics* (2nd ed.). John Wiley & Sons, Inc.
- Berenger, J. P. (1994). A Perfectly Matched Layer for the Absorption of Electromagnetic Waves. *Journal of Computational Physics*, 114, 185-200.
- Berenger, J. P. (1996). Three-dimensional perfectly matched layer for the absorption of electromagnetic waves. *Journal of Computational Physics*, 127, 363-379.
- Berenger, J. P. (2007). *Perfectly Matched Layer (PML) for Computational Electromagnetics*, ser. *Synthesis Lectures on Computational Electromagnetics*. (C. Balanis, Ed.) Morgan & Claypool.
- Bilotti, F., & Sevgi, L. (2012). Metamaterials: Definitions, Properties, Applications, and FDTD-Based Modeling and Simulation (Invited Paper). *RFMiCAE, International Journal on RF and Microwave Computer-Aided Engineering*, 22(4), 422-438.

- Çakır, M., Çakır, G., & Sevgi, L. (2008). A Two-dimensional FDTD-Based Virtual Metamaterial – Wave Interaction Visualization. *IEEE Antennas and Propagation Magazine*, 50(3), 166-175.
- Capolino, F. (2009). *Applications of Metamaterials*. Boca Raton, FL: CRC Press.
- Chan, K. L., & Judah, S. R. (1998). Mode-matching analysis of a waveguide junction formed by a circular and a larger elliptic waveguide. *IEE Proc. Microwaves, Antennas and Propagation*, 145(1), 123–127.
- Chen, H., & Chen, M. (2011). Flipping photons backward: reversed Cherenkov radiation. *Materialstoday*, 14, 34-41.
- Chen, H., Ran, L., Huangfu, J., Zhang, X., & Chen, K. (2004). Left-handed materials composed of only S-shaped resonators. *The American Physical Society, Physical Review E*, 70, 057605.
- Chen, J., & et.al. (2011). Observation of the inverse Doppler effect in negative-index materials at optical frequencies. *Nature Photonics*, 5, 239-245.
- Chettiar, U. K., & et.al. (2007). Dual-band negative index metamaterials: Double-negative at 813nm and single negative at 772 nm. *Opt. Lett.*, 32, 1671-1673.
- Chew, W. C., & Weedon, W. H. (1994). A 3d perfectly matched medium from modified maxwell's equations with stretched coordinates. *Microwave Opt. Technol. Lett*, 7, 599-604.
- Cimen, S., Cakir, G., & Sevgi, L. (2010). Filter Design and Mode Suppression Inside Metamaterial filled Rectangular Waveguides. *Microwave and Optical Tech. Letters*, 52(7), 1659-1663.
- Clarricoats, P. J., & Slinn, K. R. (1965). Complex modes of propagation in dielectric loaded circular waveguide. *Electron. Lett.*, 1, 145-146.
- Cory, H., & Shtrom, A. (2004). Wave propagation along a rectangular metallic waveguide longitudinally loaded with a metamaterial slab. *Microw. and Opt. Tech. Lett.*, 41(2), 123-127.
- Cummer, S. A. (2003). A simple, nearly perfectly matched layer for general electromagnetic media. *IEEE Microwave Wireless Compon. Lett.*, 13, 128–130.
- Cummer, S. A. (2004). Perfectly Matched Layer Behavior in Negative Refractive Index Materials. *IEEE Antennas and Wireless Propagation Letters*, 3, 172-175.
- Davidson, D. B. (2011). *Computational Electromagnetics for RF and Microwave Engineering, Second Edition*. New York: Cambridge University Press.

- Duan, Z. Y., Wu, B. I., Chen, H. S., Xi, S., & Chen, M. (2009). Research progress in reversed Cherenkov radiation in double-negative metamaterials. *Prog. Electromagn. Res*, 90, 75-87.
- Eleftheriades, G. V., & Engheta, N. (2011). Metamaterials: Fundamental, and Applications in the Microwave and Optical Regimes. *Proc. IEEE (Special Issue)*, 99(10), 1618-1621.
- Eleftheriades, G. V., & Grbic, A. (2002). Experimental verification of backward-wave radiation from a negative refractive index metamaterial. *J. Appl. Phys.*, 92(10), 5930-5935.
- Eleftheriades, G. V., Iyer, A. K., & Kremer, P. C. (2002). Planar Negative Refractive Index Media Using Periodically L-C Loaded Transmission Lines. *IEEE Trans. on MTT*, 50(12), 2702-2712.
- Engheta, N. (2002). An idea for thin sub-wavelength cavity resonators using metamaterials with negative permittivity and permeability. *IEEE Antennas and Wireless Propagation Letters*, 10-13.
- Engheta, N., & Ziolkowski, R. W. (2006). *Metamaterials: Physics and Engineering Explorations*. NJ: John Wiley & Sons.
- Engquist, B., & Majda, A. (1977). Absorbing Boundary Conditions for the Numerical Simulation of Waves. *American Mathematical Society, Mathematics of Computation*, 31(139), 629-651.
- Fan, G. X., & Liu, Q. H. (2000). An FDTD algorithm with perfectly matched layers for general dispersive media. *IEEE Trans. Antennas Propagation*, 48, 637-646.
- Foroozesh, A., & Shafai, L. (2008). Wave Propagation in 1D EBGs: Periodic Multilayer Films Consisting of Two Different Materials. *IEEE Antennas and Propagation Magazine*, 50(2), 175-182.
- Galyamin, S., & Tyukhtin, A. (2010). Electromagnetic field of a moving charge in the presence of a left-handed medium. *Phys. Rev. B*, 81(23), 235134.
- Gedney, S. D. (1996a). An anisotropic perfectly matched layer-absorbing medium for the truncation of fdtd lattices. *IEEE Transactions on Antennas and Propagation*, 44, 1630-1639.
- Gedney, S. D. (1996b). An anisotropic pml absorbing media for the fdtd simulation of fields in lossy and dispersive media. *Electromagnetics*, 16, 399-415.

- Gedney, S. D., & Zhao, B. (2010). An auxiliary differential equation formulation for the complex-frequency shifted PML. *IEEE Trans. Antennas Propagation*, 58(3), 838–847.
- Golio, M., & Golio, J. (2008). *The RF and Microwave Handbook: RF and Microwave, Circuits, Measurements, and Modeling* (2nd ed.). New York: CRC Press.
- Gundogdu, T. F., & et.al. (2008). Negative index short-slab pair and continuous wires metamaterialsin the far infrared regime. *Opt. Expr*, 16(12), 9173-9180.
- Hao, Y., & Mittra, R. (2009). *FDTD Modeling of Metamaterials: Theory and Applications*. USA: Artech House Inc.
- Helszajn, J. (2000). *Ridge Waveguides and Passive Microwave Components*. London: IET Electromagnetic Waves Series, The Institution of Engineering and Technology.
- Heyman, E., & Ziolkowski, R. W. (2001). Wave propagation in media having negative permittivity and permeability. *Phys. Rev. E*, 64, 1-15.
- Higdon, R. L. (1986). Absorbing boundary conditions for difference approximations to the multi-dimensional wave equation. *Math. Comput*, 47, 437-459.
- Inan, U. S., & Marshall, R. (2011). *Numerical Electromagnetics: The FDTD Method*. New York: Cambridge University Press.
- Irci, E. (2007, August). *Wave propagation in metamaterial structures and retrieval of homogenization parameters*. Retrieved from (Master Thesis): <http://www.thesis.bilkent.edu.tr/0003355.pdf>
- Jackson, J. D. (1998). *Classical Electrodynamics*. Hoboken, NJ: Wiley.
- Jakšić, Z., Dalarsson, N., & Maksimović, M. (2006). Negative Refractive Index Metamaterials: Principles and Applications. *Microwave Review*, 12(1), 36-49.
- Kafesaki, M., & et.al. (2007). Left-handed metamaterials: The fishnet structure and its variations. *Phys. Rev. B*, 75.
- Kalluri, D. K. (2012). *Electromagnetic Waves, Materials, and Computation with MATLAB*. New York: CRC Press.
- Kashiwa, T., & Fukai, I. (1990). A Treatment by FDTD Method of Dispersive Characteristics Associated with Electronic Polarization. *Microwave and Optical Technology Letters*, 3, 203–205.

- Kelley, D., & Luebbers, R. J. (1996). Piecewise Linear Recursive Convolution for Dispersive Media Using FDTD. *IEEE Trans on Antennas and Propagation*, 44(6), 792–797.
- Kim, K. Y. (2009). Comparative Analysis of Guided Modal Properties of Double-Positive and Double-Negative Metamaterial Slab Waveguides. *Radioengineering*, 18, 117-123.
- Kishor, K., Baitha, M. N., Sinha, R. K., & Lahiri, B. (2014). Tunable negative refractive index metamaterial from V-shaped SRR structure: fabrication and characterization. *Optical Society of America B*, 31(7), 1410-1414.
- Kosmas, P., & Rappaport, C. (2004). A Simple Absorbing Boundary Condition for FDTD Modeling of Lossy, Dispersive Media Based on the One-Way Wave Equation. *IEEE Transactions on Antennas and Propagation*, 52(9), 2476-2479.
- Li, J., & Dai, J. (2006). Z-Transform Implementation of the CFS-PML for Arbitrary Media. *IEEE Microwave and Wireless Components Letters*, 16(8), 437-439.
- Li, Z., Aydin, K., & Ozbay, E. (2010). Transmission spectra and the effective parameters for planar metamaterials with omega shaped metallic inclusions. *Optics Communications*, 283, 2547-2551.
- Liao, Z. P., Wong, H. L., Yang, B. P., & Yuan, Y. F. (1984). A transmitting boundary for transient wave analysis. *Scientia Sinica, Ser. A*, 27(10), 1063-1076.
- Lu, J., & et.al. (2003). Cerenkov radiation in materials with negative permittivity and permeability. *Opt. Express*, 11, 723-734.
- Lu, L. (2006). *Characterization and Application of Left-Handed Meta-Materials Using the Dispersive Finite-Difference Time-Domain Method*, Ph.D. Dissertation. United Kingdom: Queen Mary, University of London.
- Luebbers, R. J., & Hunsberger, F. (1992). FDTD for Nth-order Dispersive Media. *IEEE Trans. on Antennas Propagation*, 40(11), 1297-1301.
- Luebbers, R. J., Hunsberger, F., & Kunz, K. S. (1991). A frequency-dependent finite-difference timedomain formulation for transient propagation in plasma. *IEEE Trans. On Antennas Propagation*, 39, 29–34.
- Luebbers, R. J., Hunsberger, F., Kunz, K. S., Standler, R. B., & Schneider, M. (1990). A Frequency Dependent Finite-Difference Time-Domain Formulation for Dispersive Materials. *IEEE Trans. on EMC*, 32, 222–227.

- Mitra, R., Rajab, K., & Lanagan, M. T. (July 2005). Size reduction of microstrip antennas using metamaterials ., *Proc. IEEE AP-S*. Washington.
- Mur, G. (1981). Absorbing Boundary Conditions for the Finite Difference Approximation of the Time-Domain Electromagnetic-Field Equations. *IEEE Trans. Electromagn. Compat.*, 23(4), 377–382.
- Nefedov, I. S., & Tretyakov, S. A. (2003). Waveguide containing a backward-wave slab. *Radio Sci.*, 38, 1101-1109.
- Ozakın, M. B., & Aksoy, S. (2013). A constant recursive convolution technique for frequency dependent scalar wave equation based FDTD algorithm. *J Comput Electron*, 12, 752-756.
- Pekmezci, A., & Sevgi, L. (2014). FDTD-Based Metamaterial (MTM) Modeling and Simulation. *IEEE Antennas and Propagation Magazine*, 56(5), 289-303.
- Pekmezci, A., Topuz, E., & Sevgi, L. (2016). Finite Difference Time Domain Formulation for Epsilon-Negative Medium Using Wave Equation. *International Journal of RF and Microwave Computer-Aided Engineering*, 26(4), 304-310.
- Pekmezci, A., Topuz, E., & Sevgi, L. (2018). First and Second Order Mur Type ABCs for DNG Media. *ACES JOURNAL*, 33(6), 569-574.
- Pendry, J. B. (2000). Negative Refraction Makes a Perfect Lens. *Physical Review Letters*, 85(18), 3966-3969.
- Pendry, J. B., & Brien, S. O. (2002a). Very- low frequency magnetic plasma. *Journal of Physics: Condensed Matter*, 14(32), 7809-7416.
- Pendry, J. B., & Brien, S. O. (2002b). Magnetic activity at infrared frequencies in structures metallic photonic crystals. *Journal of Physics: Condensed Matter*, 14(25), 6383-6394.
- Pendry, J. B., Holden, A. J., Robbins, D. J., & Stewart, W. (1998). Low frequency plasmons in thin-wire structures. *Journal of Physics: Condensed Matter*, 10, 4785–4809.
- Pendry, J. B., Holden, A. J., Robbins, D. J., & Stewart, W. (1999). Magnetism from conductors and enhanced nonlinear phenomena. *IEEE Transactions on Microwave Theory and Techniques*, 47, 2075–2084.
- Pendry, J. B., Holden, A. J., Stewart, W. J., & Youngs, I. (1996). Extremely Low Frequency Plasmons in Metallic Mesostructures. *Phys. Rev. Lett.*, 76, 4773-4776.

- Ramakrishna, S. A. (2005). Physics of negative refractive index materials. *Rep. Prog. Phys.*, 68, 449–521.
- Ramakrishna, S. A., & Grzegorzczak, T. M. (2001). *Physics and Applications of Negative Refractive Index Materials*. CRC Press.
- Roden, J., & Gedney, S. D. (2000). Convolution PML (CPML): An efficient FDTD implementation of the CFS-PML for arbitrary media. *Microwave and Opt. Tech. Lett.*, 27, 334–339.
- Rozzi, T., & et.al. (1998). General Constraints on the Propagation of Complex Waves in Closed Lossless Isotropic Waveguides. *Trans. MTT*, 6(5), 512-516.
- Rozzi, T., & Farina, M. (1999). *Advanced Electromagnetic Analysis of Passive and Active Planar Structure*. London: The Institution of Electrical Engineers.
- Sabah, C. (2010). Tunable Metamaterial Design Composed Of Triangular Split Ring Resonator And Wire Strip For S- And C- Microwave Bands. *Progress In Electromagnetics Research B*, 22, 341-357.
- Sacks, Z. S., Kingsland, D. M., Lee, R., & Lee, J. R. (1995). A perfectly matched anisotropic absorber for use as an absorbing boundary condition. *IEEE Transactions on Antennas and Propagation*, 43, 1460-1463.
- Sadiku, M. N. (2001). *Numerical Techniques in Electromagnetics* (2nd ed.). Washington: CRC Press.
- Schmidt, R., & Russer, P. (1995). Modeling of cascaded coplanar waveguide discontinuities by the mode-matching approach. *IEEE Trans. Microwave Theory Techniques*, 43, 2910–2917.
- Schultz, S., Smith, D. R., Padilla, W. J., Vier, D. C., & Nemat-Nasser, S. C. (2000). Composite media with simultaneously negative permeability and permittivity. *Physical Review Letters*, 84(18), 4184–4187.
- Schurig, D., & et.al. (2006). Metamaterial Electromagnetic Cloak at Microwave Frequencies. *Science*, 314(5801), 977-980.
- Seddon, N., & Bearpark, T. (2003). Observation of the inverse Doppler effect. *Science*, 302, 537-1540.
- Shalaev, V. M., & et.al. (2005). Negative index of refraction in optical metamaterials. *Opt.Lett.*, 30(24), 3356-3358.
- Shelby, A., Smith, D. R., & Schultz, S. (2001). Experimental verification of a negative index of refraction. *Science*, 292, 77–79.

- Siakavara, K. (2007). Modal analysis of the microwave frequency response and composite right-/left-handed operation of a rectangular waveguide loaded with double positive and double negative materials. *Int. Journal of RF and Microwave Computer-Aided Engineering*, 17, 435–445.
- Şimşek, S., Işık, C., & Topuz, E. (2011). *Mikrodalga Tekniği: Pasif Devreler ve Çözümlü Problemler*. İstanbul: Papatya Yayıncılık.
- Smith, D. R., & Kroll, N. (2000). Negative refractive index in left-handed materials. *Phys. Rev. Lett*, 85, 2933–2936.
- Sullivan, D. M. (1992). Frequency-Dependent FDTD Methods Using Z Transforms. *IEEE Trans. on Antennas and Propagation*, 40, 1223–1230.
- Sullivan, D. M. (1995). Nonlinear FDTD formulations using Z transforms. *IEEE Trans. on MTT*, 43(3), 676–682.
- Sullivan, D. M. (1997). An unsplit step 3-d PML for use with the FDTD method. *IEEE Microwave and Guided Wave Letters*, 7, 184-186.
- Taflove, A., & Hagness, S. C. (2005). *Computational Electrodynamics: The Finite-Difference Time-Domain Method*. MA: Artech House.
- Taflove, A., Oskooi, A., & Johnson, S. G. (2013). *Advances in FDTD Computational Electrodynamics: Photonics and Nanotechnology*. Artech House.
- Tretyakov, S., & et.al. (2017). The century of Metamaterials. *Journal of Optics (Special Issue)*, 19(8), 080404.
- Veihl, J. C., & Mittra, R. (1996). An efficient implementation of Berenger's perfectly matched layer (pml) for finite-difference time-domain mesh truncation. *IEEE Microwave and Guided Wave Letters*, 6, 94-96.
- Veselago, V. G. (1968). The Electrodynamics of Substances with Simultaneously Negative Values of ϵ and μ . *Sov. Phys.- Usp.*, 10(4), 509-514.
- Veselago, V., Braginsky, L., Shklover, V., & Hafne, C. (2006). Negative Refractive Index Materials. *Journal of Computational and Theoretical Nanoscience*, 3, 1-30.
- Wessel, W., Sieverding, T., & Arndt, F. (1999). Mode-matching analysis of general waveguide multiport junctions. *Proc. IEEE-MTT Symposium*, 3, 1273-1276.
- Wexler, A. (1967). Solution of waveguide discontinuities by modal analysis. *IEEE Trans. Microwave Theory Techniques*, 15, 508–517.

- Yee, K. S. (1966). Numerical Solution of Initial Boundary Value Problems Involving Maxwell's Equations in Isotropic Media. *IEEE Trans. on Antennas and Propagat.*, 14(3), 302–307.
- Yeh, P., Yariv, A., & Hong, C. S. (1977). Electromagnetic propagation in periodic stratified media, I. General Theory. *Journ. Opt. Soc. Am.*, 67(4), 423-438.
- Yongmei, P., & Shanxia, X. (2009). Complex modes in parallel-plate waveguide structure filled with left-handed material. *Chinese Jour. Electr.*, 18(3), 551-554.
- Zhang, S., & et.al. (2005). Experimental demonstration of near-infrared negative-index metamaterials. *Phys. Rev. Lett.*, 95(13), 137404.
- Zhao, L., & Cangellaris, A. C. (1996). Generalized theory of perfectly matched layers and its application to the reflectionless truncation of finite-difference time-domain grids. *IEEE Transactions on Microwave Theory and Techniques*, 44, 2555-2563.
- Zheng, K., Tam, W. Y., Ge, D. B., & Xu, J. D. (2009). Uniaxial PML absorbing boundary condition for truncating the boundary of DNG metamaterials. *Progress In Electromagnetics Research Letters*, 8, 125-134.
- Zhou, J., & et.al. (2006). Experimental demonstration of negative of index of refraction. *Appl.Phys. Lett.*, 88, 221103.
- Ziolkowski, R., & Kipple, A. (2003). Application of double negative metamaterials to increase the power radiated by electrically small antennas. *IEEE Trans. Antennas Propag.*, 51(10), 2626–2640.

APPENDICES

Appendix A. ADE-FDTD Update Equations in Two Dimension (2D)

We assume plane wave propagation along z-axis and TMz polarization in working out the formulation of ADE-FDTD algorithm for Lorentz type DNG media.

$$D_z(\omega) = \epsilon_o \epsilon_\infty E_z(\omega) + P(\omega) \quad (\text{A.1a})$$

$$B_x(\omega) = \mu_o \mu_\infty H_x(\omega) + J_x(\omega) \quad (\text{A.1b})$$

$$B_y(\omega) = \mu_o \mu_\infty H_y(\omega) + J_y(\omega) \quad (\text{A.1c})$$

where

$$P(\omega) = \epsilon_o \frac{\omega_{pe}^2}{\omega_{oe}^2 - \omega^2 + j\Gamma_e \omega} E_z(\omega) \quad (\text{A.2a})$$

$$J_x(\omega) = \mu_o \frac{\omega_{pm}^2}{\omega_{om}^2 - \omega^2 + j\Gamma_m \omega} H_x(\omega) \quad (\text{A.2b})$$

$$J_y(\omega) = \mu_o \frac{\omega_{pm}^2}{\omega_{om}^2 - \omega^2 + j\Gamma_m \omega} H_y(\omega) \quad (\text{A.2c})$$

The inverse Fourier transform of these two are:

$$\frac{\partial^2 P(t)}{\partial t^2} + \Gamma_e \frac{\partial P(t)}{\partial t} + \omega_{oe}^2 P(t) = \epsilon_o \omega_{pe}^2 E_z(t) \quad (\text{A.3a})$$

$$\frac{\partial^2 J_x(t)}{\partial t^2} + \Gamma_m \frac{\partial J_x(t)}{\partial t} + \omega_{om}^2 J_x(t) = \mu_o \omega_{pm}^2 H_x(t) \quad (\text{A.3b})$$

$$\frac{\partial^2 J_y(t)}{\partial t^2} + \Gamma_m \frac{\partial J_y(t)}{\partial t} + \omega_{om}^2 J_y(t) = \mu_o \omega_{pm}^2 H_y(t) \quad (\text{A.3c})$$

The discrete forms of Equations (A.3) are given as:

$$P^{n+1}(i, j) = \left[\frac{2 - \Delta t^2 \omega_{oe}^2}{1 + 0.5 \Delta t \Gamma_e} \right] P^n(i, j) + \left[\frac{0.5 \Delta t \Gamma_e - 1}{0.5 \Delta t \Gamma_e + 1} \right] P^{n-1}(i, j) + \left[\frac{\Delta t^2 \epsilon_o \omega_{pe}^2}{1 + 0.5 \Delta t \Gamma_e} \right] E_z^n(i, j) \quad (\text{A.4a})$$

$$J_x^{n+1/2}(i, j+1/2) = \left[\frac{2 - \Delta t^2 \omega_{om}^2}{1 + 0.5 \Delta t \Gamma_m} \right] J_x^{n-1/2}(i, j+1/2) + \left[\frac{0.5 \Delta t \Gamma_m - 1}{0.5 \Delta t \Gamma_m + 1} \right] J_x^{n-3/2}(i, j+1/2) + \left[\frac{\Delta t^2 \mu_o \omega_{pm}^2}{1 + 0.5 \Delta t \Gamma_m} \right] H_x^{n-1/2}(i, j+1/2) \quad (\text{A.4b})$$

$$J_y^{n+1/2}(i+1/2, j) = \left[\frac{2 - \Delta t^2 \omega_{om}^2}{1 + 0.5 \Delta t \Gamma_m} \right] J_y^{n-1/2}(i+1/2, j) + \left[\frac{0.5 \Delta t \Gamma_m - 1}{0.5 \Delta t \Gamma_m + 1} \right] J_y^{n-3/2}(i+1/2, j) + \left[\frac{\Delta t^2 \mu_o \omega_{pm}^2}{1 + 0.5 \Delta t \Gamma_m} \right] H_y^{n-1/2}(i, j) \quad (\text{A.4c})$$

These can then be used in iterative form and FDTD loops can be formed accordingly:

$$D_z^{n+1}(i, j) = D_z^n(i, j) + \Delta t \left[\frac{H_y^{n+1/2}(i+1/2, j) - H_y^{n+1/2}(i-1/2, j)}{\Delta x} - \frac{H_x^{n+1/2}(i, j+1/2) - H_x^{n+1/2}(i, j-1/2)}{\Delta y} \right] \quad (\text{A.5a})$$

$$B_x^{n+1/2}(i, j+1/2) = B_x^{n-1/2}(i, j+1/2) - \frac{\Delta t}{\Delta y} [E_z^n(i, j+1) - E_z^n(i, j)] \quad (\text{A.5b})$$

$$B_y^{n+1/2}(i+1/2, j) = B_y^{n-1/2}(i+1/2, j) + \frac{\Delta t}{\Delta x} [E_z^n(i+1, j) - E_z^n(i, j)] \quad (\text{A.5c})$$

$$E_z^{n+1}(i, j) = \frac{D_z^{n+1}(i, j) - P^{n+1}(i, j)}{\epsilon_o \epsilon_x} \quad (\text{A.6a})$$

$$H_x^{n+1/2}(i, j+1/2) = \frac{B_x^{n+1/2}(i, j+1/2) - J_x^{n+1/2}(i, j+1/2)}{\mu_o \mu_x} \quad (\text{A.6b})$$

$$H_y^{n+1/2}(i+1/2, j) = \frac{B_y^{n+1/2}(i+1/2, j) - J_y^{n+1/2}(i+1/2, j)}{\mu_o \mu_x} \quad (\text{A.6c})$$

When the resonance frequency ω_{oc} is taken as zero, the ADE-FDTD formulation in Equation (A.4) based on Lorentz model is reduced to Drude model's formulation. Hence the following process developed for Lorentz type DNG media simulations is also acceptable for Drude model simulations:

1. Update P^{n+1} using the previous values of E^n and P^n, P^{n-1} .
2. Update E^{n+1} in free space and insert excitation source.
3. Update D^{n+1} in DNG medium using the previous values of D^n and H_x^n, H_y^n .
4. Update E^{n+1} in DNG medium using the present value of D^{n+1} and P^{n+1} .
5. Apply the absorbing boundary conditions at the terminating nodes.
6. Repeat the whole steps for the magnetic fields (J, B, H).

Appendix B. Modified UPML in DNG media (DNG- UPML)

For a matched condition (Berenger, 2007) the time-harmonic Maxwell's curl equations in the UPML can be written in their most general form as (Taflove & Hagness, 2005).

$$\nabla \times \vec{H} = j\omega\epsilon \bar{\bar{s}} \vec{E} \quad (\text{B.1a})$$

$$\nabla \times \vec{E} = -j\omega\mu \bar{\bar{s}} \vec{H} \quad (\text{B.1b})$$

where $\bar{\bar{s}}$ is the diagonal tensor defined by

$$\bar{\bar{s}} = \bar{\bar{s}}_x \bar{\bar{s}}_y \bar{\bar{s}}_z = \begin{bmatrix} s_x^{-1} & 0 & 0 \\ 0 & s_x & 0 \\ 0 & 0 & s_x \end{bmatrix} \begin{bmatrix} s_y & 0 & 0 \\ 0 & s_y^{-1} & 0 \\ 0 & 0 & s_y \end{bmatrix} \begin{bmatrix} s_z & 0 & 0 \\ 0 & s_z & 0 \\ 0 & 0 & s_z^{-1} \end{bmatrix} = \begin{bmatrix} s_y s_z s_x^{-1} & 0 & 0 \\ 0 & s_x s_z s_y^{-1} & 0 \\ 0 & 0 & s_x s_y s_z^{-1} \end{bmatrix} \quad (\text{B.2})$$

and the diagonal elements of $\bar{\bar{s}}$ are given by

$$s_x = 1 + \frac{\sigma_x}{j\omega\epsilon_o} ; s_y = 1 + \frac{\sigma_y}{j\omega\epsilon_o} ; s_z = 1 + \frac{\sigma_z}{j\omega\epsilon_o} \quad (\text{B.3})$$

The conductivity σ_i (where $i = x, y, z$) is the loss parameter that controls the wave attenuation rate along the x, y or z axis in the UPML. However, DNG media have simultaneously negative permittivity and permeability and negative refractive index, if one still assumes $\sigma_i > 0$, the wave will grow exponentially in UPML, which results in instability. Consequently, some modifications on the original UPML method are required to yield a stable solution for DNG media as in the following:

$$\sigma_x^m = \frac{\sigma_x}{\sqrt{\varepsilon_r(\omega)}\sqrt{\mu_r(\omega)}} \Rightarrow s_x = 1 + \frac{\sigma_x^m}{j\omega\varepsilon_o} = 1 + \frac{\sigma_x}{j\omega\varepsilon_o\sqrt{\varepsilon_r(\omega)}\sqrt{\mu_r(\omega)}} \quad (\text{B.4a})$$

$$\sigma_y^m = \frac{\sigma_y}{\sqrt{\varepsilon_r(\omega)}\sqrt{\mu_r(\omega)}} \Rightarrow s_y = 1 + \frac{\sigma_y^m}{j\omega\varepsilon_o} = 1 + \frac{\sigma_y}{j\omega\varepsilon_o\sqrt{\varepsilon_r(\omega)}\sqrt{\mu_r(\omega)}} \quad (\text{B.4b})$$

$$\sigma_z^m = \frac{\sigma_z}{\sqrt{\varepsilon_r(\omega)}\sqrt{\mu_r(\omega)}} \Rightarrow s_z = 1 + \frac{\sigma_z^m}{j\omega\varepsilon_o} = 1 + \frac{\sigma_z}{j\omega\varepsilon_o\sqrt{\varepsilon_r(\omega)}\sqrt{\mu_r(\omega)}} \quad (\text{B.4c})$$

where σ_x^m, σ_y^m and σ_z^m are the modified conductivities in the x, y and z directions, respectively. Applying this modification to DNG media results in a DNG-UPML that can attenuate the electric and magnetic fields in each direction. One can find the choices of loss parameters and spatial grading of the PML loss parameters in Berenger's study (Berenger, 1994).

The FDTD approximation is derived from the time-harmonic Maxwell's curl equations and modified conductivities within the DNG-UPML medium, as defined in (B.4). Formulations can be implemented in One-Dimensional (1D), Two-Dimensional (2D) and Three-Dimensional (3D) cases. In the following section, 2D TM case is considered under $\partial/\partial z \equiv 0$ assumption that involves only E_z , H_x and H_y field components. Since the DNG-UPML can attenuate waves in both x and y direction, the diagonal tensor yields $\bar{\bar{s}} = \bar{\bar{s}}_x \bar{\bar{s}}_y$. Thus, the Maxwell equations in (B.1) can be reduced to a set of three equations as follows:

$$\frac{\partial H_y}{\partial x} - \frac{\partial H_x}{\partial y} = j\omega\varepsilon(\omega)s_x s_y E_z = j\omega\varepsilon_o\varepsilon_r(\omega)s_x s_y E_z \quad (\text{B.5a})$$

$$\frac{\partial E_z}{\partial y} = -j\omega\mu(\omega)\frac{s_y}{s_x} H_x = -j\omega\mu_o\mu_r(\omega)\frac{s_y}{s_x} H_x \quad (\text{B.5b})$$

$$\frac{\partial E_z}{\partial x} = j\omega\mu(\omega)\frac{s_x}{s_y} H_y = j\omega\mu_o\mu_r(\omega)\frac{s_x}{s_y} H_y \quad (\text{B.5c})$$

where $\varepsilon_r(\omega)$ and $\mu_r(\omega)$ are the relative permittivity and permeability of DNG media, respectively. Considering the identical models for $\varepsilon_r(\omega)$ and $\mu_r(\omega)$, s_x and s_y can be rewritten as

$$s_x = 1 + \frac{\sigma_x}{j\omega\varepsilon_o\varepsilon_r(\omega)} ; s_y = 1 + \frac{\sigma_y}{j\omega\varepsilon_o\varepsilon_r(\omega)} \quad (\text{B.6})$$

To derive an equivalent system of time domain differential equations for (B.5), some auxiliary field variables are introduced as in (Lu L. , 2006).

$$D_z(\omega) = \varepsilon_o\varepsilon_r(\omega)s_x s_y E_z(\omega) = s_x P_z(\omega) \quad (\text{B.7a})$$

$$B_x(\omega) = \mu_o\mu_r(\omega)\frac{s_y}{s_x} H_x(\omega) = \mu_o\mu_r(\omega)Q_x(\omega) \quad (\text{B.7b})$$

$$B_y(\omega) = \mu_o\mu_r(\omega)\frac{s_x}{s_y} H_y(\omega) = \mu_o\mu_r(\omega)Q_y(\omega) \quad (\text{B.7c})$$

where

$$P_z(\omega) = \varepsilon_o\varepsilon_r(\omega)s_y E_z(\omega) \quad (\text{B.8a})$$

$$Q_x(\omega) = \frac{s_y}{s_x} H_x(\omega) \quad (\text{B.8b})$$

$$Q_y(\omega) = \frac{s_x}{s_y} H_y(\omega) \quad (\text{B.8c})$$

Substituting (B.7) into (B.5), the Maxwell equations yield:

$$\frac{\partial H_y}{\partial x} - \frac{\partial H_x}{\partial y} = j\omega D_z \quad (\text{B.9a})$$

$$\frac{\partial E_z}{\partial y} = -j\omega B_x \quad (\text{B.9b})$$

$$\frac{\partial E_z}{\partial x} = j\omega B_y \quad (\text{B.9c})$$

Applying the second-order FDTD discretization both in space and time to equations (B.9a) leads to a time-stepping expression for D_z :

$$D_z^{n+1}\Big|_{(i,j)} = D_z^n\Big|_{(i,j)} + \Delta t \left[\frac{H_y^{n+1/2}\Big|_{(i+1/2,j)} - H_y^{n+1/2}\Big|_{(i-1/2,j)}}{\Delta x} - \frac{H_x^{n+1/2}\Big|_{(i,j+1/2)} - H_x^{n+1/2}\Big|_{(i,j-1/2)}}{\Delta y} \right] \quad (\text{B.10})$$

Substituting s_x in (B.5a) into (B.6a) yields

$$D_z = s_x P_z = \left(1 + \frac{\sigma_x}{j\omega \epsilon_o \epsilon_r(\omega)} \right) P_z \quad (\text{B.11})$$

Multiplying $j\omega \epsilon_r(\omega)$ on both sides of (B.11) and using Lorentz type model, one obtains

$$j\omega \left(1 + \frac{\omega_{pe}^2}{\omega_{oe}^2 - \omega^2 + j\Gamma_e \omega} \right) D_z = j\omega \left(1 + \frac{\omega_{pe}^2}{\omega_{oe}^2 - \omega^2 + j\Gamma_e \omega} \right) P_z + \frac{\sigma_x}{\epsilon_o} P_z \quad (\text{B.12})$$

Here ω_{oe} is set to zero as in (Cummer, 2004) to avoid the third order differential equation in time for simplicity in implementation of FDTD scheme. Then (B.12) can be represented as follows:

$$\left(\omega^2 - j\Gamma_e\omega - \omega_{pe}^2\right)D_z = \left(\omega^2 - j\Gamma_e\omega - \omega_{pe}^2\right)P_z + \frac{\sigma_x}{\epsilon_o}(-j\omega - \Gamma_e)P_z \quad (\text{B.13})$$

Taking the inverse Fourier transform of (B.13) yields

$$\left(\frac{d^2}{dt^2} + \Gamma_e \frac{d}{dt} + \omega_{pe}^2\right)D_z = \left(\frac{d^2}{dt^2} + \left(\Gamma_e + \frac{\sigma_x}{\epsilon_o}\right)\frac{d}{dt} + \left(\omega_{pe}^2 + \frac{\sigma_x\Gamma_e}{\epsilon_o}\right)\right)P_z \quad (\text{B.14})$$

Applying a centered second-order finite difference approximation to equation (B.14) and grouping like terms produces

$$P_z^{n+1}\Big|_{(i,j)} = \left[a_1 P_z^n + a_2 P_z^{n-1} + b_0 D_z^{n+1} + b_1 D_z^n + b_2 D_z^{n-1} \right]\Big|_{(i,j)} \quad (\text{B.15})$$

where

$$\begin{aligned} a_1 &= \frac{8\epsilon_o - 2\Delta t^2(\sigma_x\Gamma_e + \epsilon_o\omega_{pe}^2)}{AB}; a_2 = \frac{2\Delta t(\sigma_x + \epsilon_o\Gamma_e) - 4\epsilon_o - \Delta t^2(\sigma_x\Gamma_e + \epsilon_o\omega_{pe}^2)}{AB} \\ b_0 &= \frac{4\epsilon_o + 2\Delta t\epsilon_o\Gamma_e + \omega_{pe}^2\Delta t^2\epsilon_o}{AB}; b_1 = \frac{2\Delta t^2\epsilon_o\omega_{pe}^2 - 8\epsilon_o}{AB}; b_2 = \frac{4\epsilon_o - 2\Delta t\epsilon_o\Gamma_e + \omega_{pe}^2\Delta t^2\epsilon_o}{AB} \\ AB &= 4\epsilon_o + 2\Delta t(\sigma_x + \epsilon_o\Gamma_e) + \Delta t^2(\sigma_x\Gamma_e + \epsilon_o\omega_{pe}^2) \end{aligned}$$

Let $E_{zz}(\omega) = s_y E_z(\omega)$, then (B.8a) can be rewritten as

$$P_z(\omega) = \epsilon_o \epsilon_r(\omega) E_{zz}(\omega) = \epsilon_o (\epsilon_\infty + \chi_e(\omega)) E_{zz}(\omega) = \epsilon_o \epsilon_\infty E_{zz}(\omega) + S_{kz}(\omega) \quad (\text{B.16a})$$

where

$$S_{kz}(\omega) = \varepsilon_o \chi_e(\omega) E_{zz}(\omega) \quad (\text{B.16b})$$

Applying ADE approach, we obtain FDTD update equations for S_{kz} and E_{zz} as:

$$S_{kz}^{n+1}(i, j) = \left[\frac{2 - \Delta t^2 \omega_{oe}^2}{1 + 0.5 \Delta t \Gamma_e} \right] S_{kz}^n(i, j) + \left[\frac{0.5 \Delta t \Gamma_e - 1}{0.5 \Delta t \Gamma_e + 1} \right] S_{kz}^{n-1}(i, j) + \left[\frac{\Delta t^2 \varepsilon_o \omega_{pe}^2}{1 + 0.5 \Delta t \Gamma_e} \right] E_{zz}^n(i, j) \quad (\text{B.17})$$

$$E_{zz}^{n+1} = \frac{P_z^{n+1} - S_{kz}^{n+1}}{\varepsilon_o \varepsilon_\infty} \quad (\text{B.18})$$

Finally, substituting s_y given in (B.6b) into the equality of $E_{zz}(\omega) = s_y E_z(\omega)$ and applying same procedure for Pz (see D.11), we obtain the next step values of E_z .

$$E_{zz} = s_y E_z = \left(1 + \frac{\sigma_y}{j \omega \varepsilon_o \varepsilon_r(\omega)} \right) E_z \quad (\text{B.19})$$

$$E_z^{n+1} \Big|_{(i+1/2, j+1/2)} = \left[c_1 E_z^n + c_2 E_z^{n-1} + d_0 E_{zz}^{n+1} + d_1 E_{zz}^n + d_2 E_{zz}^{n-1} \right] \Big|_{(i+1/2, j+1/2)} \quad (\text{B.20})$$

where

$$\begin{aligned} c_1 &= \frac{8\varepsilon_o - 2\Delta t^2(\sigma_y \Gamma_e + \varepsilon_o \omega_{pe}^2)}{CD}; c_2 = \frac{2\Delta t(\sigma_y + \varepsilon_o \Gamma_e) - 4\varepsilon_o - \Delta t^2(\sigma_y \Gamma_e + \varepsilon_o \omega_{pe}^2)}{CD} \\ d_0 &= \frac{4\varepsilon_o + 2\Delta t \varepsilon_o \Gamma_e + \omega_{pe}^2 \Delta t^2 \varepsilon_o}{CD}; d_1 = \frac{2\Delta t^2 \varepsilon_o \omega_{pe}^2 - 8\varepsilon_o}{CD}; d_2 = \frac{4\varepsilon_o - 2\Delta t \varepsilon_o \Gamma_e + \omega_{pe}^2 \Delta t^2 \varepsilon_o}{CD} \\ CD &= 4\varepsilon_o + 2\Delta t(\sigma_y + \varepsilon_o \Gamma_e) + \Delta t^2(\sigma_y \Gamma_e + \varepsilon_o \omega_{pe}^2) \end{aligned}$$

Similarly, the explicit time-stepping expressions for the components B_x , Q_x , H_x and B_y , Q_y , H_y are given by

$$J_x^{n+3/2}(i, j+1/2) = \left[\frac{2 - \Delta t^2 \omega_{om}^2}{1 + 0.5\Delta t \Gamma_m} \right] J_x^{n+1/2}(i, j+1/2) + \left[\frac{0.5\Delta t \Gamma_m - 1}{0.5\Delta t \Gamma_m + 1} \right] J_x^{n-1/2}(i, j+1/2) + \left[\frac{\Delta t^2 \mu_o \omega_{pm}^2}{1 + 0.5\Delta t \Gamma_m} \right] H_x^{n+1/2}(i, j+1/2) \quad (B.21)$$

$$B_x^{n+3/2} \Big|_{(i,j+1/2)} = B_x^{n+1/2} \Big|_{(i,j+1/2)} - \frac{\Delta t}{\Delta y} \left[E_z^{n+1} \Big|_{(i,j+1)} - E_z^{n+1} \Big|_{(i,j)} \right] \quad (B.22)$$

$$Q_x^{n+3/2} = \frac{B_x^{n+3/2} - J_x^{n+3/2}}{\mu_o \mu_\infty} \quad (B.23)$$

$$H_x^{n+3/2} \Big|_{(i,j+1/2)} = \left[k_1 H_x^{n+1/2} + k_2 H_x^{n-1/2} + m_0 Q_x^{n+3/2} + m_1 Q_x^{n+1/2} + m_2 Q_x^{n-1/2} \right] \Big|_{(i,j+1/2)} \quad (B.24)$$

where

$$k_1 = \frac{8\varepsilon_o - 2\Delta t^2 (\sigma_y \Gamma_e + \varepsilon_o \omega_{pe}^2)}{KM}; k_2 = \frac{2\Delta t (\sigma_y + \varepsilon_o \Gamma_e) - 4\varepsilon_o - \Delta t^2 (\sigma_y \Gamma_e + \varepsilon_o \omega_{pe}^2)}{KM}$$

$$m_0 = \frac{4\varepsilon_o + 2\Delta t (\sigma_x + \varepsilon_o \Gamma_e) + \Delta t^2 (\sigma_x \Gamma_e + \varepsilon_o \omega_{pe}^2)}{KM}; m_1 = \frac{2\Delta t^2 (\sigma_x \Gamma_e + \varepsilon_o \omega_{pe}^2) - 8\varepsilon_o}{KM}$$

$$m_2 = \frac{4\varepsilon_o - 2\Delta t (\sigma_x + \varepsilon_o \Gamma_e) + \Delta t^2 (\sigma_x \Gamma_e + \varepsilon_o \omega_{pe}^2)}{KM}; KM = 4\varepsilon_o + 2\Delta t (\sigma_y + \varepsilon_o \Gamma_e) + \Delta t^2 (\sigma_y \Gamma_e + \varepsilon_o \omega_{pe}^2)$$

$$J_y^{n+3/2}(i+1/2, j) = \left[\frac{2 - \Delta t^2 \omega_{om}^2}{1 + 0.5\Delta t \Gamma_m} \right] J_y^{n+1/2}(i+1/2, j) + \left[\frac{0.5\Delta t \Gamma_m - 1}{0.5\Delta t \Gamma_m + 1} \right] J_y^{n-1/2}(i+1/2, j) + \left[\frac{\Delta t^2 \mu_o \omega_{pm}^2}{1 + 0.5\Delta t \Gamma_m} \right] H_y^{n+1/2}(i+1/2, j) \quad (B.25)$$

$$B_y^{n+3/2}\Big|_{(i+1/2,j)} = B_y^{n+1/2}\Big|_{(i+1/2,j)} + \frac{\Delta t}{\Delta x} \left[E_z^{n+1}\Big|_{(i+1,j)} - E_z^{n+1}\Big|_{(i,j)} \right] \quad (\text{B.26})$$

$$Q_y^{n+1} = \frac{B_y^{n+1} - J_y^{n+1}}{\mu_o \mu_\infty} \quad (\text{B.27})$$

$$H_y^{n+3/2}\Big|_{(i+1/2,j)} = \left[p_1 H_y^{n+1/2} + p_2 H_y^{n-1/2} + r_0 Q_y^{n+3/2} + r_1 Q_y^{n+1/2} + r_2 Q_y^{n-1/2} \right] \Big|_{(i+1/2,j)} \quad (\text{B.28})$$

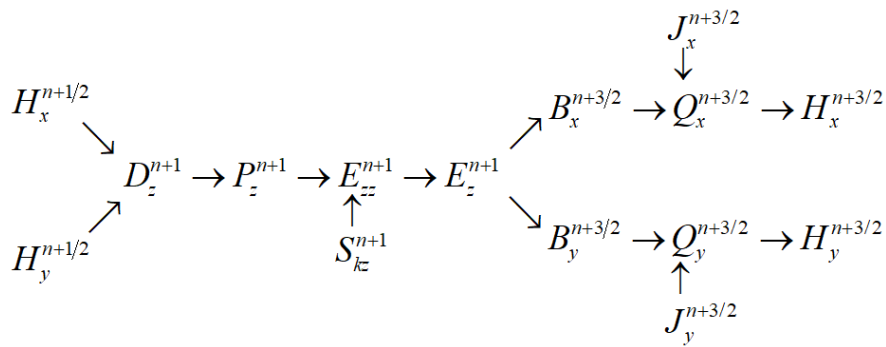
where

$$p_1 = \frac{8\varepsilon_o - 2\Delta t^2(\sigma_x \Gamma_e + \varepsilon_o \omega_{pe}^2)}{PR}; p_2 = \frac{2\Delta t(\sigma_x + \varepsilon_o \Gamma_e) - 4\varepsilon_o - \Delta t^2(\sigma_x \Gamma_e + \varepsilon_o \omega_{pe}^2)}{PR}$$

$$r_0 = \frac{4\varepsilon_o + 2\Delta t(\sigma_y + \varepsilon_o \Gamma_e) + \Delta t^2(\sigma_y \Gamma_e + \varepsilon_o \omega_{pe}^2)}{PR}; r_1 = \frac{2\Delta t^2(\sigma_y \Gamma_e + \varepsilon_o \omega_{pe}^2) - 8\varepsilon_o}{PR}$$

$$r_2 = \frac{4\varepsilon_o - 2\Delta t(\sigma_y + \varepsilon_o \Gamma_e) + \Delta t^2(\sigma_y \Gamma_e + \varepsilon_o \omega_{pe}^2)}{PR}; PR = 4\varepsilon_o + 2\Delta t(\sigma_x + \varepsilon_o \Gamma_e) + \Delta t^2(\sigma_x \Gamma_e + \varepsilon_o \omega_{pe}^2)$$

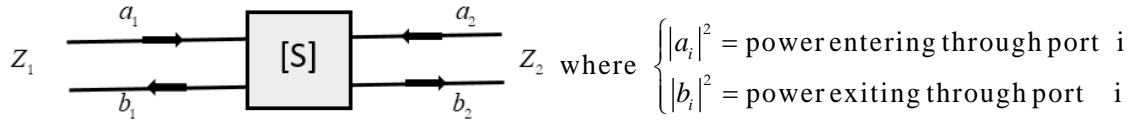
The process of UPML-DNG simulations using the above equations are:



Appendix C. S-Matrix Representation

C1. S-Matrix Representation of Fully Loaded Single Two-Port Circuit:

We note that when the empty waveguide is assumed to be lossless the phases of R and T depend on the location of the reference planes used in their definitions, but their amplitudes do not. Moreover, in case the absorption losses within scattering region tend to zero the sum of the squared magnitudes of R and T approach to unity (power conservation).



$$\begin{bmatrix} b_1 \\ b_2 \end{bmatrix} = \begin{bmatrix} S_{11} & S_{12} \\ S_{21} & S_{22} \end{bmatrix} \begin{bmatrix} a_1 \\ a_2 \end{bmatrix} \Rightarrow S_{11} = \left. \frac{b_1}{a_1} \right|_{a_2=0}; S_{21} = \left. \frac{b_2}{a_1} \right|_{a_2=0}; S_{12} = \left. \frac{b_1}{a_2} \right|_{a_1=0}; S_{22} = \left. \frac{b_2}{a_2} \right|_{a_1=0} \quad (\text{C.1})$$

When we deal with a lossless problem then the power entering the region should be equal to the power exiting from the region:

$$P_{enter} = P_{exit} \Rightarrow \frac{1}{2} \sum |a_i|^2 = \frac{1}{2} \sum |b_i|^2 \Rightarrow [a]^T [a^*] = [b]^T [b^*] \Rightarrow [a]^T [I] [a^*] = [b]^T [b^*] \quad (\text{C.2})$$

where $\sum |b_i|^2 = [b_1 \ b_2] \begin{bmatrix} b_1^* \\ b_2^* \end{bmatrix}$; $[b]^T [b^*] = b_1 b_1^* + b_2 b_2^*$ and $[I] = [S]^T [S]^*$. If the problem

is reciprocal we should also have $[S]^T = [S]$. Then,

$$\begin{bmatrix} S_{11} & S_{12} \\ S_{21} & S_{22} \end{bmatrix} \begin{bmatrix} S_{11}^* & S_{12}^* \\ S_{21}^* & S_{22}^* \end{bmatrix} = \begin{bmatrix} 1 & 0 \\ 0 & 1 \end{bmatrix} \quad (\text{C.3})$$

$$\left. \begin{aligned} S_{11}S_{12}^* + S_{12}S_{22}^* = 0 \rightarrow S_{12}S_{11}^* + S_{22}S_{12}^* = 0 \\ S_{21}S_{11}^* + S_{22}S_{21}^* = 0 \end{aligned} \right\} S_{21} = S_{12} \text{ and } S_{12}^* = S_{21}^* \Rightarrow [S]^t = [S] \quad (\text{C.4})$$

$$\left. \begin{aligned} S_{11}S_{11}^* + S_{12}S_{21}^* = 1 \\ S_{21}S_{12}^* + S_{22}S_{22}^* = 1 \end{aligned} \right\} \left. \begin{aligned} |S_{11}|^2 + |S_{12}|^2 = 1 \\ |S_{12}|^2 + |S_{22}|^2 = 1 \end{aligned} \right\} |S_{11}| = |S_{22}| \quad (\text{C.5})$$

Let $|S_{11}| = R \Rightarrow S_{11} = R e^{j\theta_1}$, $|S_{22}| = |S_{11}| = R \Rightarrow S_{22} = R e^{j\theta_2}$ and $|S_{12}| = T \Rightarrow S_{12} = T e^{j\theta}$, then the angle relation between S parameters are found as:

$$S_{11}S_{12}^* + S_{12}S_{22}^* = 0 \Rightarrow R e^{j\theta_1} T e^{-j\theta} + T e^{j\theta} R e^{-j\theta_2} = 0 \Rightarrow \theta_1 + \theta_2 = 2\theta \pm \pi \quad (\text{C.6})$$

In special case of symmetric regions (both geometry and electrical parameters) no distinction can be made between port 1 and 2. Thus, indices 1 and 2 are interchangeable.

S matrix will then have the form $\begin{bmatrix} S_{11} & S_{12} \\ S_{12} & S_{22} \end{bmatrix}$ and from above it follows $\theta_1 = \theta_2 = \theta \pm \pi / 2$ which yields:

$$S_{11} = |S_{11}| e^{j\theta_1}; S_{12} = |S_{12}| e^{j\theta} \Rightarrow \theta_1 = \theta \pm \pi / 2. \quad (\text{C.7})$$

Now we consider the relations obtained for a section of waveguide completely-filled with DNG material.

$$S_{11} = -j \frac{2\Gamma e^{-j\beta_2 d} \sin \beta_2 d}{1 - \Gamma^2 e^{-j2\beta_2 d}} = -j \frac{2\Gamma e^{-j\beta_2 d} \sin \beta_2 d}{D e^{j\phi}} = |S_{11}| e^{j\theta_1} \Rightarrow \theta_1 = -(\beta_2 d + \phi + \pi / 2) \quad (\text{C.8})$$

$$S_{12} = \frac{(1 - \Gamma^2) e^{-j\beta_2 d}}{1 - \Gamma^2 e^{-j2\beta_2 d}} = \frac{(1 - \Gamma^2) e^{-j\beta_2 d}}{D e^{j\phi}} = |S_{12}| e^{j\theta} \Rightarrow \theta = -(\beta_2 d + \phi) \quad (\text{C.9})$$

where $1 - \Gamma^2 e^{-j2\beta_2 d} = D e^{j\phi}$.

This relation between S_{11} and S_{12} is true if and only if $S_{11} = S_{22}$ and their angles. So, we can say that the DNG system can be assumed symmetric. Thus, when β_2 is real (region lossless) the phase relationship between S_{11} and S_{12} are satisfied. When Lorentz model contains no loss term we have: $\beta_2 = k_0 \sqrt{\epsilon_{r2} \mu_{r2} - (\lambda_0/2a)^2}$ for dominant mode. Thus, β_2 is purely imaginary at frequencies above cutoff ($\epsilon_{r2} \mu_{r2} < (\lambda_0/2a)^2$). Since T will then decrease exponentially, the positive sign should be selected to amplify wave exponentially.

C2. S-Matrix Representation of Fully Loaded Cascade Connected Two-Port Circuit:

The total scattering matrix of the system is defined by the S-matrix of each circuit as given in (Şimşek, Işık, & Topuz, 2011):

$$\begin{bmatrix} b_1^A \\ b_2^A \end{bmatrix} = \begin{bmatrix} S_{11}^A & S_{12}^A \\ S_{21}^A & S_{22}^A \end{bmatrix} \begin{bmatrix} a_1^A \\ a_2^A \end{bmatrix}; \begin{bmatrix} b_1^B \\ b_2^B \end{bmatrix} = \begin{bmatrix} S_{11}^B & S_{12}^B \\ S_{21}^B & S_{22}^B \end{bmatrix} \begin{bmatrix} a_1^B \\ a_2^B \end{bmatrix} \Rightarrow \begin{bmatrix} b_1^A \\ b_2^B \end{bmatrix} = \begin{bmatrix} S_{11} & S_{12} \\ S_{21} & S_{22} \end{bmatrix} \begin{bmatrix} a_1^A \\ a_2^B \end{bmatrix} \quad (\text{C.10})$$

where

$$\left. \begin{aligned} S_{11} &= S_{11}^A + \frac{e^{-j2\beta L} S_{12}^A S_{11}^B S_{21}^A}{(1 - e^{-j2\beta L} S_{22}^A S_{11}^B)} \\ S_{21} &= \frac{e^{-j2\beta L} S_{21}^B S_{21}^A}{(1 - e^{-j2\beta L} S_{22}^A S_{11}^B)} \\ S_{12} &= \frac{e^{-j2\beta L} S_{12}^A S_{12}^B}{(1 - e^{-j2\beta L} S_{22}^A S_{11}^B)} \\ S_{22} &= S_{22}^B + \frac{e^{-j2\beta L} S_{21}^B S_{22}^A S_{12}^B}{(1 - e^{-j2\beta L} S_{22}^A S_{11}^B)} \end{aligned} \right\} \xrightarrow{\text{if } L=0} \left. \begin{aligned} S_{11} &= S_{11}^A + \frac{S_{12}^A S_{11}^B S_{21}^A}{(1 - S_{22}^A S_{11}^B)} \\ S_{21} &= \frac{S_{21}^B S_{21}^A}{(1 - S_{22}^A S_{11}^B)} \\ S_{12} &= \frac{S_{12}^A S_{12}^B}{(1 - S_{22}^A S_{11}^B)} \\ S_{22} &= S_{22}^B + \frac{S_{21}^B S_{22}^A S_{12}^B}{(1 - S_{22}^A S_{11}^B)} \end{aligned} \right\} \quad (\text{C.11})$$

S-parameters of each circuit can be obtained by using Equation (C.12).

$$\begin{aligned}
S_{11}^A &= -j \frac{2\Gamma_1 e^{-j\beta_1 d_1} \sin \beta_1 d_1}{1 - \Gamma_1^2 e^{-j2\beta_1 d_1}} & ; & \quad S_{22}^A = S_{11}^A \\
S_{11}^B &= -j \frac{2\Gamma_2 e^{-j\beta_2 d_2} \sin \beta_2 d_2}{1 - \Gamma_2^2 e^{-j2\beta_2 d_2}} & ; & \quad S_{22}^B = S_{11}^B \\
S_{12}^A &= \frac{(1 - \Gamma_1^2) e^{-j\beta_1 d_1}}{1 - \Gamma_1^2 e^{-j2\beta_1 d_1}} & ; & \quad S_{21}^A = S_{12}^A \\
S_{12}^B &= \frac{(1 - \Gamma_2^2) e^{-j\beta_2 d_2}}{1 - \Gamma_2^2 e^{-j2\beta_2 d_2}} & ; & \quad S_{21}^B = S_{12}^B
\end{aligned} \tag{C.12}$$

where $\Gamma_i = \frac{Z_0 - Z_i}{Z_0 + Z_i}$; $Z_0 = \frac{\omega\mu_0}{\beta_0}$; $\beta_0 = k_0 \sqrt{1 - \left(\frac{\lambda_o}{2a}\right)^2}$; $Z_i = \frac{\omega\mu_i}{\beta_i}$; $\beta_i = k_0 \sqrt{\epsilon_{ri} \mu_{ri} - \left(\frac{\lambda_o}{2a}\right)^2}$; $i = 1, 2$

CIRRICULUM VITAE

NAME OF AUTHOR : Ayşegül Pekmezci
PLACE OF BIRTH : Zonguldak, Turkey
DATE OF BIRTH : 23 February, 1984

GRADUATE AND UNDERGRADUATE SCHOOLS ATTENDED:

Master of Science in Electrical & Electronics Engineering, 2010, Gaziantep University, Gaziantep TURKEY

Bachelor of Science in Electrical & Electronics Engineering, 2007, Gaziantep University, Gaziantep TURKEY

WORK EXPERIENCE:

Research Assistant, Department of Electronics and Communications Engineering, Dogus University, June 2012 – Present.

Research Assistant, Department of Electrical & Electronics Engineering, University of Gaziantep, January 2008 – June 2012.

PUBLICATIONS:

International Journal Papers (SCI, SSCI)

[5] A. Pekmezci, E. Topuz, "Modal Properties of Parallel Plate Waveguide Partially Loaded with Double Negative Materials"; Journal of Electromagnetic Waves and Applications; vol. xx, no. xx, pp: xx, 2018 (submitted).

[4] A. Pekmezci, E. Topuz, L. Sevgi, "First and Second Order Mur Type ABCs for DNG Media"; The Applied Computational Electromagnetics Society Journal; vol. 33, no. 6, pp: 569-574, 2018.

[3] A. Pekmezci, E. Topuz, L. Sevgi, "Finite Difference Time Domain Formulation for Epsilon-Negative Medium Using Wave Equation"; International Journal of RF and Microwave Computer-Aided Engineering, vol. 26, no. 4, May 2016

[2] A. Pekmezci, L. Sevgi, "FDTD based Metamaterial (MTM) Modeling"; IEEE Antennas and Propagation Magazine, vol. 56, no. 5, pp:289-303, October 2014.

[1] A. Pekmezci, T.Ege; "Scattering Characteristics of FSSs with Triangular Conducting Elements", Springer Electrical Engineering, vol.96, no.2, pp:145-155, June 2014

Conference Papers and Proceedings: (International)

[2] A. Pekmezci, E. Topuz, L. Sevgi, " FDTD Formulation for Epsilon-Negative (ENG) Medium Using Wave Equation, 3rd International EMC Turkiye Conference, Işık Üniversitesi, İstanbul 2-4 Eylül 2015.

[1] A. Pekmezci, T. Ege; "Frequency Selective Surfaces With Thin Triangular Conducting Elements", PIERS Proceedings, 166 - 169, July 5-8, Cambridge, USA 2010.

Conference Papers: (National)

[2] A. Pekmezci, L. Sevgi; "Elektromanyetik Uyumluluk ve Kırınım Problemlerinde Analitik Yöntemler", EMC 2013, Işık Üniversitesi, İstanbul 9-11 Eylül 2013.

[1] A. Pekmezci, T. Ege; "Düzlemsel Dielektrik Levha Üzerine Yerleştirilmiş İkizkenar Üçgen Şeklindeki İletken Elemanların Analizi", URSI-2010, Kıbrıs 25-27 Ağustos 2010.

MEMBERSHIP FOR ACADEMIC OR PROFESSIONAL ORGANIZATIONS:

IEEE Student Member, TMMOB Elektrik Mühendisleri Odası

AWARDS:

TURKCELL- Turkcell Akademi Yüksek Lisans Bursu (2008-2010)

Leopold B. FELSEN Vakfı Elektromanyetikte Üstün Başarı Ödülü (2016)